REORIENTATION AND SOLVATION DYNAMICS OF BULK AND CONFINED ALCOHOLS

BY

ANTHONY ANDREW VARTIA

Submitted to the graduate degree program in Chemistry
and the Graduate Faculty of the University of Kansas in partial fulfillment of
the requirements for the degree of Doctor of Philosophy

Chairperson Ward H. Thompson

Brian B. Laird

Christopher G. Elles

Timothy A. Jackson

Aaron M. Scurto

Date defended: November 13, 2012

The Dissertation Committee for ANTHONY ANDREW VARTIA
certifies that this is the approved version of the following dissertation:

REORIENTATION AND SOLVATION DYNAMICS OF BULK AND CONFINED ALCOHOLS

Chairperson Ward H. Thompson

Date approved: December 12, 2012

Abstract

Reorientation and solvation dynamics play a central role in chemistry in the liquid phase. In this work, molecular dynamics simulations are used to study hydroxyl group reorientation dynamics for a series of neat linear alcohols. The recently developed extended jump model satisfactorily explains reorientational slowing with increasing chain length for the water/methanol/ethanol series. The analysis indicates that hydrogen bond strength and exchange geometries are similar across the series, and that the dynamic retardation originates with decreased hydrogen bond exchange due to the increased excluded volume associated with longer alkyl chains. The reorientation of intact hydrogen bonds is thus the dominant reorientation pathway in lower alcohols, while hydrogen bond exchange is dominant in water. Simulation data for higher alcohols show emergent timescales and increased ordering in the liquid, which can also be interpreted within the extended jump model. While new barriers, which are the origin of the additional timescales, appear in free energy profiles for reorientation, solvent viscosity must also be considered. Ethanol and a Stockmayer model solute were confined within a roughly cylindrical silica pore to investigate the effect of confinement on solvation dynamics. The results of solute free energy calculations along a one-dimensional cut through the pore indicate that the charge distribution of the solute controls its location within the pore. Furthermore, the fluorescence energy is a function of solute position in a hydrophilic (but not hydrophobic) pore. These effects originate from silica surface roughness and chemistry, which also strongly alter solvent

behavior in the pore. The results indicate that solute motion contributes to the time-dependent fluorescence (TDF) spectrum, but the extent to which this can be observed is still under investigation. A comparison of TDF spectra and other solute properties in the pore for the Stockmayer solute and coumarin 153 dye model indicate that identifying how specific solute and silica properties combine to change spectral properties will require systematic testing of a series of dye and confinement models.

Contents

List of Figures

List of Tables

Chapter 1

Introduction

The dynamics of molecules in the liquid state is relevant to a broad range of chemistry. Of the various kinds of motions that molecules undergo—translation, vibration, and rotation or reorientation—the last of these has received special attention because of the role reorientation of common liquid solvents plays in chemistry. A chemical solute is solvated when surrounding solvent molecules are organized to provide the most favorable solute-solvent interactions. During chemical reactions and transformations, the charge distributions of solute molecules and their reaction intermediates change. Solvation effects then depend on the ability of the surrounding liquid to reorganize—that is, reorient—such that the solvent stabilizes the new charge distribution of the solute, reaction complex, or transition state. The relative timescales of the solute and solvent motions can have a dramatic impact on the reaction mechanisms and kinetics.

A particularly illustrative example can be found in charge transfer reactions. The movement of charge between reactant molecules or sites within the same

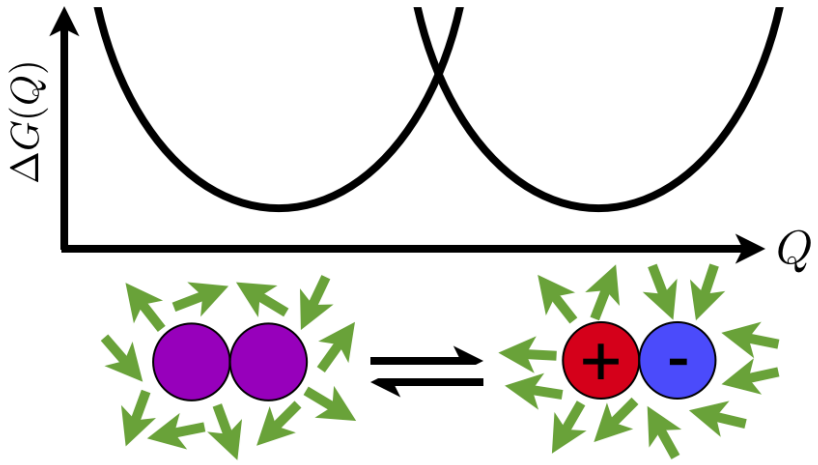

Figure 1.1: A schematic charge transfer reaction is presented. On the left is a neutral diatomic reactant molecule (purple), and the dipole moments of the surrounding solvent (green) are randomly oriented. On the right, the charge transfer product, a dipolar solute with positive (red) and negative (blue) ends, is stabilized by the solvent. In this case, the solvent dipoles are organized so as to favorably interact with the solute charges.

molecule can be facilitated in several ways, for example photoexcitation, chemical modification, temperature, or solvent rearrangements. In the last, dipolar solvents (*e.g.*, dioxane, acetonitrile, methanol) stabilize charge redistribution through reorientation of their dipoles, as depicted schematically in Figure 1.1. On the left side of Figure 1.1 the solvent dipole moments (green) are randomly distributed around the neutral solute (purple). Upon reaction, charge within the neutral molecule is redistributed so as to form positive (red) and negative (blue) ends. On the right side of Figure 1.1, the solvent dipole moments are organized so as to stabilize this new charge distribution. The rate at which the charge redistribution can be stabilized depends upon the ability of the solvent dipole to reorient. That is, charge transfer

reaction dynamics and reorientation dynamics are inextricably related. Inasmuch as the solvent responds to charge transfer, solvent fluctuations can drive charge transfer.

Notably, the solvent response has several components. For neutral solutes, the largest electrostatic interactions between solute and solvent involve molecular dipole moments. Because the solvent response involves charge redistribution, both electronic and nuclear motions contribute, but these can be treated separately within the Born-Oppenheimer approximation. The electronic response comes largely from the polarizability of the electron cloud, changing the dipole moment of the solvent. Because of the fast timescale on which this electronic response occurs, it is frequently averaged over or neglected in measurements of reorientation. The remainder of the solvent reorganization is achieved through nuclear motions. The fast translational and vibrational contributions can be captured in experiments that are sensitive to these motions and have sufficiently high temporal resolution. However, almost all experiments (generally picosecond resolution or better) report on the slow molecular reorientation component. To understand these solvation processes, including those relevant to chemical reactions such as electron or proton transfer (Figure 1.1), one must study reorientation dynamics.

Interestingly, experimental studies using methods that report on reorientation also show that the environment in which molecules are allowed to move dramatically impacts the timescales on which they do so. In a bulk liquid, molecular reorientation is generally observed on the picosecond timescale. In contrast, molecules within a confining framework that spans a handful of molecular diameters (or

"nanoconfined") show dramatically slowed reorientation [1–12], often orders of magnitude slower than in the corresponding bulk solvent. Additionally, timescales that have no bulk counterpart often emerge as a result of nanoconfinement—an effect with a debated origin[13].

While water has been thoroughly studied due to its strong solvation properties and relevance to myriad chemistries, the alcohols are less understood and far less studied. The chemical similarity of alcohols to water due to the presence of hydrogen bonding hydroxyl groups and their similar significance in a broad range of chemistries make alcohols an interesting subject for study. Notably, the linear chain alcohols show the trend that hydroxyl reorientation timescales increase (*i.e.*, slow) with increasing alkyl chain length. Additionally, experiments on nanoconfined alcohol systems show both slowed and additional timescales compared to the bulk liquid. Thus, it appears that hydroxyl reorientation is a function of its environment, but how the environment gives rise to these effects is not understood.

The aim of this work is to explore the reorientational motions of small linear alcohols in both bulk and nanoconfined systems. The remainder of the present Chapter describes some of the theoretical and experimental methods used to study molecular alcohol reorientation and also provides some experimental results on alcohol reorientation dynamics. Chapter 2 describes theoretical investigations of alcohol reorientation in the lower alcohols—methanol and ethanol—using equilibrium molecular dynamics simulations and attempts to explain the trend of slowed reorientation with increasing alkyl chain length. The molecular picture of reorientation developed in Chapter 2 is then applied to higher linear chain alcohols,

through *n*-hexanol, in Chapter 3. It is found that new reorientation dynamics emerge in simulation models of higher alcohols, and several hypotheses are tested to explain these dynamics. The emergence of new timescales in nanoconfined systems is addressed in Chapter 4 by considering the possible role of solute motion. Chapter 5 then provides preliminary results from non-equilibrium molecular dynamics in studying the role of the solute molecule motion in emergent timescales. The results presented in this work are summarized in Chapter 6, and ongoing and future directions for continued research are discussed.

1.1 Theory of Molecular Reorientation

To describe the dynamics of molecules in a liquid, one frequently invokes the Born-Oppenheimer approximation, in which electronic motions are assumed to be fast relative to the motions of heavier particles such as nuclei. In this spirit, electronic degrees of freedom are averaged, and in this way contribute to the force field, *i.e.*, the set of parameters used to describe the interactions among atoms comprising the liquid. The nuclear degrees of freedom, on the other hand, represent the atoms comprising the liquid. As an example, consider a methanol molecule. Each atom at some instant, t, has associated with it positions, velocities, and forces acting at the center of the atom—the nucleus. How this methanol molecule interacts with another molecule—and thus what its coordinates, velocities, and forces will be at a later time t'—is determined by the force field of the interacting atoms. In a classical view, the propagation of the system in time is thus achieved by calculating

the forces acting on each atom, integrating the equations of motion (by one of a number of methods), and updating positions and velocities. In this way, a classical molecular dynamics (MD) trajectory is constructed. The trajectory output, which includes positions as a function of time, can then be analyzed for quantities of interest, including molecular orientation in time for each molecule.

For an alcohol molecule at a given time, the vector $\underline{r}_{OH} = \underline{r}_H - \underline{r}_O$ describes the orientation of the hydroxyl group of the molecule. Normalizing by the vector magnitude $|\underline{r}_{OH}|$, one obtains $\underline{e}_{OH}$, a unit vector in the direction of the hydroxyl group. This quantity is calculated at some initial time, denoted $\underline{e}_{OH}(0)$, and at later times, t, as $\underline{e}_{OH}(t)$. The projection of the vector at time t onto its initial orientation at time zero ($t = 0$) can be calculated using the vector dot product, $\underline{e}_{OH}(0) \cdot \underline{e}_{OH}(t)$. When $t = 0$, this expression is equal to unity, and the "overlap" of the two vectors is complete. As the the hydroxyl group reorients in space over time, the dot product becomes less than unity, as it has the geometric interpretation that $\cos\theta(t) = \underline{e}_{OH}(0) \cdot \underline{e}_{OH}(t)$, where $\theta(t)$ is the angle the OH vector has rotated through in time t. Thus, one can relate the vector dot product to the angle through which the vector rotates in time t. This is represented in Figure 1.2.

The vector dot product $\underline{e}_{OH}(0) \cdot \underline{e}_{OH}(t) = \cos\theta(t)$ thus represents an orientational self-similarity—or autocorrelation—in time for some molecule. Experiments sensitive to molecular orientation measure the correlation function,

$$C_l(t) = \langle P_l[\underline{e}_{OH}(0) \cdot \underline{e}_{OH}(t)] \rangle. \tag{1.1}$$

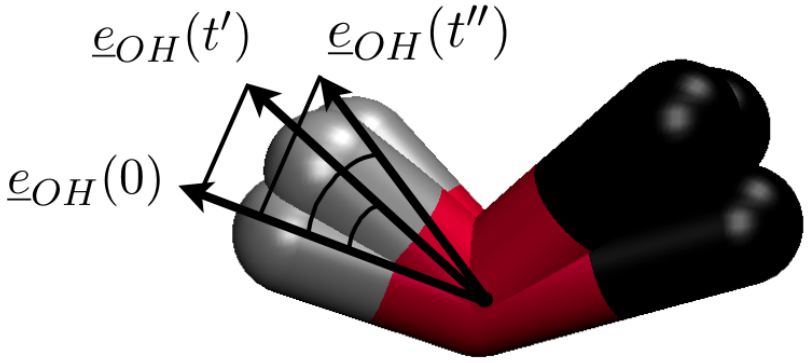

Figure 1.2: Schematic representation of the calculation of hydroxyl reorientation. A single methanol molecule is depicted at three times. Hydrogen is silver, oxygen is red, and the united atom carbon is blue. The $\underline{e}_{OH}(0)$ vector is shown to the left. The projections of this vector at later times, $t' > 0$ and $t'' > t'$ onto the vector at t_0 are also depicted, along with the corresponding angles, the key quantity in reorientation.

The brackets, $\langle - \rangle$, indicate averaging over the collection of time origins for all molecules (thermal averaging), and P_l is the l^{th} Legendre polynomial. Notably, different experiments measure different Legendre polynomials of the autocorrelation function (primarily the 1^{st} and 2^{nd}. For example, NMR and IR anisotropy experiments are both related to the second Legendre polynomial, $P_2 = \frac{1}{2}(3x^2 - 1)$, as discussed in Sections 1.2.1 and 1.2.4.

The key reorientational information about a system is contained in Equation 1.1. That information is frequently extracted by approximating $C_n(t)$ as a sum of exponential functions, as shown in Equation 1.2.

$$C_2(t) \approx \sum_{i=1}^{n} A_i e^{-t/\tau_i} \tag{1.2}$$

The interpretation of Equation 1.2 is that a process i that contributes to reorientation occurs with amplitude A_i with characteristic timescale τ_i. Thus each distinct process i, *e.g.* libration (see Section 1.1), is assigned a timescale. As usual, the physical interpretation of fitting to such functions is that at time $t = \tau_i$, an average of $\frac{1}{e}$ of the process i has yet to happen.

In the liquid state, the "collisions" of molecules constitute the fastest of such molecular motions. The condensed nature of the liquid state means that there is always another molecule nearby. Consequently, the mean-free path length is on the order of an Ångstrom or less, and the "collision frequency" in liquids is high. Because this motion is always occurring in a liquid, any experiment of sufficient temporal resolution reporting on molecular orientation beginning at times $t = 0$ and later will always capture a large population of molecules reorienting between their previous collisions and their next. Thus, the fastest-time component of molecular reorientation is always ascribed to this "inertial" component. While formally the inertial response is Gaussian, the averaged response it can be reasonably fit with an exponential function as in Equation 1.2.

Just after a collision, a molecule undergoes a rebounding motion. In terms of reorientation, the effect is to partially realign the vector of interest with its initial orientation vector. The partially restorative dynamics can be seen as small *increases* in $C(t)$ measurements and are often interpreted as the molecule "rattling around in a solvent cage." This type of librational motion is observed in all weakly interacting liquids and constitutes part of their reorientation response.

In networked liquids, where a directionality is imposed by specific interactions (*e.g.*, hydrogen bonds), librational motion takes on a qualitatively different character. In hydroxyl-bearing hydrogen bonded liquids, such as water and alcohols, the hydrogen bond donor (D) hydroxyl group on average is directed toward the oxygen atom of the hydrogen bond acceptor (A). Thermal motion allows displacement of the donor hydroxyl group away from the $O_D - O_A$ axis. Importantly, the oxygen and hydrogen atoms in this context can be viewed as having a partial negative and positive charges, respectively. Thus, displacements of the hydroxyl group are countered by a restoring force due to the hydrogen bond. The hydroxyl group, while participating in a hydrogen bond, therefore exhibits a wobbling motion within a cone, the geometry of which is dictated by the hydrogen bond strength[14]. This "librational" motion–including the restorative dynamics induced by the hydrogen bond–can be seen in sub-picosecond measurements of water reorientation.

The longest timescales—those observed after inertial and librational contributions—are traditionally associated with “diffusive” reorientational motion. However, the nature of this gross molecular reorientation is not well characterized, particularly in the case of networked liquids, for which theoretical and experimental descriptions have generally failed to agree. Common molecular-level theoretical models for long-time reorientation—and their failures and successes—are described in the next Section.

1.1.1 Debye Model of Reorientational Diffusion

The longest reorientation timescale has traditionally been associated with the Debye mechanism of reorientation. As applied to hydroxyl-bearing hydrogen bonded liquids, the Debye model [15] indicates that after a hydrogen bond breaks, the unnassociated hydroxyl group executes a series of random, small amplitude angular displacements until it achieves a hydrogen bond geometry with a new acceptor oxygen. That is, the long timescale comes from diffusive motion of free hydroxyl groups between hydrogen bond acceptors. The diffusive reorientation time can be described[15] by

$$\tau_n = \frac{1}{n(n+1)D_R}, \tag{1.3}$$

where n indicates the rank of the Legendre Polynomial, and D_R is the rotational diffusion constant. Importantly, one can calculate from simulation data ratios of n^{th}-order time constants as tests of the Debye model. Where the Debye model holds, $\tau_1/\tau_2 = 3$ and $\tau_1/\tau_3 = 6$.

1.1.2 Jump Model

In the jump model for reorientation first developed by Ivanov [16], this diffusive behavior is replaced by large amplitude angular jumps that occur as a consequence of a hydroxyl group switching between two hydrogen bond acceptors. The n^{th}-order timescale of this jumping motion can be described through geometric

considerations by

$$\tau_n^{jump} = \tau_0 \left[1 - \frac{1}{2n+1} \frac{\sin[(n+1/2)\Delta\theta]}{\sin(\Delta\theta/2)} \right]^{-1}. \tag{1.4}$$

In Equation 1.4, τ_0 represents the time characteristic of hydrogen bond jumping, where $\tau_0 = k_{jump}^{-1}$ and k_{jump} is the rate constant for switching hydrogen bond acceptors. As will be discussed later, of particular interest is the second-order reorientation time,

$$\tau_2^{jump} = \tau_0 \left[1 - \frac{\sin(5\Delta\theta/2)}{5\sin(\Delta\theta/2)} \right]^{-1} \tag{1.5}$$

These equations suggest that the time it takes a hydrogen bond switching event to occur depends on both the microscopic switch time and the geometry of the switch event. In the Ivanov jump model, the description of dynamics stops here. This suggests reorientation occurs only during hydrogen bond switches, while intact hydrogen bonds in water remain locked in place.

1.1.3 Extended Jump Model

In contrast to the Ivanov jump model [16], recent theoretical studies by Laage and Hynes[17–19] have indicated that the long timescale for water reorientation arises from a combination of two effects: a fast, large-amplitude switch between hydrogen bond acceptors and the tumbling motion of an intact hydrogen bond between these switches. In this extended jump model, depicted in Figure 1.3, the overall long timescale associated with water reorientation is then described by

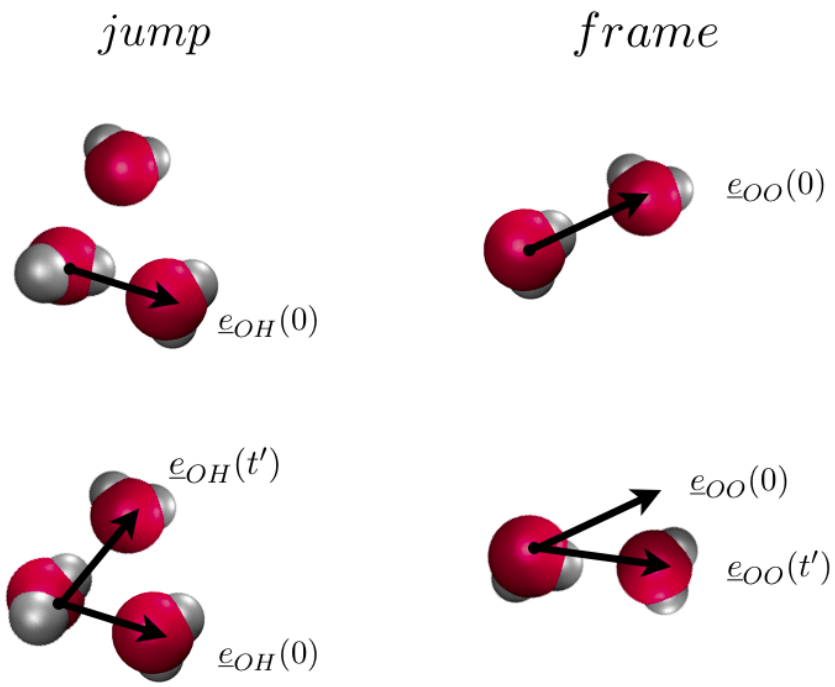

Figure 1.3: Two mechanisms account for longtime reorientation in water in the extended jump model. During hydrogen bond "jumps" (Left), the orientation of a hydroxyl group changes in time as a consequence of switching hydrogen bond acceptors. During "frame" reorientation (Right), the hydroxyl group reorients in-frame with its hydrogen bond acceptor. For the jump and frame mechanism, the $\underline{e}_{OH}$ and $\underline{e}_{OO}$ vectors are shown at $t = 0$ and $t = t'$ to highlight the angular displacement for each type of motion.

$$\frac{1}{\tau_2} = \frac{1}{\tau_2^{jump}} + \frac{1}{\tau_2^{frame}}. \tag{1.6}$$

The right side of Figure 1.3 indicates that the frame time is calculated using the reorientation of the $\underline{e}_{OO}$ vector, rather than the $\underline{e}_{OH}$ vector. The inclusion of the librational motion of the OH group wobbling around the $\underline{e}_{OO}$ vector has little effect on τ_2^{frame}, and the motion of the $\underline{e}_{OO}$ vector is tracked instead.

In the extended jump model, the transition state for a water molecule reorienting between an old and a new hydrogen bond acceptor (shown in Figure 1.4) is symmetric in the coordinates $R^{\ddagger}_{O_D-O_A}$ and $R^{\ddagger}_{O_D-O_B}$. Similarly, for the hydrogen bond jump, the vector $\underline{e}_{O_D-H_D}$ bisects the $O_B - O_D - O_A$ angle. Thus, as the current acceptor molecule A moves away from the donor D and the new acceptor B approaches, the identity of the hydrogen bond acceptor is lost and A and B are equally plausible hydrogen bond partners. Importantly, in water the future acceptor B generally approaches from the second solvation shell, which is a slightly activated process.

The extended jump model has been further developed to provide simple explanations for changes to water reorientation rates through both entropic and enthaplic considerations, which have been applied successfully to a number of situations showing aberrant reorientation dynamics, including reorientation about hydrophobic solutes[20], emergent reorientation timescales in supercooled water[21], and increased reorientation around certain hydrophilic and amphipathic solutes[22–24].

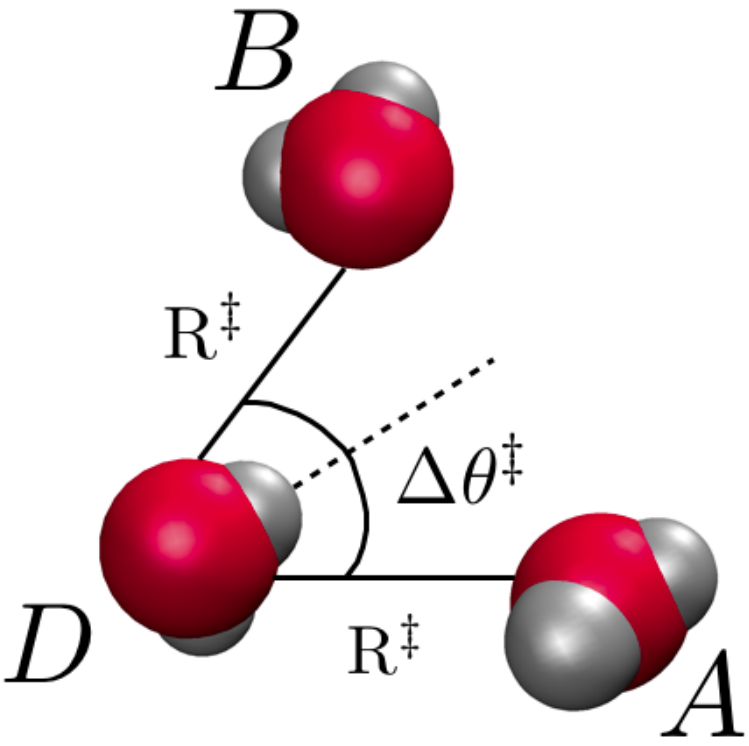

Figure 1.4: The transition state for water hydrogen bond switching in the extended jump model is symmetric. Oxygen atoms (red) and hydrogen atoms (silver) are shown for the hydrogen bond donor (D), the previous acceptor (A), and the future acceptor (B). At the transition state, the $R^{\ddagger}_{O_D-O_A}$ and $R^{\ddagger}_{O_D-O_B}$ distances are the same, and the donor hydroxyl bisects the $\Delta\theta^{\ddagger}_{O_B-O_D-O_A}$ transition state angle.

1.2 Experimental Measurements of Reorientation

Several experimental methods can be used to measure reorientation in alcohols. In the case of NMR, the results indicate slower reorientation with longer alkyl chain length. Other techniques measuring dynamics in liquids have only been sparsely applied to alcohols, but deserve mention for their potential utility in future experimental investigations.

1.2.1 Nuclear Magnetic Resonance

Nuclear magnetic resonance (NMR) has been used to measure the O-H intramolecular reorientation for water [25] and linear chain alcohols [26–29]. By titration of $CD_3(CD_2)_n^{17}OH$ in $CD_3(CD_2)_n^{16}OH$, one can obtain a reliable estimate of the hydroxyl proton relaxation rate in $CD_3(CD_2)_n^{16}OH$. In essence, the ^{17}O magnetically active nucleus provides an additional relaxation pathway for the proton. Measurement of relaxation over the isotopic mole fraction series allows one to extrapolate the longitudinal relaxation (T_1) time back to that for the pure, unlabeled alcohol. The results of such an experiment across a series of short chain linear alcohols at 298 K are provided in Table 1.1.

The NMR approach has the advantage that the reorientation of specific bonds can be measured. However, because the NMR measurement is slow, it reports only the average or integrated timescale,

$$\langle \tau \rangle = \int_0^\infty C_2(t)\,\mathrm{d}t. \tag{1.7}$$

Table 1.1: NMR hydroxyl reorientation times (in ps), Eq. 1.7

Molecule	$\langle\tau\rangle$
Water	2
Methanol	5
Ethanol	18
n-Propanol	33
n-Butanol	51
n-Pentanol	72
n-Hexanol	89

Notably, Equation 1.7 also indicates that NMR is sensitive to the second-order Legendre polynomial in the reorientation correlation function, as in Equation 1.1. Accordingly, the $C_2(t)$ correlation function of the $\underline{e}_{OH}$ bond vector (described in Section 1.1) can be calculated and integrated to compare directly with these experiments. Importantly, while the trend that hydroxyl reorientation is a function of the length of the rest of the molecule is both immediately obvious (Table 1.1) and fundamentally interesting, no mechanistic explanation for this trend has been pursued previously.

1.2.2 Optical Kerr Effect Spectroscopy

Among non-linear spectroscopic methods, optical Kerr effect (OKE) spectroscopy is particularly well-suited to studying molecular reorientation and has the advantage that no labeling of the molecule of interest is required. In OKE spectroscopy (reviewed in [30]), a strong laser field induces a partial alignment of molecular dipoles in an otherwise isotropic medium. This anisotropic ordering results in an optical birefringence, which can be measured with another laser pulse. The

inducing field is eliminated, and the birefringence is monitored. The decay of the birefringence is then a measure of reorientation of the liquid molecules—it disappears as the molecular orientations randomize. Thus, OKE spectroscopy reports on librational and diffusive motions.

While the decay in induced birefringence would provide valuable information about reorientation dynamics in alcohols, no studies focused on reorientation dynamics have been conducted. Instead, several OKE spectroscopic studies of alcohols have focused instead on molecular structure, rather than dynamics. The optical Kerr constant, B_0, is related to the applied electric field, $\langle E \rangle$, the probe wavelength, λ_p, and the change in index of refraction, δn, through the expression

$$B_0 = \frac{\delta n}{\lambda_p \langle E \rangle^2} \tag{1.8}$$

Accordingly, B_0 is taken as a measure of the field-induced collective molecular ordering in the liquid.

In studies of *n*-alcohols, the Kerr constant, B_0, increases for increasing alkyl chain length, which has been interpreted as the growth of greater structural order in longer alcohols [31, 32]. Notably, in lower alcohols (methanol, ethanol), linear relationships between the number of alkyl carbons and the Kerr constant are observed, while for higher alcohols (*n*-propanol and longer), relationships become nonlinear[31, 32]. Theoretical studies aimed at direct comparison with OKE results for linear chain liquid alcohols are, at this time, absent from the literature. Similarly, OKE experiments reporting reorientation dynamics in alcohols are lacking.

1.2.3 Two-dimensional Infrared Spectroscopy

Two-dimensional infrared (2D-IR) spectroscopy is an extension of more common infrared spectroscopy, in which light in the IR region of the spectrum excites molecular vibrational modes. While the technique is not specific to reorientation, *per se*, it can be used to infer local dynamics and also monitor hydrogen bond switching. In 2D-IR, a pump pulse excites a vibrational mode in a reporter molecule (*e.g.*, dilute *ROD* in *ROH*). A second probe pulse is then introduced at some variable time delay. When the time delay is short, stimulated emission to the vibrational ground state as well as excitation to the second vibrational excited state are observed as narrow peaks. When the time delay is increased, the environment around the reporter molecule has time to change, which results in a distribution of frequencies for both stimulated emission and second excitation for the reporter molecule (spectral diffusion). Thus, the 2D-IR lineshape as a function of time reports on local rearrangements, including contributions from molecular reorientation.

Additionally, hydrogen bonding can be monitored directly as a function of time using 2D-IR spectroscopy. Hydrogen bonded *ROD* and non-hydrogen bonded *ROD* comprise a simple two state system. For a pump probe peak specific to one of these—hydrogen bonded *ROD*, say—a pulse at a later time will result in the simple stimulated emission / second excitation pair if the hydrogen bond remains intact. If, however, between the pump and the probe, the hydrogen bond is broken, a cross peak results due to the frequency change in the OH stretch. Thus, with proper peak assignment, one can monitor the chemical exchange dynamics of hydrogen bonding.

Several IR and multidimensional-IR studies of alcohol dynamics have been performed[33–41]. However, the alcohol is frequently dissolved in solvent (carbon tetrachloride), and the vibrational lifetime is monitored as a function of alcohol concentration. The focus of these studies, then, is on non-networked monomers or small oligomers, rather than the neat liquid. While in some cases useful vibrational lifetime information can be derived, a comprehensive set of data for a series of alcohols is lacking.

1.2.4 Infrared Pump-probe Anisotropy Measurements

Information concerning the motion and local environment of specific bonds can also be obtained from vibrational pump-probe anisotropy experiments. A infrared pump pulse excites a vibration from the ground state, ν_0, to its first excited state, ν_1. Then, a time-delayed probe pulse polarized parallel or perpendicular to the pump pulse is used either to further excite the vibrational mode ($\nu_1 \rightarrow \nu_2$) or stimulate it back to the ground state ($\nu_1 \rightarrow \nu_0$). The parallel and perpendicular absorption changes associated with the probe pulses can be monitored as a function of time. If the molecule has not rotated, the parallel intensity is maximal, while the perpendicular signal is zero. The perpendicular signal grows in as the molecule rotates in time. This information can be recast as the anisotropy decay

$$r(t) = \frac{I_{\parallel}(t) - I_{\perp}(t)}{I_{\parallel}(t) + 2I_{\perp}(t)} \approx \frac{2}{5} C_2(t), \tag{1.9}$$

which therefore provides rotational information about specific bonds, including hydroxyl groups. In most cases, $r(t) = \frac{2}{5}C_2(t)$, although theoretical studies indicate that other factors, such as non-Condon effects, may change the exact form of $r(t)$ [42].

While anisotropy decay experiments on dilute HOD in H_2O have provided valuable information about reorientation and vibrational energy transfer dynamics in liquid water[43, 44], analogous pump-probe anisotropy studies of alcohols have not been pursued.

1.3 Time-dependent Fluorescence Spectroscopy

Another widely employed technique for reporting dynamics in liquids is time-dependent fluorescence (TDF) spectroscopy. In contrast to the methods previously described, in which the dynamics of molecules comprising a liquid are probed directly, TDF employs a reporter dye or solute dissolved in the liquid under investigation.

The TDF process is shown schematically in Figure 1.5. At times $t < 0$, the solvent molecules interact with the ground-state charge distribution of the solute molecule. At some time $t = 0$, a high energy photon promotes the dye molecule to its excited state (upward, purple arrow in Figure 1.5). In the Franck-Condon approximation, the electronic charge redistribution of the solute occurs instantaneously with respect to the nuclear coordinates of both the solute and the surrounding solvent. (The upward, purple arrow is vertical, reflecting the fact that no change

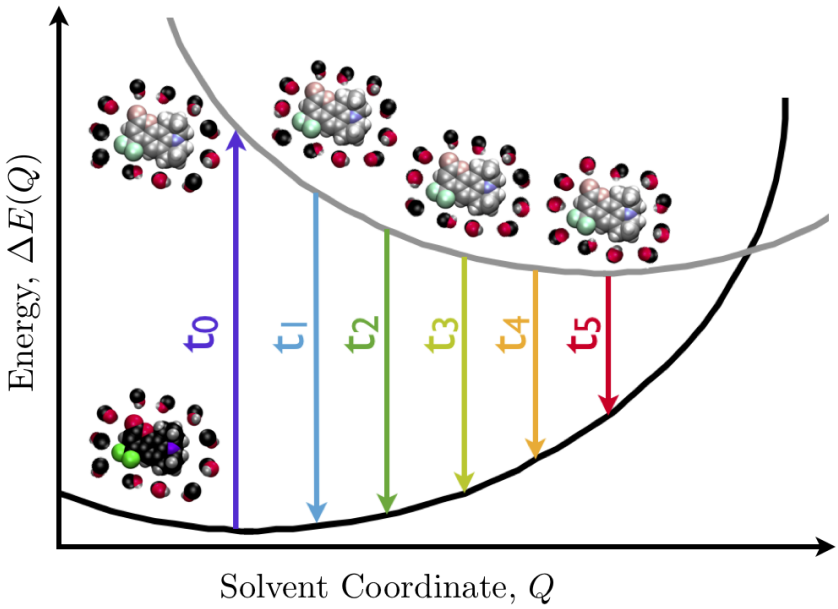

Figure 1.5: Time-dependent fluorescence is generally described by the difference in energy between the ground and excited state of a dye molecule as a function of the solvent coordinate over time. In the Figure, a ground state dye molecule (bold colors) is solvated by methanol molecules with little to no preferred orientation around it. At time $t = 0$ (purple arrow), absorption of a photon results in an excited dye molecule (pastel colors). The solvent gradually reorganizes to stabilize the new charge distribution of the excited state dye molecule. Therefore, at later times, energy lost from the dye as a photon (colored arrows) is red-shifted relative to the photon involved in excitation.

has occurred in the generalized solvent coordinate, Q.) This implies that the solvent is now in a non-equilibrium configuration with respect to the new charge distribution of the solute. The excited state charge distribution is subsequently stabilized by reorientation (and translation) of the surrounding solvent molecules. (This is depicted by the sequence of excited state solute/solvent configurations that decrease in energy for subsequent solvent coordinates, Q.) After excitation, the solute molecule can return to its electronic ground state by emitting a photon. The fluorescence wavelength of the emitted photon is therefore a function of the response time of the medium and is longer than the wavelength of the absorbed photon. (This is depicted by the sequence of downward arrows of different colors. The magnitudes of the arrows representing emission are decreased relative to that of the excitation, and the colors schematically reflect the extent of red-shifting.)

The dynamics in the general solvent coordinate Q are thus frequently quantified as changes to the fluorescence energy over time. Importantly, $\Delta E_{fl}(0)$ (purple curve) and $\Delta E_{fl}(\infty)$ are constant values, and as such, do not contribute to the response. The change in the fluorescence energy can then be taken as the difference between its value at some time t after excitation and $t \to \infty$, when the value is no longer changing. This difference can also be normalized according to,

$$S(t) = \frac{\Delta E_{fl}(t) - \Delta E_{fl}(\infty)}{\Delta E_{fl}(0) - \Delta E_{fl}(\infty)}, \tag{1.10}$$

by dividing by the largest difference in the fluorescence energy (between time t_0 and $t \to \infty$). The normalized time-dependent Stokes shift, Equation 1.10, thus

starts at 1 at $t = 0$ and decays over time to 0 at $t \to \infty$. In this sense, timescales in $S(t)$ are taken to report on the molecular motions that stabilize the excited-state charge distribution.

1.4 Reorientation in Confined Systems

All of the preceding descriptions of experiments on liquid systems have been restricted to bulk systems. In bulk systems, the medium extends sufficiently far in each direction that any effects from interactions with the containing vessel (*e.g.*, cuvette, beaker, etc.) contribute negligibly to any measured signal. That is, the surface area-to-volume ratio is typically very low. In contrast to this, confining frameworks with dimensions on the order of only a few molecular diameters have a much larger surface area-to-volume ratio, and experimental signals comprise contributions from molecules interacting with the vessel interface as well as molecules interacting directly only with other liquid molecules in the vessel interior. Examples of such nanoconfining frameworks include sol-gels, micelles, reverse-micelles, and carbon nanotubes, among others.

One consequence of the nanoconfinement of liquids is a general retardation of their dynamic properties. The methods previously described and applied to bulk systems—NMR, OKE spectroscopy, and 2D-IR spectroscopy—all show generally increased reorientational timescales. However, the most interesting results for dynamics in confined systems come from time-dependent fluorescence (TDF) measurements, in which the number of observed timescales exceeds that in the

corresponding bulk case. That is, the functions $S(t)$ for a given solute and solvent are often fit to a larger number of exponential functions in confined systems than in bulk systems, and these emergent timescales—those with no bulk counterpart—are observed more commonly than not.

In general, models to explain these emergent timescales in nanoconfined systems have been directed toward changes in solvent motions. As it is unlikely that confinement induces some new type of solvent motion, it has been suggested that additional timescales results from the partitioning of solvent dynamics between those at the interface and those in the confining framework interior. However, such a two-state model [45–50] cannot account for the emergence of multiple additional timescales, which has been experimentally observed[1, 51–64]. Similarly, in the dynamic exchange model [65–70], in which bound interfacial solvent does not contribute to reorientation, the exchange between bound and bulk-like molecules (in the interior) is suggested to contribute a new reorientation timescale. However, experiments and simulations[71–81] both indicate that molecular processes—including reorientation— occur at the framework interface, but on slower timescales than bulk-like molecules.

The emergent dynamics often observed in nanoconfined systems may originate with motion of the solute itself. Whereas bulk systems are isotropic, in nanoconfined systems, the framework introduces anisotropy, and molecular properties along directions normal and tangential to the confining interface are often different. For example, in a cylindrical silica pore, the rate of solute diffusion toward the interface may be different than the rate of diffusion along the pore axis. Thus, it is

plausible that spectral properties of a solute may also change in confinement, and that new timescales in TDF experiments in nanoconfined systems are associated with solute motions. Such a hypothesis has been proposed[68, 73, 75, 78], although no definitive tests, experimental or theoretical, have been conducted. Thus, the origin of emergent timescales in TDF spectra of nanoconfined systems is still not understood, but is required for proper interpretation of TDF spectra and solvent (and possibly solute) dynamics.

1.5 Goals of the Present Work

Several phenomena with regard to reorientation dynamics remain unexplained. The trend that alcohol reorientation timescales increase with increasing chain length has been experimentally observed, although no mechanism for this has been proposed and tested. New timescales emerge in TDF spectra. Both the extended jump model for supercooled water and the solute diffusion hypothesis predict the emergence of new timescales, but neither hypothesis has been theoretically investigated. The goal of the present work is to explore using MD simulations the origins of trends and new timescales that appear experimentally in bulk and confined alcohol systems. While this work is not exhaustive, it is hoped that it represents a small but strong foundation on which subsequent studies can build.

Chapter 2

Lower Alcohol Reorientation Dynamics

Alcohols are frequently employed as solvents for their cost effectiveness, simple synthesis, low toxicity, and modest environmental impact. Of these, the better-studied [25–29, 33–41, 82–119] lower alcohols—methanol and ethanol—are often chosen. As discussed in Section 1.2, the timescale on which the hydroxyl group in alcohols reorients is a function of the alkyl chain length. Thus, processes in which solvent reorientation is key can, in principle, be better controlled through an informed choice of solvent. A particularly important example of this is reaction dynamics, and specifically nucleophilic substitution and elimination reactions, in which charge stabilization of transition states and/or intermediates through solvent reorganization is critical. The reaction rate constants are thus, in principle, controllable through fine-tuning of the reaction medium, and a fundamental understanding of alcohol reorientation can facilitate rational design in reaction chemistry.

Recently, the extended jump model has received attention for its ability to theoretically explain experimental measurements on water reorientation [14, 17–24]–

particularly in cases where previous models have failed. The structural similarity between water, $H-O-H$, and alcohols, $R-O-H$, suggests that alcohol OH reorientation may occur by mechanisms similar to that of water due to the central role of hydrogen bonding. Accordingly, in this Chapter the analysis of molecular dynamics (MD) simulation trajectories to explore hydroxyl group reorientation mechanisms in lower alcohols is discussed.

2.1 Simulation Methods

Water reorientation has been successfully investigated using classical MD and interaction models using fixed charges. Here, a similar approach has been taken with water and the lower alcohols—methanol and ethanol. Water was described using the Simple Point Charge Extended (SPC/E) model [120]. Methanol and ethanol were modeled based on the Optimized Potentials for Liquid Simulation United Atom (OPLS-UA) potential of Jorgensen [121, 122]. The force field parameters for water and the lower alcohols are listed in Table 2.1. In addition to fixed charges, the models use fixed bond lengths and fixed bond angles; accordingly, no force constants for bond stretching or bending are provided. The torsional potential of ethanol is handled by a Fourier series of the form

$$V(\phi) = V_0 + \frac{1}{2}V_1(1+\cos\ \phi) + \frac{1}{2}V_2(1-\cos\ 2\phi) + \frac{1}{2}V_3(1+\cos\ 3\phi) \qquad (2.1)$$

Table 2.1: Force field parameters for water and lower alcohols

Atom	m (g mol^{-1})	q (e)	σ (Å)	ε (kJ mol^{-1})
H_{water}	1.0079	0.4238	0.0000	0.00000
O_{water}	15.999	0.8476	3.1660	0.65000
$H_{alkanol}$	1.01	0.435	0.0000	0.00000
$O_{alkanol}$	16.00	-0.700	3.0700	0.71128
C_1	14.03	0.265	3.9050	0.49371
C_2	15.04	0.000	3.7750	0.86609
Atoms AB	HO_{water}	$HO_{alkanol}$	OC	CC
R_{AB} (Å)	1.0	0.945	1.430	1.530
Atoms ABC		HOH	HOC	OCC
Θ_{ABC} (°)		109.47	108.5	108.0
ϕ_{HOCC}	$V_0^{\dagger}$	V_1	V_2	V_3
	0.000	3.48947	-0.48535	3.12546

† All torsional parameters are provided in kJ mol^{-1}.

Intermolecular interactions between two sites A and B are described by Coulombic and van der Waals terms (represented by a Lennard-Jones potential), which are provided in Equations 2.2 and 2.3.

$$V_{Coul}(r_{AB}) = \frac{1}{4\pi\varepsilon_0}\frac{q_A q_B}{r_{AB}} \tag{2.2}$$

$$V_{LJ}(r_{AB}) = 4\varepsilon_{AB}\left[\left(\frac{\sigma_{AB}}{r_{AB}}\right)^{12} - \left(\frac{\sigma_{AB}}{r_{AB}}\right)^{6}\right] \tag{2.3}$$

In these equations, A and B represent the identities of the interacting sites, r_{AB} is the distance between them, q_α represents the electrostatic charge of site α, σ_{AB} represents the AB distance at which the interaction energy is zero, and ε_{AB} represents the strength of interaction. Values for σ_{AB} and ε_{AB}, where $A \neq B$, for the

lower alcohols have been calculated according to the standard Lorentz-Berthelot combining rules.

$$\sigma_{AB} = \frac{\sigma_{AA} + \sigma_{BB}}{2} \tag{2.4}$$

$$\varepsilon_{AB} = \sqrt{\varepsilon_{AA}\varepsilon_{BB}}. \tag{2.5}$$

Force field parameters for these intermolecular interactions are also provided in Table 2.1.

Classical MD simulations were performed using the DL_POLY_2 software package[123]. Water, methanol, and ethanol simulations contained 343, 385, 264 molecules in cubic boxes of lengths 21.725311, 30, and 30 Å, respectively. The resulting liquid densities were 1.00, 0.759, and 0.748 g cm^{-3}. Lennard-Jones interactions (Equation 2.3) and Coulombic interactions (Equation 2.2), were applied with a cut-off distance of 10.5 Å and 15 Å for water and the alcohols, respectively. Long-range electrostatics were handled using an Ewald sum, with α = 0.25 and a $10 \times 10 \times 10$ k-point grid for fast Fourier transformation. Simulations were run in the NVT ensemble, using a Nosé-Hoover thermostat[124, 125] with a 1 ps time constant. With the exception of the calculation of the activation energy of hydrogen bond switching, all calculations and analyses use simulation trajectories collected at 298 K. For water, methanol, and ethanol, simulations were performed for a range of temperatures to determine the activation energy of hydrogen bond switching. The trajectory lengths for all temperature simulations are provided in Table 2.2. In each case, a 500 ps equilibration was followed by the data collection stages presented in Table 2.2. For all simulations, a 1 fs time step was used,

Table 2.2: Trajectory lengths (in ns) of the simulations

	280 K	298 K	320 K	340 K	360 K
H_2O	2	2	1	1	1
CH_3OH	5	2	1	1	1
CH_3CH_2OH	4	10	4	4	4

and configurations were written every 8 fs. Uncertainties were calculated at a 95% confidence interval using the Student's t-test[126] and 10 blocks for block averaging.

2.2 Applicability of the Extended Jump Model

The extended jump model developed by Laage and Hynes[17, 18] and applied to liquid water has excellent theoretical and experimental support. (See Section 1.1.3.) This is not the case for the Debye mechanism for water reorientation. That is, the slow angular diffusion of hydroxyl groups is suggested not to occur in water. Instead, the extended jump model posits that hydroxyl groups reorient quickly and with large amplitude during the switching of hydrogen bonding partners as well as more slowly during the tumbling of an intact hydrogen bond. Thus, a natural initial test of the applicability of the extended jump model to liquid alcohols is to determine if free hydroxyl groups persist in the bulk liquid. Persistent and slow reorientation of non-hydrogen bonded hydroxyl groups would support the Debye mechanism, while an absence of such behavior would instead favor the extended jump model.

To this end, one can define a hydrogen bond in a classical MD simulation in several ways. The simplest among these uses purely geometric criteria involving interatomic distances and angles [127]. For example, the definition used in the present studies is that a pair of molecules, labeled D (donor) and A (acceptor), are considered hydrogen bonded if $R_{H_D-O_A} < 2.15$ Å, $R_{O_D-O_A} < 3.10$ Å, and $\Theta_{H_D-O_D-O_A} < 20^\circ$. One can thereby calculate the time for which a "free" hydroxyl group remains non-hydrogen bonded. Mathematically, this can be calculated using a side-side correlation function,

$$C_{NHB}(t) = \langle \theta_{NHB}(0)\, \theta_{HB}(t) \rangle \tag{2.6}$$

Here, θ_{NHB} is a binary function that a molecule donates No Hydrogen Bond. Similarly, θ_{HB} is a binary function that a molecule donates a Hydrogen Bond. This is better illustrated as

$$\theta_{NHB}(t) = \begin{cases} 1 & \text{when the selected molecule has no} \\ & \text{hydrogen bond } (NHB) \text{ acceptor at } t \\ & \\ 0 & \text{when the selected molecule has a}t \\ & \text{hydrogen bond acceptor at } t \end{cases}$$

$$\theta_{HB}(t) = \begin{cases} 0 & \text{when the selected molecule has no} \\ & \text{hydrogen bond acceptor at time } t \\ & \\ 1 & \text{when the selected molecule has} \\ & \text{a hydrorgen bond at time } t \end{cases}$$

Note that $\theta_{NHB}(t) = 1 - \theta_{HB}(t)$. Thus, at $t = 0$, the product $\theta_{NHB}(0)\theta_{HB}(0)$ is always zero. When a hydrogen bond acceptor for the selected molecule is found at some later time, t, $\theta_{HB}(t) = 1$. The, the product $\theta_{NHB}(0)\,\theta_{HB}(t) = 1$, and remains so for all later times when absorbing boundary conditions are applied. The imposition of absorbing boundary conditions means the correlation function reports only on the dynamics of the direct formation of a hydrogen bond. This is a simple step function in time, in which the step represents the switch from non-hydrogen bonded to hydrogen bonded for a single molecule. Averaging over all molecules and time origins results in a smooth curve, $C_{NHB}(t)$, which is related to the dangling hydroxyl survival time, $S_{NHB}(t)$, by the simple equation

$$S_{NHB}(t) = 1 - C_{NHB}(t). \tag{2.7}$$

The results of this calculation for methanol and ethanol are presented in Figure 2.1. Notably, the curves in Figure 2.1 were generated using the force field described in Section 3.1. Both curves can be well fit (to $C_2(t) \approx 1\%$) using a 2-exponential function. For methanol, the two time constants are 0.34 and 1.01 ps, while for

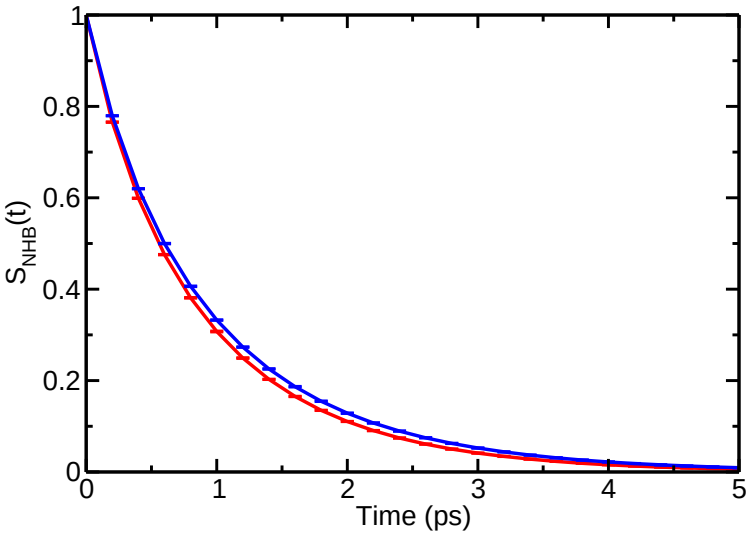

Figure 2.1: The timescales for free hydroxyl groups to find a hydrogen bond partner are reflected in the free hydroxyl survival probability as a function of time, $S_{NHB}(t)$, for both methanol (red) and ethanol (blue).

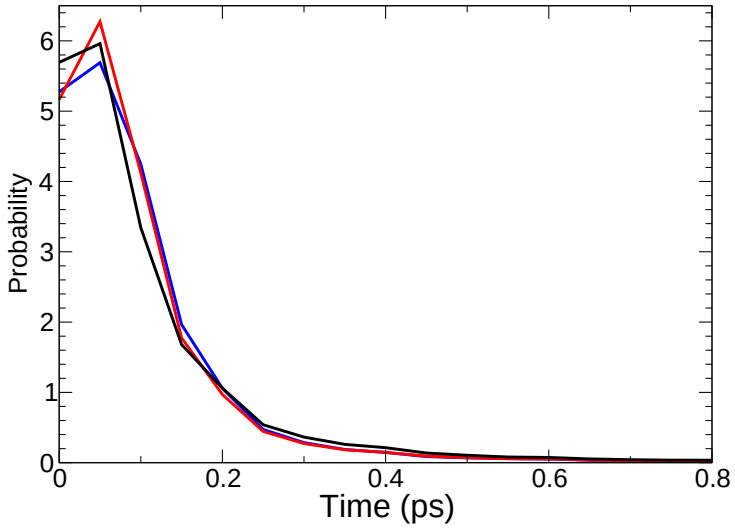

Figure 2.2: The distributions of waiting times for a free hydroxyl group to find an acceptor molecule are plotted for water (black), methanol (red), and ethanol (blue).

ethanol, these are 0.39 and 1.12 ps. That is, the lifetime of a non-hydrogen bonded hydroxyl group is short for the lower alcohols.

Alternatively, one may examine the distribution of the time a free hydroxyl group persists, *i.e.*, how long it takes a non-hydrogen bonded hydroxyl group to find a new acceptor molecule. The result of such a calculation is presented in Figure 2.2. The results show clearly that few "dangling" hydroxyl groups persist beyond 1 ps, and the curves for water, methanol, and ethanol overlap one another almost completely. Together, Figures 2.1 and 2.2 indicate that there are not long-lived dangling OH groups, and therefore alcohol reorientation does not occur by a slow

diffusive mechanism like that proposed by Debye. Thus, alternative reorientation mechanisms such as the extended jump model must be investigated.

2.3 Hydroxyl Reorientation Times

To investigate the mechanism by which alcohols reorient, the employed models must capture the experimentally observed trend in reorientation times, *i.e.*, that hydroxyl reorientation slows with increasing alkyl chain length. To validate the models used here, the simulation trajectories have been mined for the hydroxyl reorientation times. The correlation functions, $C_2(t)$ (Equation 1.1), for water, methanol, and ethanol have been calculated and are presented in Figure 2.3. Assuming that the processes that contribute to hydroxyl reorientation occur on distinct timescales, the expression for $C_2(t)$ can be fit as a sum of exponential functions, each of which corresponds to a process with its own timescale. (See Section 1.1.) The curves in Figure 2.3 can be well-fit (to $C_2(t) \approx 1\%$) using a 3-exponential function of the form Eq. 1.2. The longest of these timescales, traditionally denoted τ_2 when considering $C_2(t)$, is of particular interest, as it represents the timescale of the diffusive reorientational motion. The values of τ_2 for water, methanol, and ethanol are 2.6 ± 0.1, 5.5 ± 0.3, and 12.1 ± 1.7 ps, respectively. Thus, the reorientation time increases with increasing alkyl chain length. The average time constants for water, methanol, and ethanol are $\langle \tau \rangle = 1.7 \pm 0.1, 3.3 \pm 0.3$, and 6.3 ± 1.8 ps, respectively, which are shorter than then NMR-measured values of $1.7 - 2.6$[25, 27, 128] for water, 5[26, 29, 129] for methanol, and 12.7 and 18

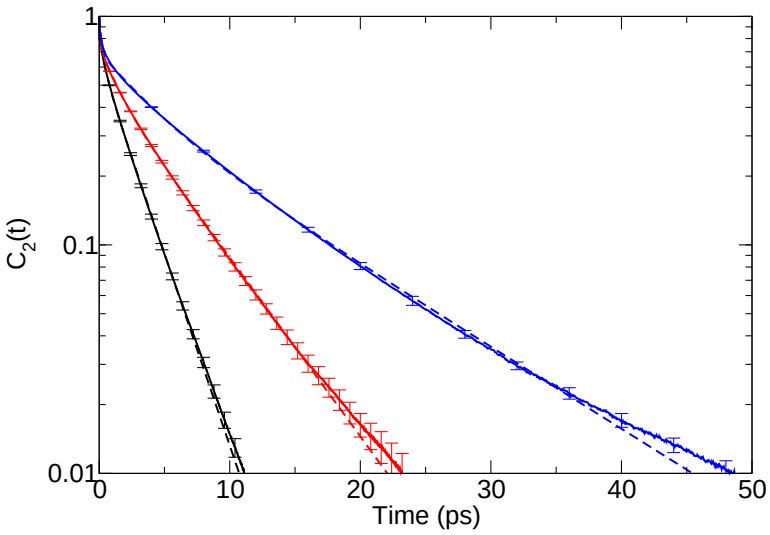

Figure 2.3: Reorientational correlation functions for water (black), methanol (red), and ethanol (blue). Three-exponential fits to each function are represented by dashed lines of the corresponding color.

ps[28, 118] for ethanol, but gives the same trend for the series. The fact that this trend in theoretical models follows those derived from experimental results (see Table 1.1) indicates that these models can be used to examine the origin of the trend.

In the extended jump model, hydroxyl reorientation of water is viewed within the context of hydrogen bonding; a hydroxyl group is either in the midst of a fast, large angle switch or "jump" between hydrogen bond partners or is tumbling in solution with its hydrogen bond partner. Each of these rate processes (See Section 1.1) has associated with it a rate constant, such that

$$k_2 = k_2^{jump} + k_2^{frame}.$$

Thus, the two timescales involved, τ_2^{jump} and τ_2^{frame}, respectively, are related to the reorientation time τ_2 by

$$\frac{1}{\tau_2} = \frac{1}{\tau_2^{jump}} + \frac{1}{\tau_2^{frame}}. \tag{2.8}$$

The jump time contribution and frame time contribution are now examined in turn for water, methanol, and ethanol.

2.4 Lower Alcohol Jump Times

The timescale for a hydroxyl group to reorient from one acceptor to another is a function of the rate constant for hydrogen bond exchange and the angle traversed

in the exchange. The jump time contribution, τ_2^{jump}, to the full reorientational timescale, τ_2, is therefore described mathematically by the equation []

$$\tau_2^{jump} = \tau_0 \left[1 - \frac{\sin(5\Delta\theta/2)}{5\sin(\Delta\theta/2)} \right]^{-1}. \tag{2.9}$$

Here, τ_0 is the characteristic hydrogen bond jump time and $\Delta\theta$ is the jump angle. (Note that to distinguish between these timescales, τ_2^{jump} is called "the jump time contribution to τ_2" and τ_0 is called simply "the jump time.") From Equation 2.9, it is clear that both the hydrogen bond jump time and the jump angle can change the τ_2^{jump} contribution. After constructing from the trajectory a list of the hydrogen bond switch times and the molecules participating in each switch, it is possible to calculate the jump angle, $\Delta\theta$ or the O_A-O_D-O_B angle, for each switching event. Here, A is the previous hydrogen bond acceptor molecule, D is the hydrogen bond donor molecule, and B is the new hydrogen bond acceptor molecule. The distribution of jump angles calculated this way is shown in Figure 2.4. Notably, for all species, the jump angle distributions are qualitatively similar. Water, methanol, and ethanol each display a global probability maximum near $\Delta\theta = 50^\circ$, a broad shoulder that begins near 60°, and a decay in probability that gradually decreases to 0 at 180°. The global maximum is smallest for water, which also has the correspondingly largest shoulder. The maximum is largest for ethanol, which has the correspondingly smallest shoulder. That is, the major differences in $P(\Delta\theta)$ across the series are in the relative weighting of the sharp peaks and broad shoulders. The asymmetry of these distributions leads to slightly different average

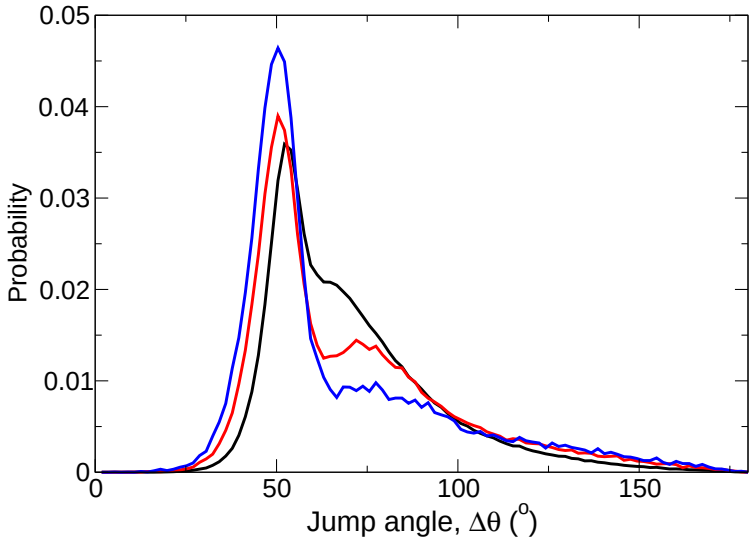

Figure 2.4: Distribution of hydrogen bond jump angles for water (black), methanol (red), and ethanol (blue).

jump angles across the series calculated as

$$\langle \Delta\theta \rangle = \int_0^{\pi} \Delta\theta \, P(\Delta\theta) \sin(\Delta\theta) \, \mathrm{d}\Delta\theta, \tag{2.10}$$

where

$$\int_0^{\pi} P(\Delta\theta) \sin(\Delta\theta) \, \mathrm{d}\Delta\theta = 1. \tag{2.11}$$

These averages for water, methanol, and ethanol are $\langle \Delta\theta \rangle = 68^\circ$, 71°, and 68°, respectively. This implies that the average hydrogen bond exchange mechanisms for water, methanol, and ethanol involve approximately the same angular geometry. The origin of the differences among angular distributions for water, methanol, and ethanol is discussed in Section 2.4.2.

Because there is little change in the average jump transition state geometry between the lower alcohols and water, any change in the jump contribution to τ_2 must come from the hydrogen bond jump time, τ_0. The hydrogen bond jump times can also be calculated using a side-side correlation function, of the form

$$C_{AB}(t) = \langle \, \theta_{DA}(0) \, \theta_{DB}(t) \, \rangle. \tag{2.12}$$

This is similar to the correlation function in Equation 2.6. Here, if at time $t = 0$, a molecule, D, donates a hydrogen bond to an acceptor molecule, A, $\theta_{DA}(0) = 1$. The donation by molecule D at $t = 0$ to another molecule B is then zero, because a single hydroxyl group donates to only one acceptor. (While double donation in these systems according to the geometric criteria has been observed, it is exceed-

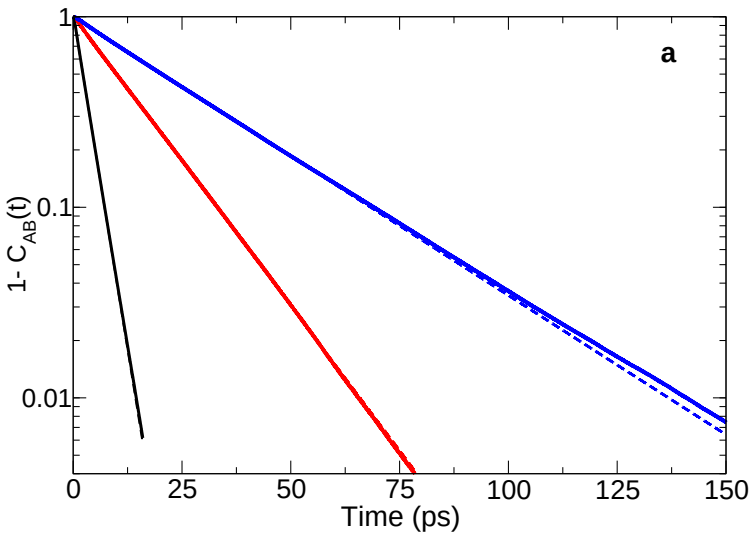

Figure 2.5: The hydrogen bond survival probability as a function of time for water (black), methanol (red), and ethanol (blue). The single-exponential fit to each function is represented by a dashed line of the same color.

ingly rare.) At a later time t, D changes its donation to B, and $\theta_{DB}(t) = 1$. The product $\theta_{DA}(0)\,\theta_{DB}(t)$ then becomes unity at time t and remains so when absorbing boundary conditions are applied. Thus, the hydrogen bond survival probability function $S_{AB}(t) = 1 - C_{AB}(t)$ represents the rate constant for hydrogen bond jumps, specifically $1 - C_{AB}(t) = e^{-k_0 t} = e^{-t/\tau_0}$. The results of this calculation are presented in Figure 2.5. Single-exponential fits to these curves result in hydrogen bond jump times, τ_0, of 3.1, 14.3, and 29.7 ps for water, methanol, and ethanol, respectively. Inclusion of the angular factors evaluated at the average jump angle for each alcohol results in corresponding τ_2^{jump} times of 3.2, 14.5, and 31.7 ps.

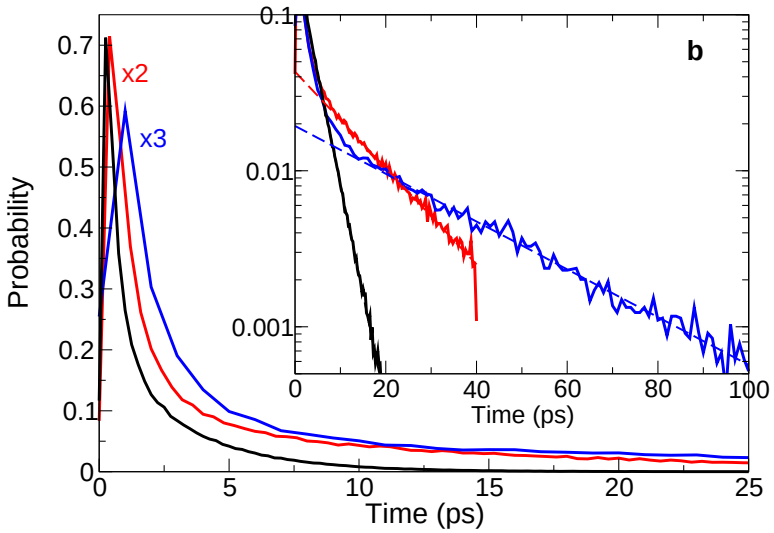

Figure 2.6: The waiting time distribution for hydrogen bond switching as a function of time for water (black), methanol (red), and ethanol (blue). The inset comprises single-exponential fits (dashed lines) to the long-time component of each distribution (solid lines).

A simple check of these results can be obtained using the hydrogen bond waiting time distributions, *i.e.*, the distribution of times a molecule must wait to switch from its current acceptor to a new acceptor. The tail of such a distribution should also represent the time for hydrogen bond switching, *i.e.*, decay as e^{-t/τ_0}. For water and each lower alcohol, the waiting time distributions are shown in Figure 2.6, with single-exponential fits to the long-time component shown in the figure inset. Similarly to the hydrogen bond survival probability distribution, the tails of the waiting time distribution are well-fit by a single-exponential function, and thus capture the dynamics of the rate process of hydrogen bond switching.

Correlation times calculated from the waiting time distributions are 3.2, 14.5, and 31.7 ps for water, methanol, and ethanol; the agreement with the hydrogen bond survival probability is excellent. The results are collected in Table 2.3.

Table 2.3: Jump time contributions (in ps) for lower alcohols

species	τ_2	$\tau_{0,SSP}{}^a$	$\tau_{2,SSP}^{jump}$	$\tau_{0,WTD}{}^b$	$\tau_{2,WTD}^{jump}$	$\tau_{2,f(\langle\Delta\theta\rangle)}^{jump}{}^c$	$\tau_{2,\langle f\rangle}^{jump}{}^d$
H_2O	2.6	3.1	3.2	3.1	3.2	—	—
MeOH	5.5	14.3	14.5	14.1	14.3	17.3	21.7
EtOH	12.1	29.7	31.7	28.4	30.3	23.6	28.9

[a] Calculated from the stable-states picture (SSP) correlation function, $1 - C_{AB}(t)$, corresponding to Figure 2.5.
[b] Calculated from the waiting time distribution (WTD) long-time decay, corresponding to Figure 2.6.
[c] Estimated using excluded volume fraction at the average jump angle, $f(\langle\Delta\theta\rangle)$ and Equation 2.8. (See Section 2.4.2.)
[d] Estimated using average excluded volume fraction, $\langle f\rangle$, and 2.8. (See Section 2.4.2.)

Both the hydrogen bond survival probability and the waiting time distributions show that τ_0 increases with increasing alkyl chain length. This implies that the increase in τ_2^{jump} is at least partly responsible for the mirrored trend in τ_2. This does not, however, address the fundamental cause of the change in the jump time, τ_0. Both enthalpic and entropic factors may change the hydrogen bond jump time, and each possibility has been investigated.

2.4.1 Enthalpy and Hydrogen Bond Jump Times

If the slowdown in jump times for increasing alkyl chain length is due to changes in the hydrogen bond enthalpy, it should manifest as changes in the activation energy

for hydrogen bond switching. For water, methanol, and ethanol, simulations were performed for a range of temperatures, and simulations details can be found in Section 2.1. From the Arrhenius equation,

$$k_2 = \frac{1}{\tau_2} = Ae^{-E_a/RT}, \tag{2.13}$$

one can determine the activation energies. Taking the natural logarithm of each side of Equation 2.13, one obtains

$$\ln\left(\frac{1}{\tau_2}\right) = \left(\frac{-E_a}{RT}\right) + \ln A,$$

which is in slope-intercept form. Thus, the activation energy is obtained from the slope of the line on an Arrhenius plot, $-E_a/R$. The results are presented in Figure 2.7. The calculated activation energies, E_a, for water, methanol, and ethanol are 3.50 ± 0.07, 3.10 ± 0.09, and 3.73 ± 0.59 kcal mol^{-1}, respectively. The activation energies for water and ethanol are the same within error bars. The value for methanol is close to these values; the difference in the methanol value is too small to account fully for the change in reorientation time. Additionally, the decrease and subsequent rise in activation energy for water to methanol to ethanol does not follow the trend of strictly increasing reorientation time. Thus, the change in reorientation time in the series of liquids cannot be enthalpic in nature.

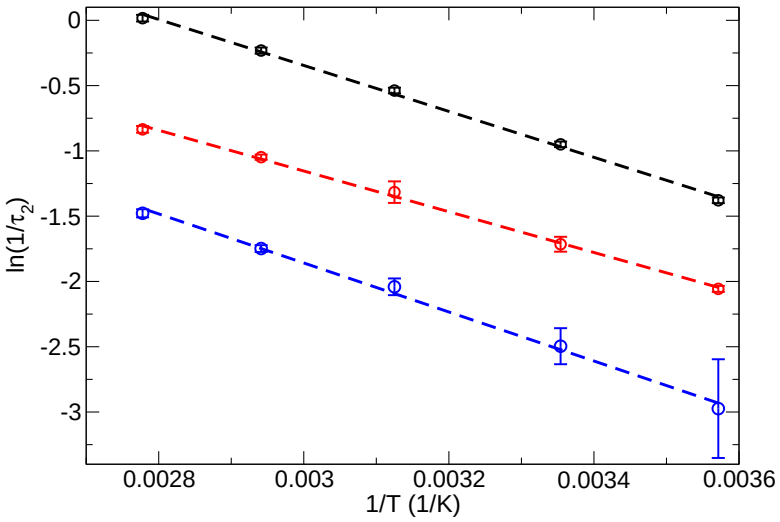

Figure 2.7: The Arrhenius plot of $k_2 = 1/\tau_2$ for water (black), methanol (red), and ethanol (blue). The dashed lines are linear fits to the data.

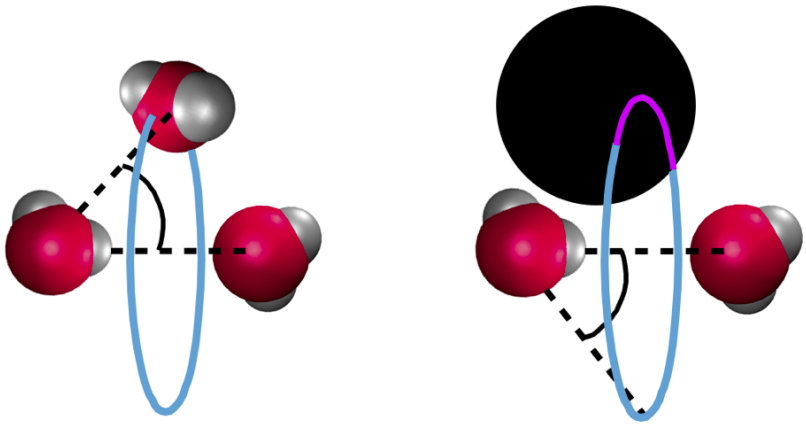

Figure 2.8: Left: A potential new acceptor molecule is positioned on a ring of equally plausible transition state geometries, shown as a blue ring. Right: The donor molecule is now near a hydrophobic solute (black), and much of the ring of transition states is inaccessible (purple) to incoming hydrogen bond exchange partners.

2.4.2 Entropy and Hydrogen Bond Jump Times

Hydrogen bond jumps occur in a symmetric fashion, with the outgoing oxygen (O_A) and the incoming oxygen (O_B) equidistant to the donor oxygen (O_D). That is, $R_{O_D-O_A} = R_{O_D-O_B} = R^{\ddagger} = 3.5$ Å. Additionally, the transition state angle is $\Delta\theta^{\ddagger}_{O_B-O_D-O_A} \approx 68^{\circ}$, with the donor hydrogen H_D bisecting this angle. The distance and angle together imply that the incoming exchange partner (molecule B) approaches the donor D anywhere on a ring, as shown in Figure 2.8, left. The ring comprises all equivalent transition states.

With a well-defined transition state geometry, it was possible for Laage *et al.*[130] to explain the reorientation of water next to hydrophobic solutes. The central idea was that a hydrophobic solute blocks molecules B from attaining the

transition-state geometry that induces the reorientation of D from hydrogen bonding with A to hydrogen bonding with B. That is, a smaller fraction of hydrogen bond exchanges occur next to the hydrophobic solute. This picture can be quantified by considering the $D-A$ hydrogen bond. For a hydrogen bond switch to occur, a molecule B must be present at the transition-state length and angle. Accordingly, these geometric parameters can be used to construct the ring of points where a molecule B would need to be located. In other words, a ring of possible transition states is constructed. Then the fraction of points on the ring that fall within the van der Waals radius of a hydrophobic group are considered excluded. The ratio of excluded points to all the points on the ring is the excluded volume fraction, f. This is shown schematically in Figure 2.8, right. The excluded volume fraction, f, can then be related to the jump time, τ_0, through Equation 2.14,

$$\frac{\tau_2^{jump}(H_2O/\text{solute})}{\tau_2^{jump}(H_2O/\text{bulk})} = \frac{1}{1-f}. \tag{2.14}$$

The quantitative agreement between the excluded volume fraction and the relative jump time for water molecules near a hydrophobic solute was found by Laage, *et al*. to be excellent.

One can adapt this excluded volume picture to the reorientation of alcohols—and calculate f from the simulation trajectory—by assuming the hydrophobic alkyl groups of the alcohols play the same role as the hydrophobic solute in the water study of Laage *et al*. In the case of alcohols, the excluded volume fraction is anticipated to be high, as each alcohol molecule has a hydrophobic

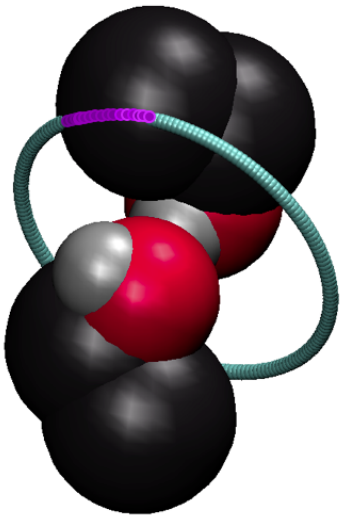

Figure 2.9: Two ethanol molecules are engaged in a hydrogen bond. Hydrogen (silver), oxygen (red), and united-atom carbon groups (black) are shown. A ring (cyan) of possible transition states is constructed based on the $\underline{R}_{O_D-O_A}$ axis, the average jump angle of $\approx 70^\circ$, and an assumed transition state distance of $R^\ddagger = 3.5$ Å. The distance from the methyl site to each site on the ring is calculated. If the distance is less than the first non-zero value in the calculated $g(R_{O-CH_3})$ function, the point on the ring is considered excluded (highlighted in purple).

group. Indeed, by replacing (H_2O/solute) with (ROH) in Equation 2.14, one can calculate anticipated excluded volume fractions for methanol and ethanol using their calculated jump time contributions. This yields $f_{\text{MeOH}} = 0.78$ and $f_{\text{EtOH}} = 0.89$.

The excluded volume fraction, f, can be calculated directly from the simulation, as shown in Figure 2.9, similarly to the calculations performed by Laage *et al*. The details of the calculation are presented in Appendix A. The results are $f(\langle\Delta\theta\rangle)_{\text{MeOH}} = 0.855 \pm 0.005$ and $f(\langle\Delta\theta\rangle)_{\text{EtOH}} = 0.895 \pm 0.005$.

While the anticipated and calculated excluded volume fraction values for ethanol are in good agreement, the values for methanol—0.78 and 0.85—are slightly different from one another. The reciprocal relationship between the slowdown factor and the excluded volume fraction means that as f approaches 1, the slowdown factor approaches infinity. Accordingly, while the predicted and calculated f values for methanol are close to one another, the difference translates to slowdown factors of $\approx$ 4.5-6.7. The $\approx$ 10% difference in f results in a 50% error in the slowdown factor. In this case, the slowdown factors are within a factor of two of one another and are in reasonable agreement, given the geometric approximations involved. However, because of the large amplification of uncertainty in the slowdown factor, comparison among values is more reasonably made using the excluded volume fraction. f. Despite the small differences between f_{MeOH} and $f(\langle\Delta\theta\rangle)_{\mathrm{MeOH}}$ from estimates based on τ_2 and direct calculation from the simulation, respectively, the overall trend across the water/methanol/ethanol series is preserved in both the estimated and calculated cases.

The jump mechanism occurs over a distribution of angles, as shown in Figure 2.4. A more accurate measure of f might be obtained by calculating f at each angle and then averaging over the angular distribution, as

$$\langle f\rangle = \int_0^{\pi} f(\Delta\theta)\,P(\Delta\theta)\,\sin(\Delta\theta)\,\mathrm{d}\Delta\theta. \tag{2.15}$$

Such a calculation is depicted in Figure 2.10, in which the transition state jump angle $\Delta\theta^{\ddagger}_{O_B-O_D-O_A}$ is varied in 15° increments. For the actual calculations, $\Delta\theta^{\ddagger}_{O_B-O_D-O_A}$

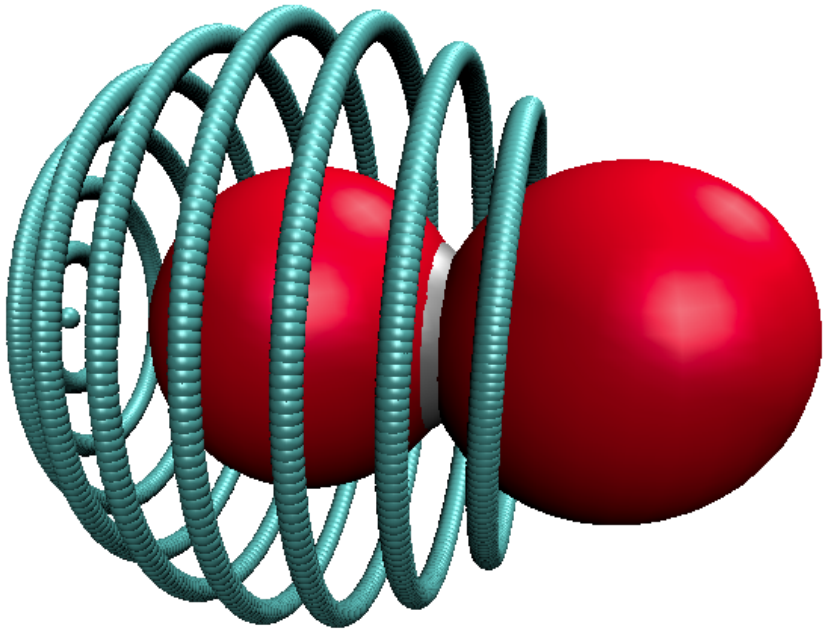

Figure 2.10: The transition state angle, $\Delta\theta^{\ddagger}_{O_B-O_D-O_A}$, can be varied to examine the dependence of the excluded volume fraction, f, on it. A hydroxyl group (oxygen, red; hydrogen, silver) is shown donating a hydrogen bond to an acceptor oxygen. The ring of possible transition states are shown in cyan, and each ring is staggered by 15° from 0° to 180°. Notably, the acceptor oxygen precludes transition states at low angles.

was varied by at most 5°. Each ring represents a separate calculation over many configurations and all molecules. Notably, $\langle f \rangle$ values obtained this way are still approximate, as they do not reflect possible changes in the distance coordinate, $R^{\ddagger}_{O_D-O_B}$, which is held fixed at 3.5 Å. Consideration of the jump angle distribution leads to $\langle f \rangle_{\mathrm{MeOH}} = 0.88$ and $\langle f \rangle_{\mathrm{EtOH}} = 0.91$. These are slightly larger than the $f(\langle \Delta\theta \rangle)$ values calculated using the average jump angle, $\langle \Delta\theta \rangle$.

The slowing of hydrogen bond jumps for ethanol is thus well-explained by the excluded volume effect. For methanol, however, the excluded volume effect still predicts that the jump contribution to reorientation is ~ 8 times slower than for water reorientation. As previously noted in Figure 2.7, the activation energy for methanol hydrogen bond jumps is slightly less than that for water and ethanol. A decrease in this enthalpic contribution corresponds to an increase in the hydrogen bond switching rate constant, and thus a faster (lower) jump time contribution, τ_2^{jump}. This effect may partially compensate for the jump time contribution over-estimated by the excluded volume. Despite such details, the overall trend across the series is maintained. Data concerning the excluded volume fractions and their effects on reorientation times are provided in Tables 2.4 and 2.3, respectively.

Table 2.4: Excluded volume fractions by various estimates

	$f^a_{\tau_2}$	$f(\langle\Delta\theta\rangle)^b$	$\langle f\rangle^c$
MeOH	0.78	0.85	0.88
EtOH	0.89	0.89	0.91

[a] Estimated using Equation 2.14 and calculated τ_2 values.
[b] Calculated from simulation by constructing a transition state ring at the angle $\langle\Delta\theta\rangle$
[c] Calculated over a distribution of angles according to Equation 2.15

The calculation of the excluded volume fraction f as a function of angle can be decomposed to provide insight to the roles different molecules and atoms play in the access the donor molecule has to new hydrogen bond acceptors, and thus the hydrogen bond jump time. Figure 2.11 shows the excluded volume decomposition for methanol. The total excluded volume fraction (black, solid line) shows that

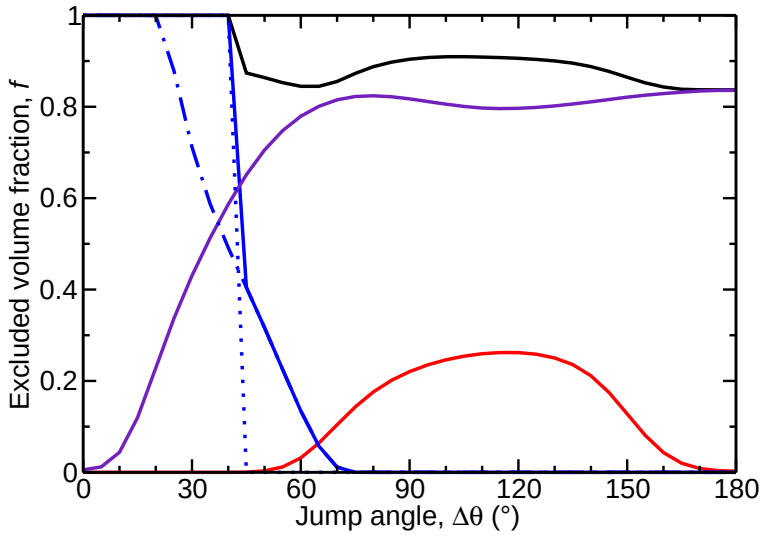

Figure 2.11: The figure shows the excluded volume fraction, f, as a function of jump angle, $\Delta\theta$ for methanol. Calculations are performed in increments of 5°. The solid black line represents the total excluded volume. Molecule types have been partitioned into hydrogen bond acceptor (blue), hydrogen bond donor (red), and all other molecules (purple). The dotted and dot-dashed blue lines represent the volume excluded by acceptor oxygen atoms and methyl groups, respectively. Uncertainties are approximately the size of the line thickness.

at small angles ($< 40^\circ$), no transition state is possible, as $f = 1$. At angles larger than 40°, the excluded volume profile decreases to about 0.8, with a broad peak of $f \approx 0.9$ from 65° to 160°.

Decomposition by molecule and atom type readily explains these features. Examining the acceptor molecule (blue, solid line), it becomes clear that no transition state is possible below 40° because such transitions are fully blocked by the acceptor oxygen atom (blue, dotted line) and to a lesser extent, the acceptor methyl group. Also, some transition states from 40° to 60° are blocked also by the acceptor methyl group for certain donor/acceptor configurations. At larger transition angles, the donor molecule itself can exclude possible transition states. The red solid line of Figure 2.11 is the donor methyl profile. (The donor oxygen, by definition, cannot contribute to the excluded volume for its own hydrogen bond switching.) This is mostly responsible for the distribution of larger excluded volume fractions at large angles. Lastly, the majority of the excluded volume comes from the methyl groups of "other" molecules (purple, solid lines)–molecules that are neither the donor nor the acceptor. (The methyl and full contributions from other molecules are the same. The oxygen atoms of other molecules are considered possible new acceptors, and they do not contribute to the excluded volume.) This can be anticipated from the fact that around the two molecules, D and A, participating in a hydrogen bond should be a large collection of surrounding molecules.

The ethanol excluded volume fraction as a function of angle shown in Figure 2.12 is qualitatively similar to the methanol case, with additional contributions

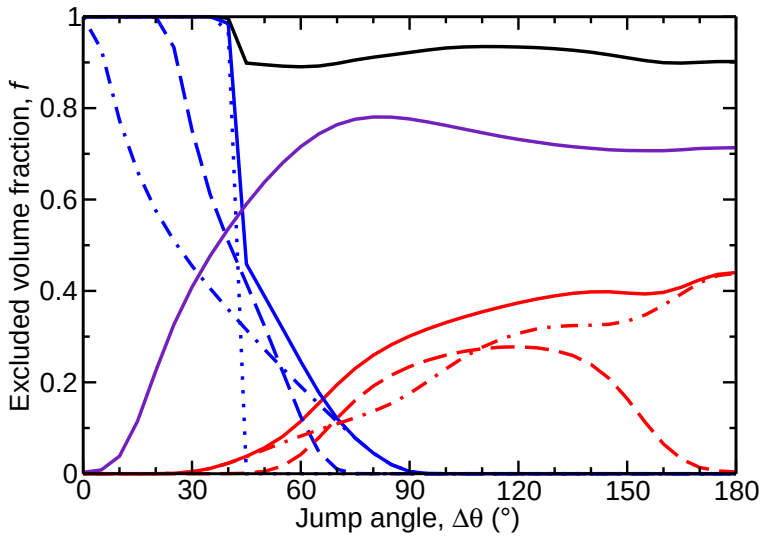

Figure 2.12: Same as for Figure 2.11 but for ethanol. Dotted lines, dashed lines, and dot-dashed lines represent the excluded volume fractions from oxygen atoms, methylene groups, and methyl groups, respectively. Uncertainties are approximately the size of the line thickness.

from the extended alkyl chain. The profile of the full excluded volume fraction indicates that all transitions at low angle are excluded by the acceptor oxygen, as in the case for methanol. The excluded volume fraction profile at transition-state angles greater than 40° is closer to 0.90. There is also a broad peak in the profile at higher angles, and it is less pronounced than it is in the case of methanol, presumably due to the higher overall value of f at large angles for ethanol relative to methanol. The roles of ethanol acceptor, donor and other molecules readily explain these differences. Specifically, Figure 2.12 shows that the acceptor oxygen (blue, dotted line), acceptor methylene group (blue, dashed line), and acceptor

methyl group (blue, dot-dashed line) can all prevent incoming acceptor molecules at small jump angles, in order of decreasing effectiveness. At larger jump angles, these curves indicate that the methylene group blocks incoming acceptors to about 70°, while the terminal methyl group can block incoming acceptor molecules up to $\approx 90^\circ$. This is easily interpreted as a consequence of connectivity, distance, and possible molecular conformations. The net result is that the ethanol acceptor molecules can block incoming acceptors at larger angles than in the methanol case. For similar reasons, the ethanol donor molecule methylene group (red, dot-dashed line) plays a similar role as the methanol donor methyl group, as they occupy the same alpha position with respect to the oxygen. The ethanol donor methyl group (red, dot-dashed line) can block possible acceptors at lower and higher angles. The net result (red, solid line) is that the donor molecule excludes transition states at higher angles more effectively for ethanol than for methanol. Notably, this is in excellent agreement with the jump angle distributions of Figure 2.4. It can be reasoned that the decreased probability in the distribution at large jump angles is, at least in part, due to the increased space occupied by the donor molecule itself at those angles. Lastly, the contribution to f from other molecules is qualitatively similar between ethanol and methanol. However, relative to methanol, the effect from other molecules is diminished in ethanol at angles where donor and acceptor molecules become more effective at blocking incoming molecules, which is directly attributable to the longer alkyl chain.

An important feature of these decompositions is that the components are non-additive. In ethanol, for example, $f^{full}(\Delta\theta) \neq f^{donor}(\Delta\theta) + f^{other}(\Delta\theta)$ and

$f_{mol}^{donor}(\Delta\theta) \neq f_{CH_2}^{donor}(\Delta\theta) + f_{CH_3}^{donor}(\Delta\theta)$. Such inequalities can be anticipated from the fact that the soft potentials of Equation 2.3 and the bond lengths and σ values in Table 2.1 allow more than one site to simultaneously block a potential acceptor. In contrast, the roles some sites play are certain and are a function of their position in the molecule, as depicted in Figure 2.13. From Figure 2.13, it can

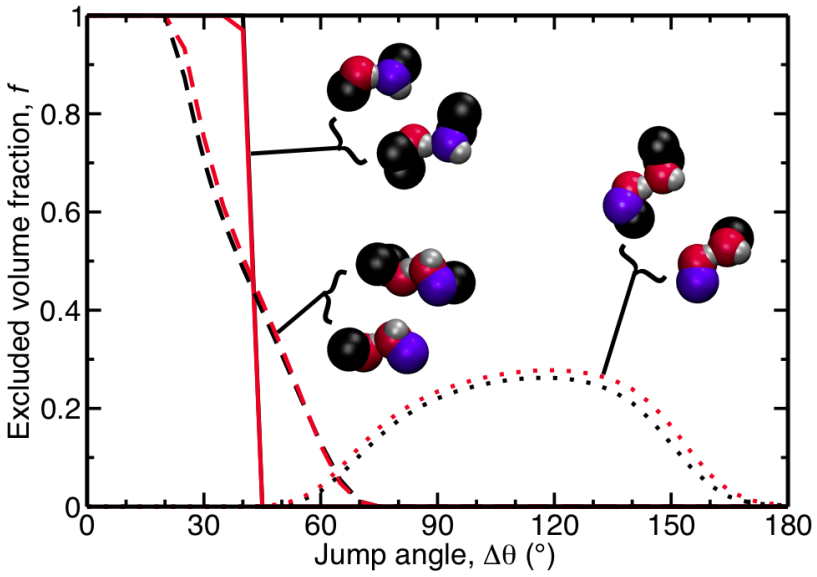

Figure 2.13: Excluded volume as a function of angle, $f(\Delta\theta)$, is shown for methanol (black lines) and ethanol (red lines) for the acceptor oxygen (solid lines), acceptor α position (dashed lines), and donor α position (dotted lines). In each case the curves for a given site are identical or nearly identical for the two alcohols. For reference, the site of interest in each case is highlighted in purple for both methanol and ethanol.

be anticipated that the acceptor oxygen in *any* alcohol should preclude incoming exchange partners at angles $< 40^{\circ}$. Similarly, the α position for both donor and acceptor molecules in any alcohol molecule should block transition states at the

same angles. The tantalizing possibility of developing a predictive model for alcohol reorientation would require knowledge of how different excluded volume effects add. The two lower alcohols presented here do not constitute a series large enough to develop such a model. In part, this motivates the study of dynamics of higher alcohols found in Chaper 3. Nevertheless, they provide the starting point for such a predictive approach.

These results provide a mechanistic picture for the slowdown in jump contribution reorientation timescales in the series water, methanol, ethanol. The increased steric bulk of the alkyl groups prevents incoming molecules from inducing a hydrogen bond switch–an important part of overall hydroxyl reorientation. The other component of reorientation—the frame reorientation of intact hydrogen bonds—is now examined.

2.5 Lower Alcohol Frame Times

The time for reorientation of intact hydrogen bonds—the frame time, τ_2^{frame}—also contributes to the overall hydroxyl reorientation time τ_2, as indicated in Equation 2.8. A $C_2(t)$ reorientational correlation function can be calculated for intact hydrogen bonds tumbling in solution. The "frame" in which the intact hydroxyl reorients is the relative $O_D - O_A$ motion, as depicted in Figure 1.3. To calculate the correlation function, at a given time $t = 0$, a hydrogen bond is identified. The reorientation of the normalized $\underline{e}_{O_D-O_A}$ vector is then monitored as a function of time, as described in Chapter 1, until the hydrogen bond breaks for the

donor to switch acceptors. Because of the distribution of hydrogen bond lifetimes, there are a greater number of contributors to the correlation function at short times than at long times. Accordingly, each bin in time is independently normalized. The independent normalization together with the low number of long-lived hydrogen bonds means that the curves fail to become smooth at long times. The results of this calculation are presented in Figure 2.14. Exponential fits to the smooth parts of

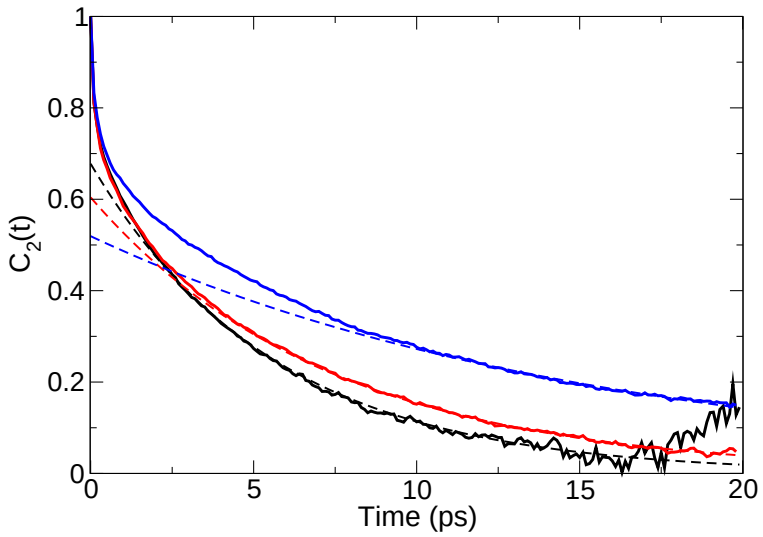

Figure 2.14: The $C_2^{frame}(t) = \langle P_2[\underline{e}_{OO}(0) \cdot \underline{e}_{OO}(t)] \rangle$ correlation functions for reorientation of intact hydrogen bonds are shown for water (black), methanol (red), and ethanol (blue) Dashed lines represent fits to the curves over the ranges 5 to 20 ps for water and 10 to 20 ps for methanol and ethanol.

the long-time tails can then be used as an estimate for the frame time contribution, and the differences in decay behavior suggest that fits be performed from 5 to 20 ps for water and from 10 to 20 ps for the alcohols. Estimates obtained this way

($\tau_{2,calc}^{frame}$) are 5.6, 7.3, and 15.5 ps for water, methanol, and ethanol, respectively. Using these values for $\tau_{2,calc}^{frame}$ and jump time contributions also calculated from correlation functions ($\tau_{2,SSP}^{jump}$ in Table 2.3) in Equation 2.8 results in values for the overall τ_2 of 2.0, 4.9, and 10.4 ps for water, methanol, and ethanol, respectively. Notably, these values for τ_2 are in very good agreement with those calculated from the full correlation function, $C_2(t)$, in Figure 2.3 and are 2.6 ± 0.1, 5.5 ± 0.3, and 12.1 ± 1.7 ps.

The frame times for water, methanol, and ethanol also have been calculated using Equation 2.8 and the values of τ_2^{jump} calculated by various methods. These estimates for τ_2^{frame} are compared in Table 2.5. For each value of τ_2^{frame}, the overall reorientation timescale, τ_2, was used in the calculation, as in Equation 2.8, and τ_2 is therefore is provided in Table 2.5 as a reference. The frame time calculated using Equation 2.8 and the calculated value of τ_2^{jump} is $\tau_{2,calc}^{frame}$.

Table 2.5: Frame times (in ps) for lower alcohols

species	τ_2	$\tau_{2,calc}^{frame}$	$\tau_{2,SSP}^{frame\ a}$	$\tau_{2,WTD}^{frame\ b}$	$\tau_{2,f(\langle\Delta\theta\rangle)}^{frame\ c}$	$\tau_{2,\langle f\rangle}^{frame\ d}$
H_2O	2.6	5.6	13.9	13.9	—	—
MeOH	5.5	7.3	8.7	8.9	8.1	7.4
EtOH	12.1	15.5	19.7	20.1	24.8	20.8

[a] Calculated using Equation 2.8 and τ_2^{jump} value derived from the stable-states picture in Figure 2.5
[b] Calculated using Equation 2.8 and τ_2^{jump} value derived from the waiting time distribution in Figure 2.6
[c] Calculated using Equation 2.8 and the τ_2^{jump} value derived from Equation 2.14 and f calculated using the average jump angle from Equation 2.10.
[d] Calculated using Equation 2.8 and the τ_2^{jump} value derived from Equation 2.14 and $\langle f\rangle$ calculated from Equation 2.15.

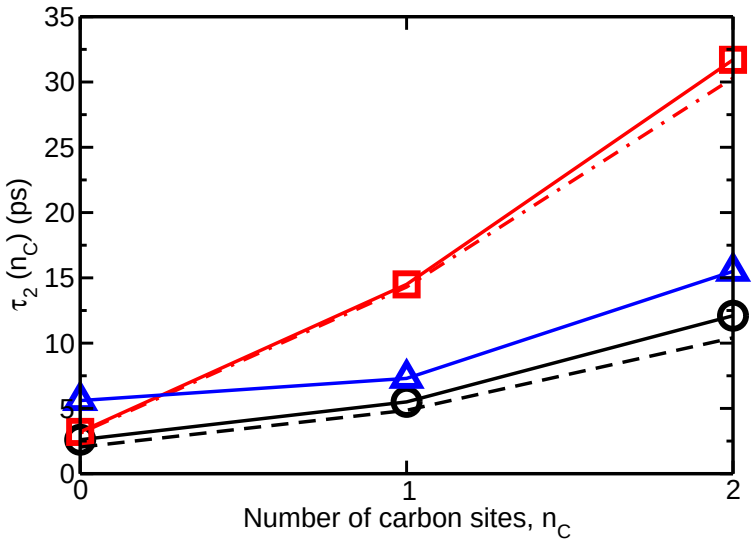

Figure 2.15: The jump time contribution (τ_2^{jump}, red) and frame time contribution (τ_2^{frame}, blue) to the longest reorientation timescale (τ_2, black) are a function of the number of carbon units in the molecule. For both jump time and frame time contributions, time constants derived using the stable states picture of Figure 2.5 (solid line) and the waiting time distribution of Figure 2.6 and Equation 2.8 are shown. For the frame time contribution, the results from the direct calculation of the τ_2^{frame} correlation function are also provided (dot-dashed line.)

Interestingly, mechanistic differences appear when the jump time contributions of Table 2.3 and the frame time contributions of Table 2.5 are compared. A visual comparison is provided in Figure 2.15. For water, $\tau_2^{frame} > \tau_2^{jump}$, which indicates that reorientation proceeds dominantly *via* mechanisms involving hydrogen bond exchange. (That is, in Figure 2.15, for $n_C = 0$, values corresponding to points in blue are larger than those in red.) In methanol, $\tau_2^{frame} < \tau_2^{jump}$, which suggests that tumbling of intact hydrogen bonds becomes the dominant pathway for

reorientation. The ethanol case is similar to methanol. More quantitatively, for methanol $\tau_{2,SSP}^{jump}/\tau_{2,SSP}^{frame} \approx 1.67$ while for ethanol, $\tau_{2,SSP}^{jump}/\tau_{2,SSP}^{frame} \approx 1.60$. As $\tau_{2,SSP}^{jump}$ and $\tau_{2,SSP}^{frame}$ are related through Equation 2.8, it may be more instructive to make comparisons using the independently calculated frame time contribution, $\tau_{2,calc}^{frame}$. Doing so yields $\tau_{2,SSP}^{jump}/\tau_{2,calc}^{frame} \approx 1.99$ for methanol and $\tau_{2,SSP}^{jump}/\tau_{2,calc}^{frame} \approx 2.04$ for ethanol. These results indicate that for both methanol and ethanol, the jump time contribution is generally between 1.5 and 2 times longer‘ than the frame time contribution, and reorientation in both is dominated by the frame time contribution.

2.6 Lower Alcohol Reorientation Summary

In this chapter, the reorientation across the series water, methanol, ethanol was examined. The reorientation timescales lengthen with increasing number of carbon sites. Notably, for each molecule, the duration a free hydroxyl persists in solution is sub-picosecond. Thus, the Debye model, in which reorientation proceeds through low-amplitude angular diffusion between hydrogen bond events, cannot explain reorientation dynamics. The extended jump model, recently developed for water, was applied to each molecule. In the extended jump model, both large-amplitude angular jumps during switching of hydrogen bond partners as well as diffusive tumbling with intact hydrogen bond partners contribute to the reorientation. The results here indicate that both jump time contributions, τ_2^{jump}, and frame time contributions, τ_2^{frame}, to overall reorientation slow with increasing alkyl chain length. The slowing trend originates from entropic, rather than enthalpic, consid-

erations. Because the hydrogen bond exchange angle is very similar across the series, the entropic effect enters through a change in the fundamental hydrogen bond jump time. The increasing bulk of the alkyl group increasingly precludes potential new acceptor molecules from achieving or participating in a transition state geometry. That is, the increased bulk decreases the probability of hydrogen bond exchange, thereby increasing the time. Notably, for the same position along the alkyl chain and for the same transition angle, approximately the same fraction of possible transition states is blocked, leading to the notion that a predictive model for reorientation dynamics might be developed. Additionally, the change in steric bulk also has the important consequence of changing the reorientation mechanism. For water, reorientation occurs mainly through hydrogen bond exchange. For lower alcohols, tumbling of intact hydrogen bonds becomes the dominant reorientation pathway.

Two fundamental questions have been raised in this chapter. The first, raised in Section 2.4.2, is: *Can one develop a predictive model of reorientation dynamics in alcohols based on excluded volume?* The second, raised in Section 2.5, is: *To what degree is either hydrogen bond jumping or hydrogen bond tumbling dominant in hydroxyl reorientation as a function of alkyl chain length, and for what alkyl chain length, if any, does a change in mechanism occur?* At the heart of these questions is the extension of the present study to higher alcohols, which serves as the motivation of the next chapter.

Chapter 3

Reorientation in Higher Alcohols

The results of the previous Chapter show that the mechanism for alcohol reorientation is dependent on the alkyl chain length for the lower alcohols. Within the extended jump model, water reorients dominantly through hydrogen bond exchange ($\tau_2^{frame} > \tau_2^{jump}$), while reorientation in methanol and ethanol is dominated by tumbling of intact hydrogen bonds ($\tau_2^{jump} > \tau_2^{frame}$). Notably, the relative contribution from hydrogen bond exchange is diminished in ethanol compared to methanol. This suggests that the reorientation mechanism may revert to a dominant jump contribution for some alkyl chain longer than the ethyl group. The determination of such mechanistic trends clearly necessitates study of longer chain ("higher") alcohols.

Additionally, it was determined that the hydrogen bond exchange frequency is related to the volume excluded by the surrounding alkyl groups. For a given hydrogen bond exchange angle, the excluded volume associated with specific positions within the alkyl chain (relative to the hydroxyl group) is constant. For

example, the same volume is excluded by the α-carbon group of the hydrogen bond donor, regardless of the length of the identity of the alcohol. However, for a given exchange angle, the way in which the excluded volume contributions from different positions along the chains of various molecules (donor, acceptor, other) add is unclear. Empirical relationships may be derived, but their determination requires studying higher alcohols.

In addition to the interest in fundamental chemistry, higher alcohols are key solvents and commodity chemicals. As such, they also enjoy wide use as flavor and fragrance agents, general reaction media, alkylating agents, extraction solvents. Understanding general principles behind reorientation dynamics across a range of alcohols therefore facilitates rational design in manufacturing products ranging from pesticides to pharmaceuticals. The trends in reorientation across higher alcohols and the origins of these trends are the subject of the present Chapter.

3.1 Simulation Details for Higher Alcohols

To examine trends in alcohol reorientation dynamics with greater clarity, the study of reorientation in lower alcohols (methanol and ethanol) was extended to *n*-alcohols through hexanol. All alcohols in the series were modeled using the OPLS-UA force field [121,122] modified to include flexibility (bond stretching and bending as well as torsional motion) [131]. Because of the force-field modification, methanol and ethanol were re-examined; this allows for comparison among force fields and also increases reliability in examining trends across the alcohols. The

force field parameters are provided in Table 3.1. Each alcohol molecule was

Table 3.1: Force field parameters for higher alcohols

Atom	m (g mol^{-1})	q (e)	σ (Å)	ε (kcal mol^{-1})
H	1.00790	0.435	0.00000	0.00000
O	16.00000	-0.700	3.07000	0.17000
C_{CH_2}	14.03000	†	3.90500	0.11800
C_{CH_3}	15.04000	†	3.90500	0.20700
Atoms AB	$R_{eq,AB}$	k_{AB} (kcal mol^{-1})		
HO	0.94500	553.00		
OC	1.43000	386.00		
CC	1.53000	260.00		
Atoms ABC	$\theta_{eq,ABC}$ ($^\circ$)	k_θ (kcal mol^{-1})		
HOC	108.5	55.00		
OCC	109.5	80.00		
CCC	112.4	63.0		
Atoms ABCD	$V_0^{\ddagger}$	V_1	V_2	V_3
HOCC	0.000	0.834	-0.116	0.747
OCCC	0.000	0.702	-0.212	3.060
CCCC	0.000	1.522	-0.315	3.207

† The charge on a united atom carbon unit is +0.265 e if occupies the α position and is 0 otherwise.
‡ Units for all torsional parameters are kcal mol^{-1}.

constructed in Molden [132] using equilibrium bond lengths and angles as well as torsional minima. The center of mass of the molecule was placed at each of the 4 sites of a face-centered cubic lattice. The dimensions of the lattice were chosen to reproduce the experimental density of the liquid alcohol near 298 K. Each of the four molecules was then rotated into a unique orientation to prevent a large dipole moment in the resulting initial configuration for the system. The group of 4 molecules was then replicated 4 times along each Cartesian x, y, and z axis to form

the initial system configuration comprising 256 molecules. Alcohol molar masses, densities, and simulation box lengths are provided in Table 3.2.

Table 3.2: Simulation box details for higher alcohols

Molecule	M (g mol^{-1})	ρ (g cm^{-3}) †	L_{box} (Å)
MeOH	32.0423	0.7914	25.90
EtOH	46.0688	0.7893	29.25
n-PrOH	60.0953	0.7997	31.70
n-BuOH	74.1218	0.8095	33.95
n-PnOH	88.1483	0.8144	35.85
n-HaOH	102.1748	0.8136	37.70

† Density values are taken from [133] at a temperature of 293 K for alcohols except *n*-propanol, which was measured at 298 K.

Classical MD simulations were run using the LAMMPS software package [134]. For each alcohol, an initial 1 ps trajectory was run in the *NVE* ensemble to relax the initial structure. Then, a 1 ns equilibration phase preceded a 40 ns trajectory (2 fs time step) run in the *NVT* ensemble at 298 K using a Nosé-Hoover thermostat with a 0.1 ps time constant. A second trajectory was initiated from the final configuration of the first by first running 250 ps in the *NVE* ensemble, equilibrating for 1 ns in the *NVT* ensemble, and then running a 40 ns trajectory. Similarly, a third 40 ns trajectory was initiated from the final configuration of the second trajectory by running a 500 ps relaxation trajectory in the *NVE* ensemble, a 1 ns equilibration in the *NVT* ensemble, and a final collection stage of 40 ns in the *NVT* ensemble. The method thereby ensures that three independent 40 ns trajectories were collected, for a total trajectory time of 120 ns. Configurations in all cases were written every 200 fs.

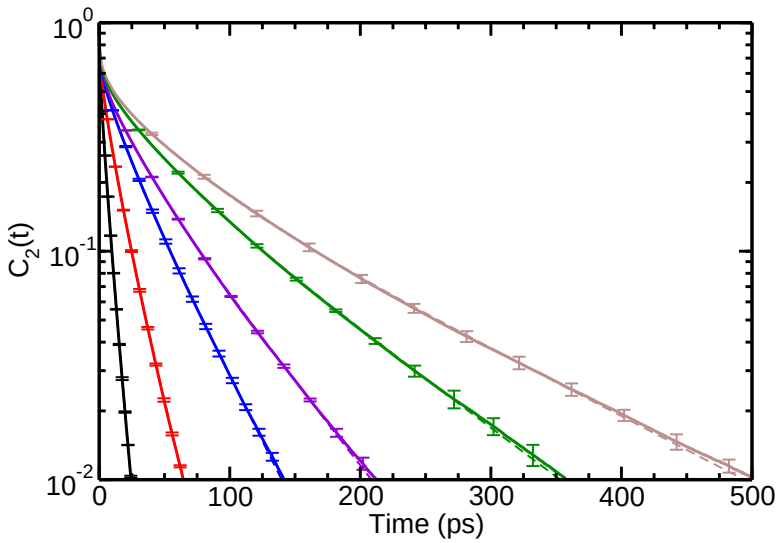

Figure 3.1: The $C_2(t)$ correlation functions for methanol (black), ethanol (red), *n*-propanol (blue), *n*-butanol (purple), *n*-pentanol (green), and *n*-hexanol (brown) are shown. Dashed lines indicate fits to the data using a sum of 4 exponential functions.

3.2 Reorientation Trends and Emergent Dynamics

3.2.1 Results for Reorientation

The $C_2(t)$ correlation functions have been calculated across this series of alcohols and are presented in Figure 3.1. In contrast to the lower alcohols, the higher alcohols require 4-exponential functions to fit $C_2(t)$ down to approximately $\approx 1\%$ of the initial magnitude. The amplitudes and timescales for each alcohol are reported in Table 3.3. The data in Table 3.3 indicate that the inertial timescales (τ_a) and amplitudes (A_a) increase only very slightly for increasing alkyl chain length.

Table 3.3: Timescales (in ps) and amplitudes in higher alcohols.

Molecule	A_a	τ_a (ps)	A_b	τ_b (ps)	A_c	τ_c (ps)	A_d	τ_d (ps)
MeOH	0.282	0.126	0.219	1.8	0.499	6.0	-	-
EtOH†	0.249	0.123	0.120	1.2	0.322	8.6	0.309	18.7
n-PrOH	0.268	0.160	0.116	1.9	0.222	14.9	0.394	38.0
n-BuOH	0.272	0.181	0.148	2.9	0.244	22.6	0.336	59.3
n-PnOH	0.284	0.213	0.153	4.5	0.242	35.0	0.321	101.8
n-HaOH	0.290	0.236	0.160	6.1	0.264	46.0	0.286	147.4

† Ethanol can be also well-fit by a 3-exponential function,
$C_2(t) = 0.36e^{-t/0.66} + 0.327e^{-t/8.3} + 0.313e^{-t/18.7}$.

(These timescales are not well resolved due to the 200 fs interval between stored configurations.) With the exception of methanol, the librational motion amplitude (A_b) also increases across the series. While the timescale generally increases with chain length, methanol is well-fit by a 3-exponential function; ethanol can also be fit this way, but a slightly better fit is obtained using 4 exponentials. However, for *n*-propanol through *n*-hexanol, the long timescale is split into 2 parts, (τ_c and τ_d). While both τ_c and τ_d increase with increasing alkyl chain length, the faster of these two (τ_c) grows in (*i.e.*, increases in amplitude) at the expense of the longer timescale. This emergent timescale, which increases in τ_d while decreasing in A_d, clearly complicates attempts at developing a predictive model for alcohol reorientation dynamics, as proposed in Chapter 2. The origin of these emergent timescales is now investigated.

Within the extended jump model, the long timescales observed in reorientational correlation functions are ascribed to contributions from the hydrogen bond exchanges and hydrogen bond tumbling. Thus, it is possible that the additional

timescales appear in either the jump time or the frame time, respectively. To address these possibilities, both the jump time and frame time contributions were calculated for each alcohol.

The jump times for the alcohol series were calculated as before (see Section 2.4 and Equation 2.12.) Curves for methanol can be fit to bi-exponential functions, while the curves for ethanol and longer-chain alcohols can be fit using a 3-exponential function. The resulting amplitudes and timescales are tabulated in Table 3.4. Note that for higher alcohols, this differs from the two-exponential fits

Table 3.4: Jump times (in ps) and amplitudes in higher alcohols.

Molecule	A_a	τ_a	A_b	τ_b	A_c	τ_c
MeOH	0.140	1.922	0.860	15.4	-	-
EtOH	0.113	2.659	0.0311	10.4	0.856	35.7
n-PrOH	0.110	2.942	0.0790	14.5	0.811	54.3
n-BuOH	0.117	3.448	0.114	21.9	0.769	70.2
n-PnOH	0.125	3.945	0.169	29.0	0.706	92.0
n-HaOH	0.134	4.312	0.225	36.2	0.641	109.2

for the jump time correlation functions in Chapter 2. (Here, the results for ethanol are nearly bi-exponential.) A bi-exponential behavior is generally expected with a fast time, τ_a, corresponding to non-barrier crossing fluctuations and the slower time giving $1/k_{jump}$ where k_{jump} is the rate constant for hydrogen bond exchange.

The frame contribution was also examined for additional dynamics. The frame time was calculated as previously discussed (see Section 2.5).The results of the frame reorientation correlation function calculation are presented in Figure 3.2. A 3-exponential function also is sufficient to fit the frame time correlation functions

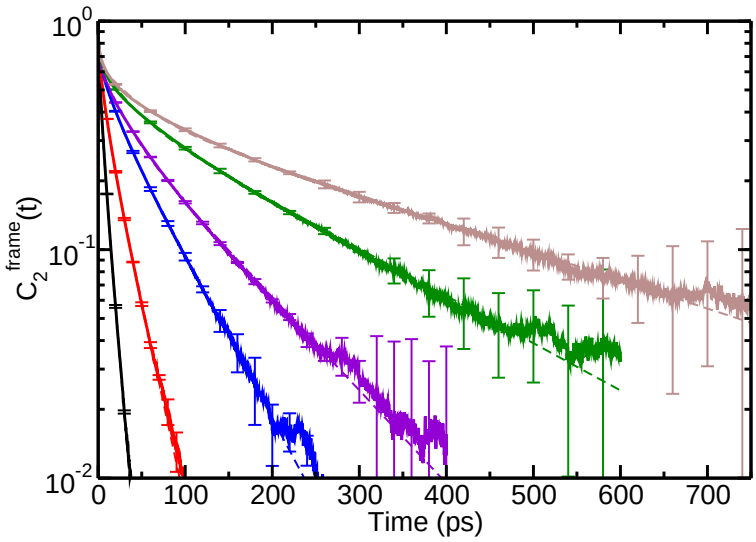

Figure 3.2: The $C_2(t)$ frame reorientation correlation functions for methanol (black), ethanol (red), *n*-propanol (blue), *n*-butanol (purple), *n*-pentanol (green), and *n*-hexanol (brown) are shown. Dashed lines indicate fits to the data using a sum of 3 exponential functions.

to about 1%, as indicated by the dahsed lines in Figure 3.2. The long time constants τ_2^{frame} increase for increasing alkyl chain length, as is clear in Table 3.5.

Table 3.5: Frame times (in ps) and amplitudes in higher alcohols.

Molecule	A_a	τ_a	A_b	τ_b	A_c	τ_c
MeOH	0.216	0.287	0.310	3.1	0.474	9.4
EtOH	0.257	0.402	0.295	7.2	0.449	24.6
n-PrOH	0.294	0.543	0.217	13.6	0.489	60.9
n-BuOH	0.334	0.880	0.263	23.6	0.403	106.7
n-PnOH	0.345	1.163	0.235	34.2	0.420	210.2
n-HaOH	0.342	1.296	0.249	41.5	0.408	349.8

Because the frame times do not show additional timescales, the additional timescales in $C_2(t)$ are reasonably attributed to the jump dynamics. In further support of this, the longest timescales in the jump dynamics decrease in amplitude with increasing alkyl chain length, the same trend observed for the longest timescales amplitudes in $C_2(t)$ (Table 3.3.) The frame time amplitudes do not show this correspondence. To investigate further the jump dynamics in higher alcohols, an analysis of local hydrogen bond relationships, free energy surfaces, and general time-dependent reaction geometries was performed.

3.2.2 Local Hydrogen Bond Relationships

Because of the central role hydrogen bonding plays in alcohol reorientation dynamics, it is possible that differences in timescales originate from differences in hydrogen bonding relationships. Of particular interest are the relationships among the donor (D), current acceptor (A), and future acceptor (B) molecules. As

an example consider the case in which A is a hydrogen bond donor to B. This implies that B is already within approximately two molecular diameters of D, and therefore may be more likely to form a hydrogen bond with D than, say, if B were unassociated with A. Such proximity also suggests that B in this case is more accessible to D, and the hydrogen bond jump may occur quickly relative to cases where B is unassociated with A. Similarly, one might anticipate that the jump angle would be small. This example illustrates the following hypothesis: The hydrogen bond relationships among molecules D, A, and B result in different geometries that have associated with them different jump time contributions to the reorientation correlation function. Because it is the contribution to the jump time that is of interest, the hydrogen bond relationships at the switching time t_0 have been examined. To simplify the classification of hydrogen bond relationships, the molecule A, the acceptor of a hydrogen bond from the OH group in question (D), has been selected as a reference. One can then imagine three hydrogen bond cases at t_0 for the relationship between molecules A and B, as depicted in Figure 3.3. In the first, labeled DBA, B and D both donate a hydrogen bond to A. In the second, labeled DAB, B accepts a hydrogen bond from A, which accepts a hydrogen bond from D. In the last, labeled $other$, A and B have no hydrogen bonding relationship. The relationships shown in Figure 3.3 have been taken directly from the simulation trajectory and provide snapshots shortly before ($t_{switch-3}$) and after ($t_{switch+3}$) the jump event $DA + B \rightarrow DB + A$ at time t_{switch}.

Each hydrogen bond switch event in the trajectory is classified as falling into one of these three cases. Then the simulation can be mined for the jump angle, $\Delta\theta$,

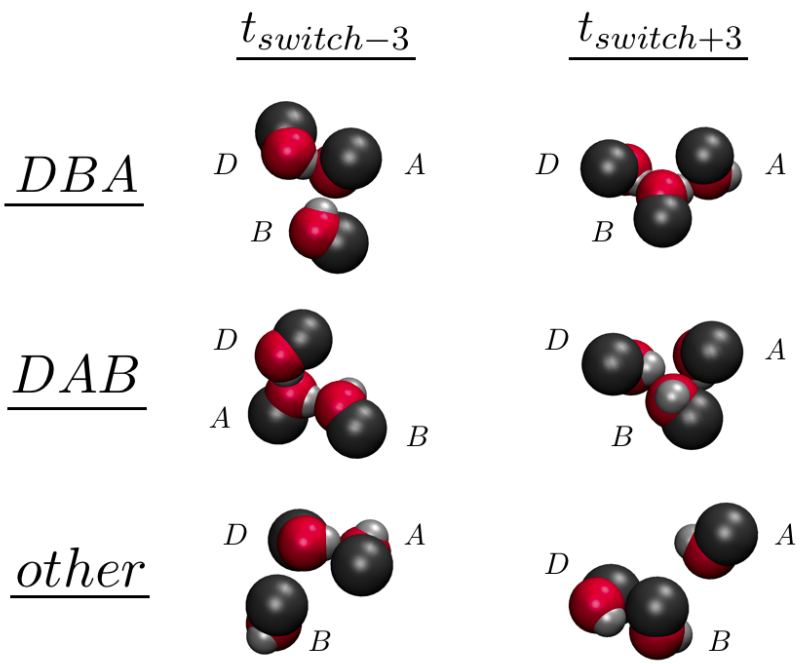

Figure 3.3: Three possible relationships exist between the current hydrogen bond acceptor molecule, *A*, and the future hydrogen bond acceptor molecule, *B* at the time of hydrogen bond switching, t_{switch}. Methanol hydrogen (silver), oxygen (red), and methyl (black) sites are shown for a hydrogen bond donor (*D*), current acceptor (*A*), and next acceptor (*B*) molecules both before ($t_{switch-3}$) and after ($t_{switch+3}$) a switch. In the first (upper left, "*DBA*") arrangement, *B* donates a hydrogen bond to *A* during the hydrogen bond switch event (at time t_{switch}). In the second ('*DAB*") arrangement, *B* accepts a hydrogen bond from *A*. In the final ("*other*") arrangement, *B* and *A* are not related through hydrogen bonding.

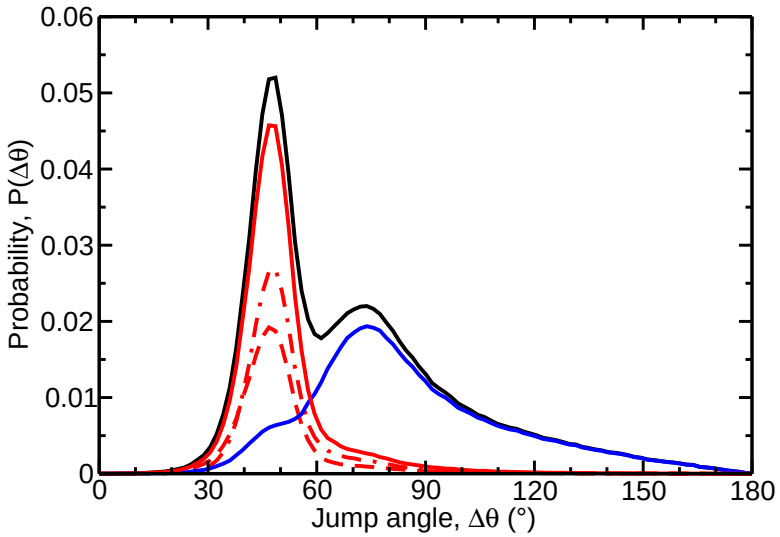

Figure 3.4: The distribution of jump angles is a function of the hydrogen bond relationships between the current (*A*) and future (*B*) acceptor. The solid black curve is the full jump angle distribution for methanol. The solid red and blue lines represents the jump angle distributions for cases in which hydrogen bond relationships do and do *not* exist, respectively, between the molecules *A* and *B*. Notably, when *A* and *B* are related through hydrogen bonding, the relationship can be further decomposed to cases where *B* donates to *A* (case "*DBA*", dashed red line) and *B* accepts from *A* (case "*DAB*", dot-dashed red line).

for each switch case. The results for methanol are presented in Figure 3.4. For nearly all hydrogen bond switches that occur at small jump angles, *A* and *B* are related through hydrogen bonding, as indicated by the solid red line. The relative magnitudes and positions of the curves for *DBA* (dashed lines) and *DAB* (dot-dashed lines) are very similar, which suggests that the nature (*i.e.*, directionality) of the relationship between *A* and *B* (*i.e.*, *DBA* or *DAB*) appears to matter little. In

contrast, for hydrogen bond switch cases in which A and B have no hydrogen bond relationship, the switches occur at large jump angles. Geometrically, this would imply that the molecule B can be regarded as "behind" D (if the hydroxyl group is regarded as pointing "forward"). Thus, for the *other* case, it is possible that B is the hydrogen bond donor to D. However, a simple analysis of hydrogen bond switches indicates that this is so for $< 1\%$ of all hydrogen bond switches, and thus the *other* case results from B having no direct association with D.

Importantly, calculations for each alcohol, methanol through *n*-hexanol, show qualitatively the same decomposition of jump angles as shown in Figure 3.4. That is, when A and B are hydrogen bonded, hydrogen bond switching of D occurs at small jump angles; when A and B are not hydrogen bonded, hydrogen bond switching of D occurs at larger jump angles. Thus, while the increased excluded volume appears to change the relative intensities of each peak in the distribution, the positions of the peaks are associated with the local hydrogen bonding structure at the time of hydrogen bond switching.

3.2.3 Alcohol Free Energy Profiles

In the extended jump model, the hydrogen bond exchanges are viewed as chemical reactions. In this context, timescales are related to free energy barriers, which in turn are relatable to the liquid structure. The first step in hydrogen bond switching in water comes from the molecule B moving from the second to the first solvation shell of the donor molecule D. A reasonable hypothesis, then, is that in alcohols,

the energetic barrier for moving from the second to first solvation shell changes as a function of alkyl chain length, thereby resulting in different timescales.

The quantity $g(R_{OO})$ (see Section 3.3.2) can be used to calculated the Helmholtz free energy, as

$$\Delta A(R_{OO}) = -k_B T \ln g(R_{OO}). \tag{3.1}$$

The results are shown in Figure 3.5. From the free energy curves $\Delta A(R_{OO})$ presented in Figure 3.5, trends related to alkyl chain length are evident. To determine if these differences are statistically meaningful, for each alcohol, the trajectory is parsed into 10 blocks. The average $\Delta A(R_{OO})$ for each block was the used to calculate uncertainties according to Student's t-test[126]. The results of calculating the free energy barriers this way as a function of alkyl chain length, n_C, are shown on the right of Figure 3.5. From Figure 3.5, it is clear that the free energy associated with moving an oxygen atom from the second to first solvation shell (black curve) decreases with increasing alkyl chain length. Also, the curve for *n*-propanol through *n*-hexanol becomes level; relative free energy values are equivalent within statistically uncertainty. The relative free energy barriers are better resolved for oxygen atoms moving from the second to third solvation shells, as indicated by the red curve of Figure 3.5, right. Excepting methanol, it becomes increasingly difficult for oxygen atoms to move from the second to third solvation shell. Taken together with the deep first shell minima in Figure 3.5, the hydroxyl groups are strongly associating, as one would anticipate for a networked liquid.

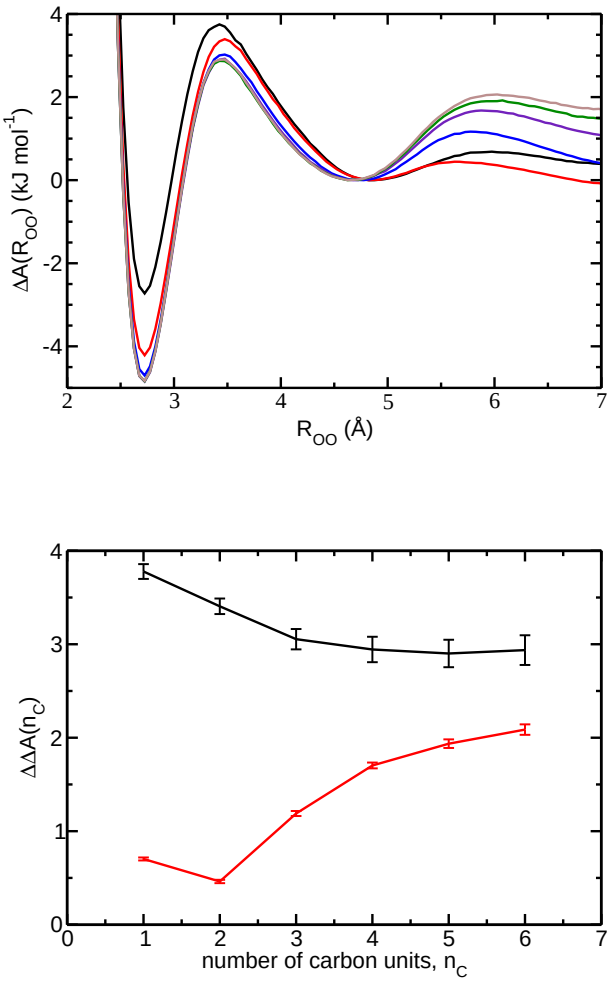

Figure 3.5: Top: Helmholtz free energies, $\Delta A(R_{OO})$ calculated from $g(R_{OO})$ are presented for methanol (black), ethanol (red), *n*-propanol (blue), *n*-butanol (purple), *n*-pentanol (green), and *n*-hexanol (brown). The curves have been shifted so that the second minimum is zero for each curve. This facilitates comparison of barrier heights in moving from the 2^{nd} to 1^{st} and 2^{nd} to 3^{rd} solvation shells across the alcohol series. Bottom: Relative barrier heights, $\Delta\Delta A(n_C)$ are a function of alkyl chain length, n_C, as shown in the figure. The free energy barrier for an oxygen atom moving from the second to first solvation shell (black) and the second to third solvation shell (red) are provided for each alcohol.

However, Figure 3.5 fails to explain the timescales observed across the series of alcohols. The thermal energy available at 298 K, $k_B T \approx 2.5$ kJ mol^{-1}, is larger than the barrier heights in moving from the second to third solvation shells, and is only slightly smaller than the barrier heights in moving from the second to first solvation shells. One can also examine the relative barrier heights and recognize that their ratios are not large enough to account for the changes in observed timescales. In the simplest analysis, a doubling in rate constant requires a relative energy difference of ≈ 1.7 kJ mol^{-1}, as per $-k_B T \ln 2 \approx \Delta\Delta A(R)$. This fails to described the observed dynamics, as $\tau_c^{n-HaOH}/\tau_c^{n-PrOH} \approx 3$ and $\tau_d^{n-HaOH}/\tau_d^{n-PrOH} \approx 3.9$. That is, the calculated free energy differences are always too small to account for the large relative changes in timescales. Also, the emergence of a new timescales τ_d requires the appearance of an alternative reaction pathway. While increased barriers are observed in $\Delta A(R_{OO})$ (*i.e.*, the $2^{nd} \rightarrow 3^{rd}$ shell barriers), their magnitudes are also too small, as $\tau_d^{n-PrOH}/\tau_c^{n-PrOH} \approx 2.6$ and $\tau_d^{n-HaOH}/\tau_c^{n-HaOH} \approx 3.2$.

3.2.4 Alcohol Free Energy Landscapes

The free energy analysis in the coordinate R_{OO} is insufficient to capture the relevant free energy barriers to hydrogen bond switching in higher alcohols. That is, the angular coordinates may be of consequence, but are averaged over in an analysis of $\Delta A(R_{OO})$ only. To this end, oxygen-oxygen pair distribution functions in the coordinates $\Delta R^{\ddagger} = R_{O_A-H_D} - R_{O_X-H_D}$ and $\cos\theta_{H_D-O_D-O_X}$, where X is any non-A/non-D atom, were constructed. The use of the cosine function means there is no Jacobian ($\sin\theta$ factor) in the angular coordinate. The resulting pair

distribution functions, $g(\Delta R, \cos\theta)$ can be similarly translated to Helmholtz free energy profiles, $\Delta A(\Delta R, \cos\theta)$, by straightforward analogy to Equation 3.1.

The results of this analysis are shown in Figures 3.6, 3.7, and 3.8, where higher free energies are bluer and lower free energies are redder. Notably, the energy scale runs from $\Delta E \approx -15$ to -30 kcal mol^{-1} in all cases. It is therefore immediately evident that the free energy changes cannot quantitatively explain the trends in the reorientation dynamics. However, Figures 3.6-3.8 show features that qualitatively agree with both the trend across the alcohol series as well as the emergence of new reorientation timescales. In the extended jump model, the transition state distance, $\Delta R^{\ddagger}$, is symmetric with respect to hydrogen bond acceptor oxygens O_A and O_B, and thus the transition state lies along the line $\Delta R^{\ddagger} = 0$ Å, and can be identified by the saddle point near $\cos\theta \approx 0.6 - 0.7$. (Notably, this is in agreement with the jump angle distribution, as the most probable jump angle is about 50°, and $\cos 50^{\circ} \approx 0.64$.) More generally, the cut through this free energy surface at $\Delta R^{\ddagger} = 0$ Å gives the ensemble of hydrogen bond exchange transition states and is consistent with the jump angle distributions. (See, for example, Figure 3.4.) For $\Delta R^{\ddagger} = 0$ Å, at $\cos\theta = 1$ (*i.e.*, $\theta = 0^{\circ}$) white spots are observed. This region is inaccessible, as it would represent an oxygen overlapping the oxygen of the current hydrogen bond acceptor. There is a free energy minimum ($\Delta R^{\ddagger} \approx 2.5$ Å and $\cos\theta \approx 0.8$ or $\theta \approx 40^{\circ}$), which grows deeper with increasing alkyl chain length and represents the global minimum. Also at low angles (near $\cos\theta = 0.9$ or $\theta \approx 25^{\circ}$) but at large distances, a *new* free energy minimum grows in with lengthening alkyl chain. A similar trend can be observed for larger angles ($\cos\theta \approx -0.75 - 0$

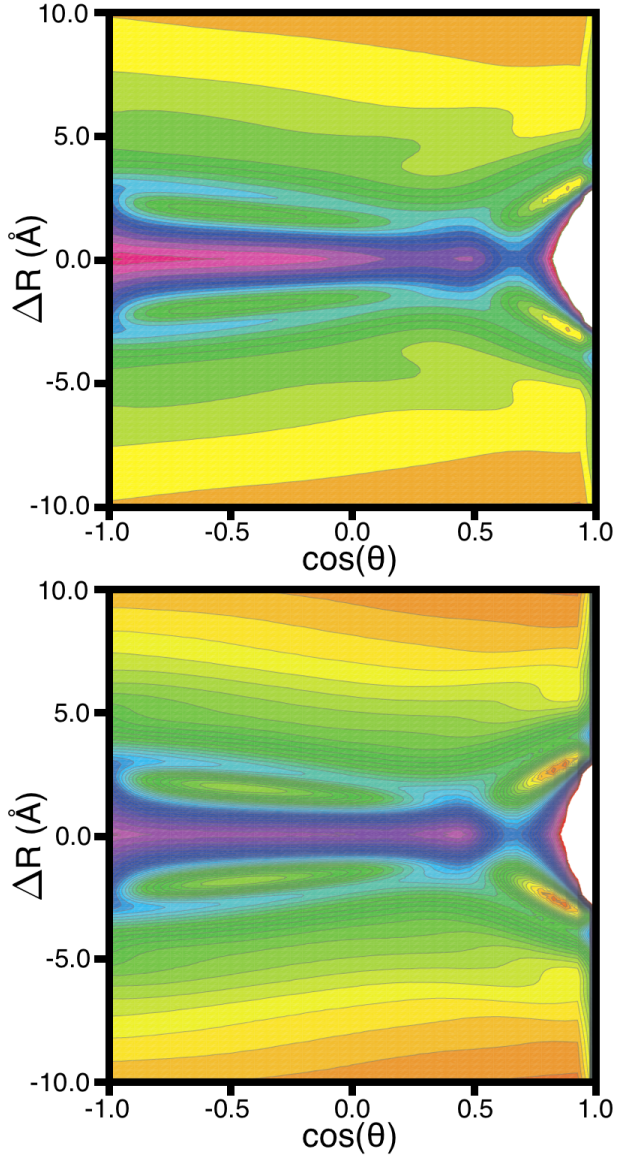

Figure 3.6: Two dimensional free energy profiles are shown for methanol (top) and ethanol (bottom). In each each case the ordinate is $\Delta R = R_{O_A-H_D} - R_{O_X-H_D}$, where H_D is the donor hydrogen atom, O_A is the acceptor oxygen, and O_X is any non-donor/non-acceptor oxygen. The abscissae are $\cos\theta$, where θ is the $H_D O_D O_X$ angle.

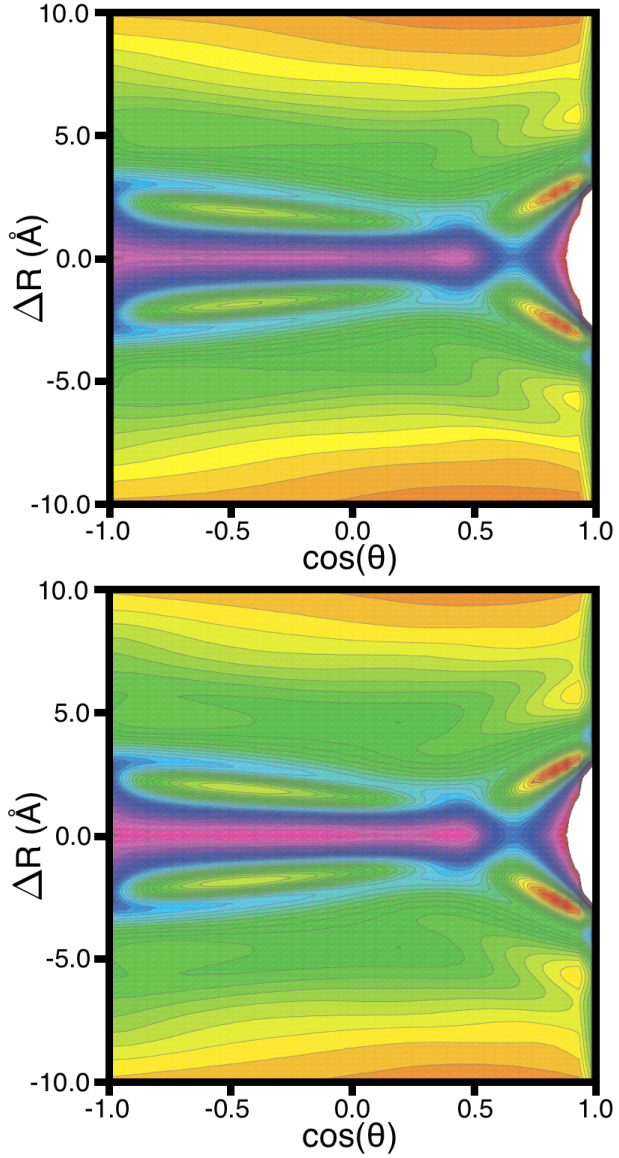

Figure 3.7: Two dimensional free energy profiles are shown for *n*-propanol (top) and *n*-butanol (bottom). In each each case the ordinate is $\Delta R = R_{O_A-H_D} - R_{O_X-H_D}$, where H_D is the donor hydrogen atom, O_A is the acceptor oxygen, and O_X is any non-donor/non-acceptor oxygen. The abscissae are $\cos\theta$, where θ is the $H_D O_D O_X$ angle.

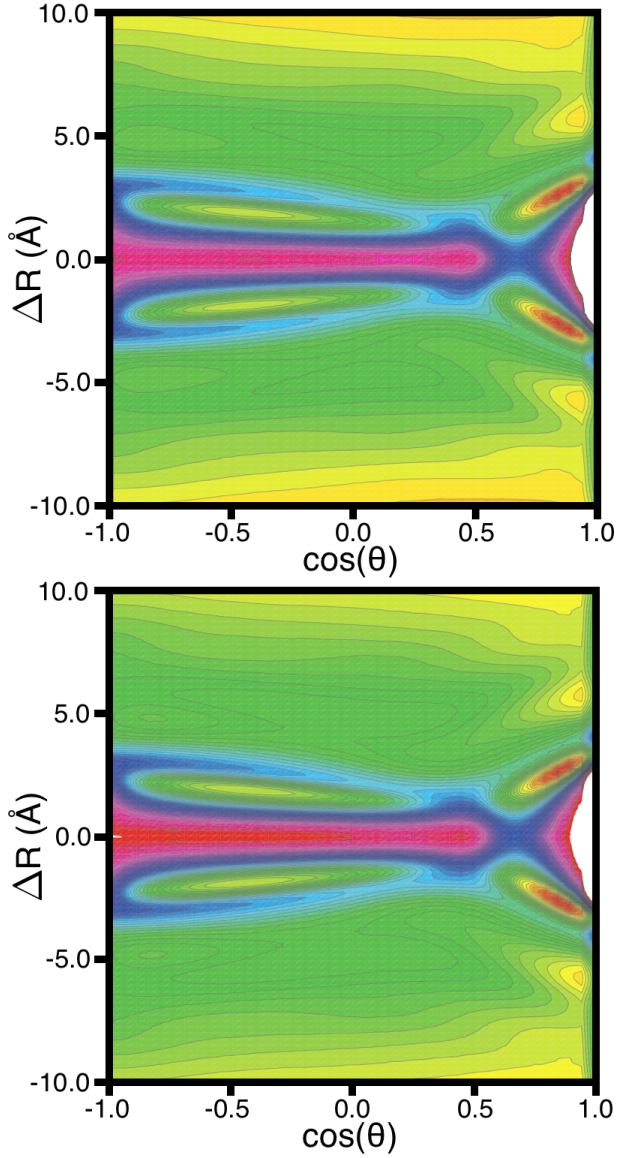

Figure 3.8: Two dimensional free energy profiles are shown for *n*-pentanol (top) and *n*-hexanol (bottom). In each each case the ordinate is $\Delta R = R_{O_A-H_D} - R_{O_X-H_D}$, where H_D is the donor hydrogen atom, O_A is the acceptor oxygen, and O_X is any non-donor/non-acceptor oxygen. The abscissae are $\cos\theta$, where θ is the $H_D O_D O_X$ angle.

or $\theta \approx 140 - 180^{\circ}$), where a broad free energy well is observed. This deepens as a function of hydrophobic bulk, and close to $\Delta R^{\ddagger} = 5$ Å and $\cos\theta = -0.9$ ($\theta \approx 155^{\circ}$), a new free energy minimum can be seen appearing.

On a molecular level, Figures 3.6, 3.7, and 3.8 indicate an overall increased ordering in the liquid as a function of alkyl chain length. Specifically, free energy minima near $\Delta R \approx 4 - 4.5$ Å and $\cos\theta \approx 0.9$ are absent for methanol and ethanol. This minimum appears for *n*-propanol and continues to grow through *n*-hexanol. Thus, second coordination shell occupancy becomes better defined (more directed in the angular coordinate) with increasing alkyl chain length. The increased steric bulk of the alkyl chains results in more isolated chains of hydroxyl groups, and thus higher shell occupancy in the angular coordinate becomes better resolved. This increased ordering is consistent with interpretations from OKE spectroscopy studies [31, 32], in which alignment of longer-chain alcohols is increasingly difficult, as reflected in increasing B values. The enhanced ordering also suggests a way that additional timescales may arise. That is, molecules participating in certain structural elements such as chains may reorient differently than those participating in other structures found in solution. This idea is explored further in Section 3.3.3.

From a kinetic view, the appearance of new timescales in $C_2(t)$ requires that new hydrogen bond exchange pathways emerge. Assuming *DA* represents a "reactant" hydrogen bond and *DB* represents a "product" hydrogen bond, a kinetic scheme such as that shown on the right side of Figure 3.9 must be favored over a reaction scheme such as that shown on the left side of Figure 3.9 for bi-exponential behavior in the long-time component to be observed. The alcohols show an increasingly deep

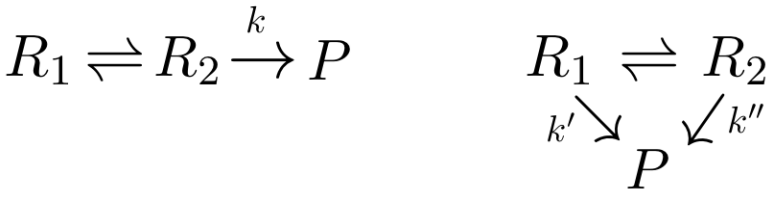

Figure 3.9: *Left*: New free energy minima result in a new population of molecules, R_1, that primarily interconverts with reactants R_2. It is R_2 that leads to the formation of products P. *Right*: For new timescales to emerge, a direct path from both R_1 and R_2 would lead to products P.

free energy minimum at large jump angles ($\cos\theta \approx -0.7$--0.4 or $\theta \approx 153 - 115^\circ$) and short distances ($\Delta R \approx 2$ Å). However, for methanol and ethanol, a single free energy minimum near $\cos\theta \approx 0.9$ ($\theta \approx 25^\circ$) exists. For *n*-propanol through *n*-hexanol, two free energy minima are present near $\cos\theta \approx 0.9$, with the emergent well located at $\Delta R \approx 4.5 - 5$ Å. This is consistent with a single-exponential long-time component to reorientation for methanol and ethanol and bi-exponential long-time reorientation for higher alcohols. Thus, the free energy landscapes of Figure 3.6, 3.7, and 3.8 are qualitatively consistent with the right side of Figure 3.9.

The free energy minima and associated barrier heights in Figure 3.6-3.8 are small, and the corresponding simple transition state theory rate constants do not quantitatively reproduce the timescales calculated for the jump times in Table 3.4. It is likely that one must include the liquid viscosity in the estimates of the rate constants to obtain quantitative agreement with the observed jump times. This can be accomplished using Kramers' theory, in which simple transition state

theory is modified to include effects from a generalized friction term [135]. In the high-viscosity limit,

$$k = k^{TST}\kappa^{KR} = k^{TST}\left(\frac{\omega^{\ddagger}}{\beta}\right), \tag{3.2}$$

where κ^{KR} is a Kramers' theory transmission coefficient, which is related to $\omega^{\ddagger}$, the transition state frequency (which can be obtained directly from the simulation), and β, a generalized friction term. Using the Einstein diffusion equation and assuming the diffusion coefficient, D, can be related to the generalized friction, β, through $D = k_B T/\beta$, Equation 3.2 becomes

$$k = \frac{k_B T}{h}\left(\frac{\omega^{\ddagger}}{6\pi r\eta(T)}\right)e^{-E_a/k_B T}. \tag{3.3}$$

The use of the Einstein equation assumes the particle in question has a spherical hydrodynamic radius, r, an assumption that becomes more severe with longer alkyl chain. Notably, Equation 3.3 also includes $\eta(T)$, the temperature-dependent viscosity, which can be obtained directly from the simulation using Green-Kubo relations. Experimentally, alcohol viscosity increases for increasing alkyl chain length. Consequently, as $\eta(T)$ increases, the rate constant decreases, and the corresponding timescale increases. Thus, including viscosity effects in the rate constant description should result in better agreement between timescales calculated directly from jump time correlation functions and those derived from free energy landscapes.

3.3 Alternative Hypotheses for Emergent Timescales

While the above analysis appears to satisfactorily explain the origin of new longtime reorientational contributions in longer chain alcohols, several alternative hypotheses for the origin of the emergent timescales in higher alcohols were also proposed and tested. While none have proven successful in explaining the emergent dynamics observed here, they have nevertheless been useful in further developing a molecular-level picture of structure and dynamics in liquid alcohols.

3.3.1 Excluded Volume Fluctuations

The excluded volume fraction, f, averaged over all molecules at many times, has been shown to provide a good description of the slow timescale for reorientation in lower alcohols. However, the excluded volume fraction represents a simplified measure of what occurs in solution. Studies indicate that dynamic heterogeneity plays a significant role in the slowed dynamics observed in supercooled water [21]. There, a large distribution of hydrogen bond switching rate constants, $k_{jump} = 1/\tau_0$, is observed as a consequence of local order fluctuations, and a cumulant expansion analysis [136] results in two timescales—k_{short} and k_{long}—for cooled water. (The details of this calculation can be found in [21].) Because of the reasonable success of the excluded volume fraction in predicting the slowing of lower alcohol jump dynamics with increasing alkyl chain length, it is reasonable to speculate that an explanation similar to the supercooled water case applies to the alcohols. That is, perhaps time-dependent fluctuations in the excluded volume fraction, f, provide

a mechanism for the emergence of an additional long reorientational timescales observed in the simulation data.

To extract k_{short} and k_{long} values for alcohols, the excluded volume fraction was calculated for each molecule at each timestep over 8 ns using a transition state ring of 200 points (thereby limiting resolution to $\Delta f = 0.005$.) Assuming a distribution of time-dependent rate constants, the hydrogen bond switching rate constant at a time t, $k_{jump}(t)$ is related to the hydrogen bond switching rate constant for water, $k_w \approx 0.3$ ps^{-1}, modulated by the excluded volume fraction, and $k_{jump}(t) = k_w[1 - f(t)]$. Fluctuations in the rate constant over time are related to fluctuations in the excluded volume, and $\delta k(t) = k_w \delta[1 - f(t)]$. Thus, a correlation function in the rate constant fluctuations,

$$C(t) = \langle \delta k_{jump}(0)\, \delta k_{jump}(t) \rangle, \tag{3.4}$$

can be recast in terms of the excluded volume fraction as a function of time, $f(t)$. The result is

$$C(t) = \frac{\langle f(0)f(t) - \langle f \rangle^2 \rangle}{\langle f^2 \rangle - \langle f \rangle^2}. \tag{3.5}$$

The correlation function (Equation 3.5) was calculated for each alcohol, and the results are presented in Figure 3.10.

The results of the calculation are presented in Figure 3.10. In Figure 3.10, the typical trend for linear alcohols is not preserved, as the positions for *n*-pentanol (green) and *n*-hexanol (brown) appear switched. Accordingly, this cannot explain the trend in reorientation timescales in higher alcohols. Also notable is that the

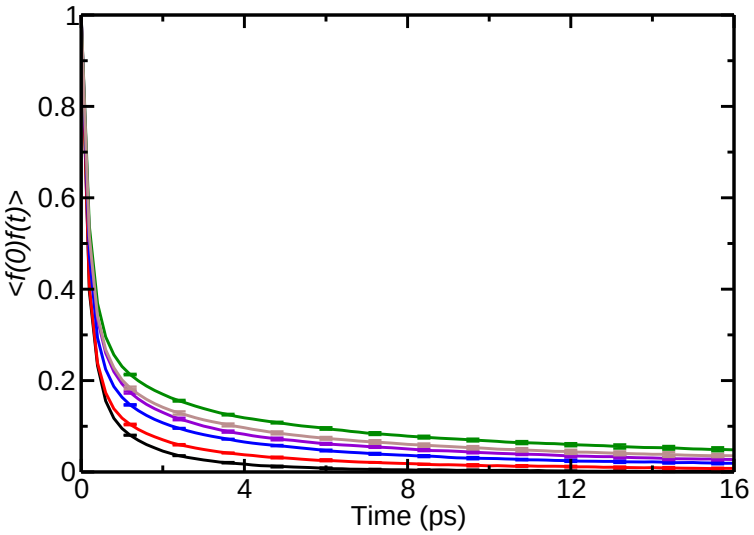

Figure 3.10: The excluded volume correlation functions are presented for methanol (black), ethanol (red), *n*-propanol (blue), *n*-butanol (purple), *n*-pentanol (green), and *n*-hexanol (brown).

correlation functions presented here do not decay to zero in the time interval shown (16 ps). Extension of the correlation function to long times (> 30 ps) still shows non-zero values for $\langle f(0) f(t) \rangle$, and the uncertainties associated with the curves become large. This is to say, the results here are data-limited. A more meaningful calculation of $\langle f(0) f(t) \rangle$ would require calculation of the excluded volume fraction over longer times.

The preceding approach was pursued because it leads directly to two long-time components in the reorientation of supercooled water—an effect similar to the two long-time components in higher alcohol reorientation. However, timescales can also be derived in a more direct fashion, by assuming that a distribution of rate constants are a function of time (see [21]). Briefly, the relevant timescales are fits to the function $S(t) = \langle e^{-\int_0^t k(\tau)\,\mathrm{d}\tau} \rangle$, which can be calculated directly from the simulation by assuming that $k_{water} \approx 0.3$ ps^{-1} and that $k(\tau) = k_{water}\,[1 - f(\tau)]$. The integration over the distribution of time constants from 0 to t then provides an average value for k at the time t. The results of this analysis are presented in Figure 3.11. In Figure 3.11, each curve is reasonably well-fit to a single exponential function. Additionally, the results are not sensitive to the method of integration. The timescales for linear alcohols with 1, 2, 3, 4, 5, and 6 carbon units are 25.5, 37.1, 43.1, 44.0, 44.9, and 84.4 ps, respectively. For methanol, the value of 25 ps is too large, as the single jump time is ≈ 15 ps. For *n*-hexanol, the value of 84.4 ps fails to match either the faster (36.2 ps) or slower (109.2 ps) timescales. (See Table 3.4.) Additionally, the values for *n*-propanol, *n*-butanol, and *n*-pentanol are very closely clustered. Accordingly, the results from this analysis fail to provide insight

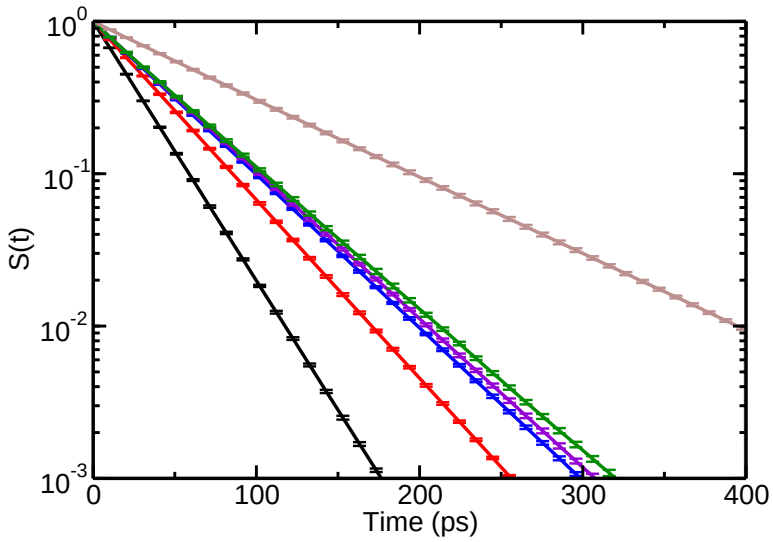

Figure 3.11: The functions $S(t)$ calculated from time-dependent rate constants, $k(\tau)$, are presented for methanol (black), ethanol (red), *n*-propanol (blue), *n*-butanol (purple), *n*-pentanol (green), and *n*-hexanol (brown).

about the trend in reorientation across the alcohol series, let alone the origin of new timescales.

3.3.2 Hydroxyl Coordination Number

A particularly useful quantity for studying liquids is the radial distribution function, $g(R)$, a quantity which reflects the local density. The function can be calculated according to Equation 3.6 as described by Allen and Tildesley [137]:

$$g(R) = \frac{V}{N^2} \left\langle \sum_{i}^{N} \sum_{j \neq i}^{N} \delta(R - R_{ij}) \right\rangle . \tag{3.6}$$

In the simulation, a site i is chosen, and the distances to all other sites j are calculated. For practical purposes, the δ function is assumed to have some small, finite width, and the distances R_{ij} are histogrammed. This is performed over all N sites and over many configurations. Lastly, the resulting function is compared at each R to the number of sites in a system of bulk density of the same volume,

$$N_{id} = \frac{4\pi\rho}{3} \left[(R + \delta R)^3 - R^3 \right] = \frac{4\pi N}{3V} \left[(R + \delta R)^3 - R^3 \right]$$

The results are shown in Figure 3.12.

The intensity in the first $g(R_{OO})$ peak for each alcohol increases with increasing alkyl chain length (Figure 3.12, top). As shown in the bottom of Figure 3.12, with the exception of methanol, the trend is preserved in the second maximum. However,

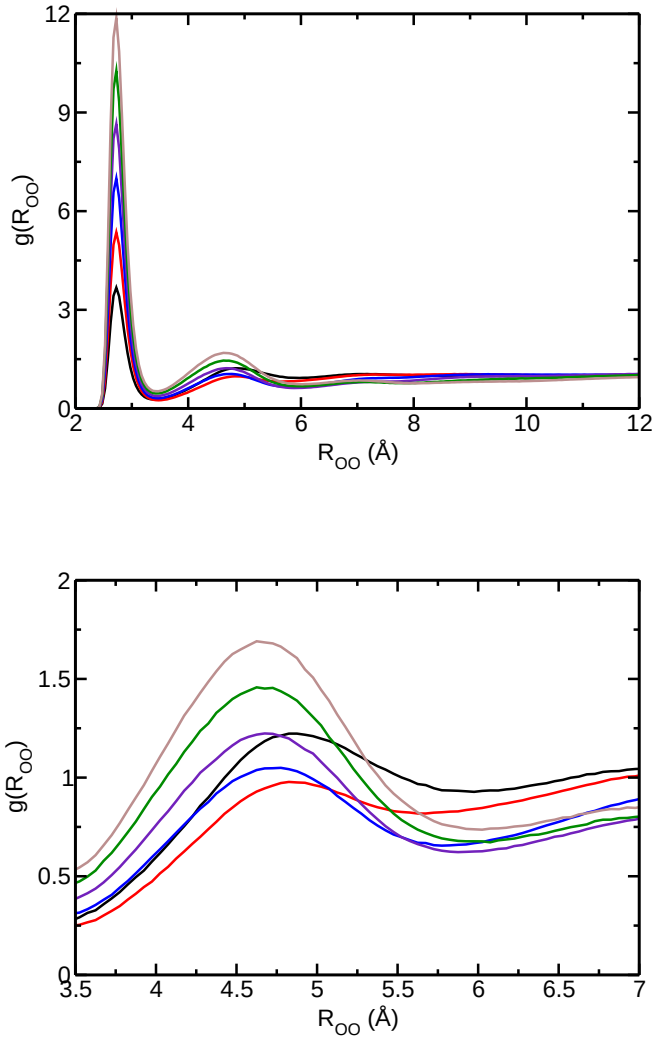

Figure 3.12: The radial distribution functions $g(R_{OO})$ are shown for methanol (black), ethanol (red), *n*-propanol (blue), *n*-butanol (purple), *n*-pentanol (green), and *n*-hexanol (brown). The largest, initial peak in each curve (shown top) represents the first coordination shell. The second coordination shell is represented by a smaller secondary peak (shown bottom).

the nature of the curves $g(R_{OO})$ quickly changes, and any easily described trend is lost by the second minimum.

A more intuitive measure of what occurs in solution might be obtained by calculating the coordination number n from $g(R_{OO})$. The minima in curves $g(R)$ are often used as a convenient demarcation of coordination shell boundaries. Thus, the limits of the first coordination shell would fall between zero and the first non-zero minimum in $g(R)$. The coordination number, n, is then the integral of $g(R)$ over this region, *viz.* the equations

$$n_1 = \int_0^{R_{OO,min_1}} 4\pi r^2 g(R_{OO})\,\mathrm{d}r \tag{3.7}$$

and

$$n_2 = \int_{R_{OO,min_1}}^{R_{OO,min_2}} 4\pi r^2 g(R_{OO})\,\mathrm{d}r = \left(\int_0^{R_{OO,min_2}} 4\pi r^2 g(R_{OO})\,\mathrm{d}r\right) - n_1 \tag{3.8}$$

Because the average jump mechanism in water begins with a new acceptor leaving the second solvation shell and entering the first, it is reasonable to suspect that changes in dynamics may relate to the number of available acceptors within the solvation shells or the relative mobility of acceptors moving between solvation shells. Figure 3.13 indicates that the numbers of members in the first and second coordination shells change very little as a function of alkyl chain length for ethanol to *n*-hexanol, and the methanol case is an outlier. Accordingly, changes in available local population of acceptor molecules cannot explain the trend in—let alone emergence of—timescales across the alcohol series. However, the information

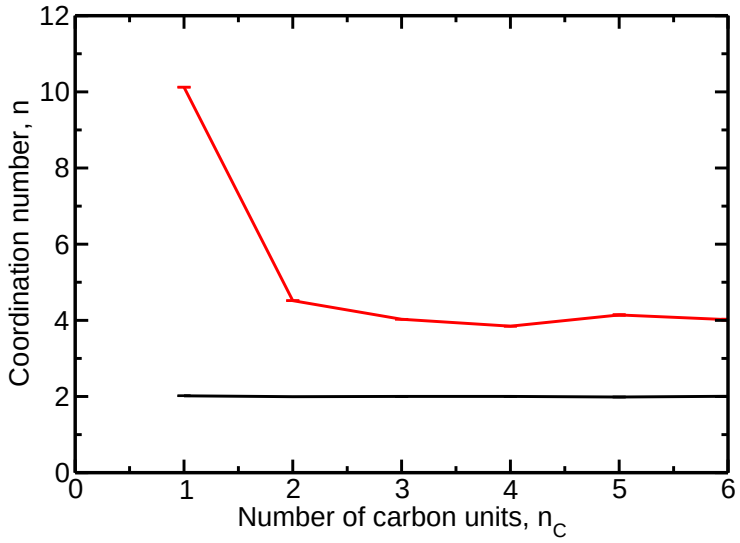

Figure 3.13: The number of molecules residing in coordination shells 1 (black) and 2 (red) is shown as a function of alkyl chain length. Error bars are similar in size to the line thickness.

in Figure 3.13 is consistent with Figure 3.6-3.8, which show increased chain formation across the alcohol series. The small steric bulk associated with the methyl group of methanol allows densely packed hydrogen bond chains, and a large second coordination sphere population (reminiscent of networked water) results. Longer alkyl groups better separate chains of hydrogen bonded hydroxyl groups. The second coordination sphere therefore consists primarily of hydroxyl oxygens within the hydrogen bond chain containing the central (reference) oxygen. Such an effect which should plateau quickly, which is shown by the red curve of Figure 3.13.

In the case of water, the incoming hydrogen bond exchange partner moves from the second to the first solvation shell as an initiating step in the jump mechanism. While the results in Figure 3.13 show that there is no general change in the coordination numbers results across the alcohol series, they do not provide a dynamic picture of the rates of exchange between first and second coordination shells. For a hydrogen bond, it is possible that the time for hydrogen bond switching is related to whether or not the future acceptor is in the first solvation shell at time t_0 or if the future acceptor must move from the second to first solvation shells. To address this, the side-side correlation functions for future acceptor (molecule *B*) residence or non-residence within the first coordination shell were calculated according to Equations 3.9 and 3.10, respectively.

$$C_{n_1}(t) = \langle \theta_{n_1}(0)\theta_{n_1}(t) \rangle \tag{3.9}$$

$$C_{\not n_1}(t) = \langle \theta_{\not n_1}(0)\theta_{n_1}(t)\rangle \tag{3.10}$$

For each molecule, lists of first and second shell neighbors are constructed for each time in the simulation. The time for a hydrogen bond to switch is calculated as before (see Equation 2.12). Here, however, the correlation functions are decomposed by the location of the future acceptor relative (B) to current donor (D)—*i.e.*, whether or not B was within the first solvation shell of D at time t_0. As usual, the time constants can then be found by multi-exponential fitting of the curves $S_{n_1}(t) = 1 - C_{n_1}(t)$ and $S_{\not n_1}(t) = 1 - C_{\not n_1}(t)$. These curves are presented in Figure 3.14. For each alcohol represented in Figure 3.14, the timescale associated with B *not* in the first coordination shell at t_0 (dashed lines) is always longer than the case in which B is in the first coordination shell at t_0. If B is within the first solvation shell at t_0, it implies proximity to D and more facile hydrogen bond switching. Similarly, if B is *not* within the first solvation shell of D at time t_0, it implies that B must move from the second to first solvation shell to accept a hydrogen bond from D, a process that takes more time. Also apparent from Figure 3.14 is that the trend for both cases is preserved across the alcohol series. That is, timescales shortest to longest always fall in order of increasing alkyl chain length.

Table 3.6 provides tri-exponential fit data for B within the first solvation shell at t_0, while the same information for B *not* in the first solvation shell at t_0 is provided in 3.7. The results in Table 3.6 do not correspond well to either jump (Table 3.4) or frame (Table 3.5) times. However, for the longer- and longest-time components (τ_b and τ_c, respectively) in Table 3.7, there is striking similarity to the longer- and

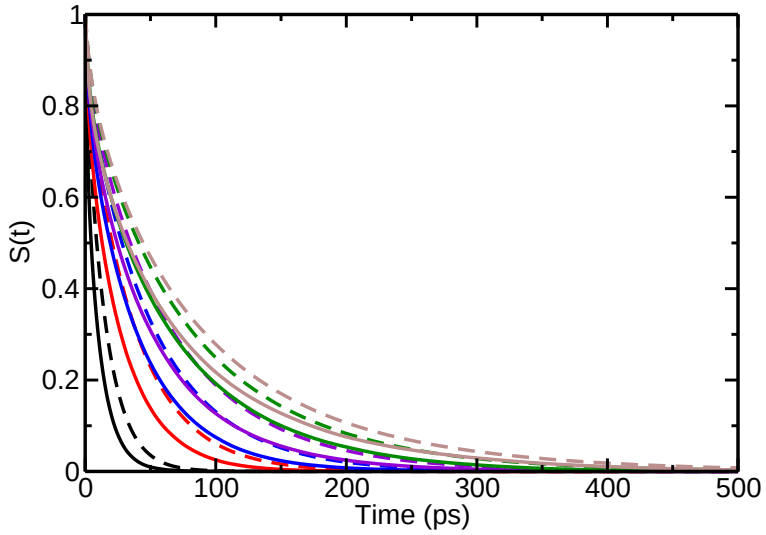

Figure 3.14: Correlations for hydrogen bond switching are shown for cases in which the future acceptor (molecule *B*) is (solid lines) and is *not* (dashed lines) in the first coordination shell at time t_0 (solid lines) for methanol (black), ethanol (red), *n*-propanol (blue), *n*-butanol (purple), *n*-pentanol (green), and *n*-hexanol (brown).

Table 3.6: Correlation times (in ps) for first coordination shell occupancy

Molecule	A_a	τ_a	A_b	τ_b	A_c	τ_c
MeOH	0.287	1.7	0.713	11.5	-	-
EtOH	0.176	2.1	0.076	8.9	0.748	29.6
n-PrOH	0.164	2.3	0.099	13.8	0.767	43.7
n-BuOH	0.164	2.6	0.210	25.4	0.626	61.6
n-PnOH	0.143	2.6	0.153	19.9	0.704	77.0
n-HaOH	0.178	3.0	0.278	33.6	0.544	101

Table 3.7: Correlation times (in ps) for first coordination shell *non*-occupancy

Molecule	A_a	τ_a (ps)	A_b	τ_b (ps)	A_c	τ_c (ps)
MeOH	0.122	1.9	0.878	15.6	-	-
EtOH	0.106	2.7	0.034	8.7	0.860	37.7
n-PrOH	0.103	3.0	0.073	14.5	0.824	54.2
n-BuOH	0.118	3.8	0.114	25.2	0.768	70.9
n-PnOH	0.119	4.1	0.162	28.7	0.719	92.6
n-HaOH	0.133	4.8	0.239	40.0	0.628	112

longest-time components in the jump times reported in Table 3.4. Importantly, the results in Table 3.7 reflect times for hydrogen bond switching for the molecule *B* not in the first solvation shell. That is, similar to the average water mechanism, the future hydrogen bond acceptor molecule *B* in linear alcohols is, on average, removed from direct contact with *D*. The hydrogen bond jump from *A* to *B* thus requires movement of *B* into the first solvation shell of *D*, and this is reflected in the dynamics in Table 3.7. While the information is relevant to developing a molecular-level picture of hydrogen bond switching, it does not address, *per se*, the origin of the new timescales.

3.3.3 Structural Characterization

While changes in the local coordination shells fail to explain the longer and emergent timescales observed for higher alcohols, it is clear that the alcohols have different local coordination environments. This naturally leads to the question of altered solution structure. That is, another hypothesis is that the emergence of new timescales arises from changes in the larger-scale liquid structure. For example, do rings of hydrogen bonded molecules increase with increasing alkyl chain length at the expense of some other structural form, such as linear chains? Do the hydrogen bonds within these structures have associated with them different dynamics?

To address this possibility, a systematic way of identifying and assigning various structures anticipated to exist in solution was devised. Structural determination and assignment effectively reduces to determining differences in connectivity. It was previously discussed that lists of hydrogen bond donors and acceptors at each time can be constructed. Molecules with no acceptor are considered "lone" molecules. Additional structural determination amounts to recursively finding a donor-acceptor pair, assigning the acceptor a donor status, and interrogating the lists for its acceptor. This process is repeated until either no acceptor is found (chain termination) or the next acceptor is a molecule already participating in the chain. In the first case, termination at the first step indicates a "pair". If additional processing occurs with chain termination, the series of molecules are participating in a "chain." If the next acceptor is a molecule already participating in the chain, it is a "ring" if the molecule is the initiating donor and is a "lariat" if the molecule is not the initiating donor. This approach does not account for branching, however. In alcohols, a

single molecule very rarely serves to donate a hydrogen bond simultaneously to two donors. However, it often occurs that a hydroxyl group can accept two hydrogen bonds (and very rarely 3). Thus, the structures determined above, may individually be part of larger structures, which all share a common terminus.

Thus, the complete structural assignment involves identifying common termini and eliminating redundancy. When this approach is taken, molecules can be structurally assigned as "lone," "pair," "v-shaped structure," "chain," "lariat," or "ring." Chain and lariat structures can be further characterized by the number of branch points, if desired. Each molecule at each time is assigned a number (1-6, respectively), corresponding to the structure in which it belongs. An example of this process taken from the methanol simulation is presented in Figure 3.15. In Figure 3.15, the hydroxyl groups of 22 hydrogen bonded methanol molecules are shown. The common terminus is indicated in carmine. Importantly, 4 chains converge to this point, and thus there are 4 origins, indicated in pink. All molecules participating in the chain are assigned the number 4.

The side-side correlation function approach can be adapted to determine the lifetime of a molecule within a given structural type. Additionally, the parsing can be done such that molecule types can be combined. For example, if a molecule is part of a pair and in the next step is part of a chain, it is likely that the acceptor molecule was in proximity to a third (or several) molecule(s) and the overall structure did not change much. The function can be modified so that molecules tagged as 5 at $t = 0$ and then 2 at time $t = t'$ (or similarly, 2 at $t = 0$ and 5 at $t = t'$) are considered as not changing structural type at time t'.

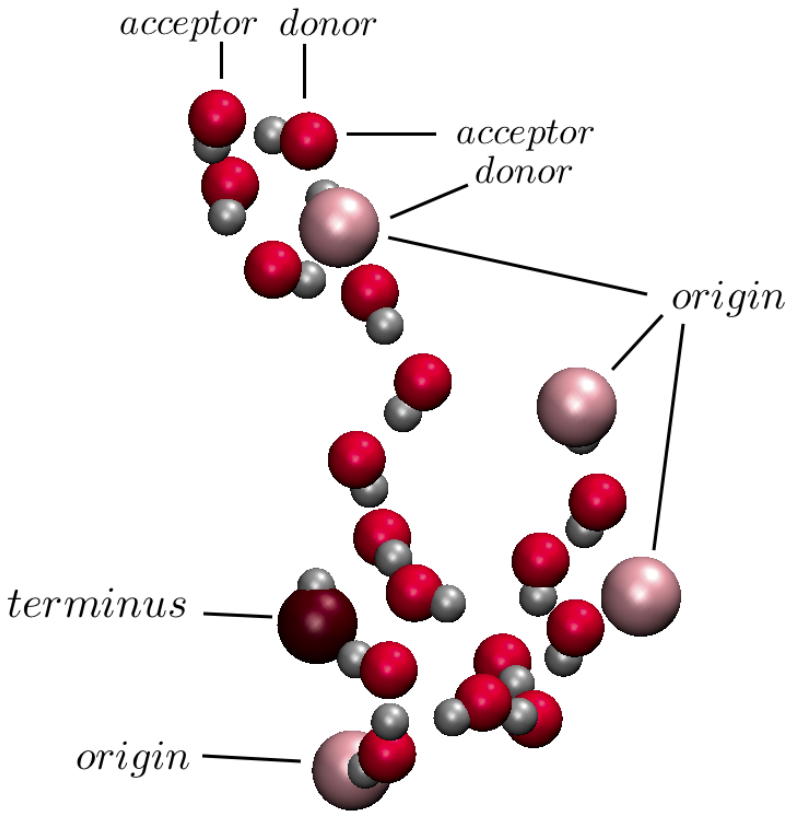

Figure 3.15: Branchings chain are present in simulations of methanol. Only oxygens (red) and hydrogens (silver) are shown for hydrogen bonding hydroxyl groups. To identify this chain structure, a molecule acting as a hydrogen bond donor but not an acceptor is considered as an origin (highlighted in pink). The donor-acceptor relationship is then shifted pairwise along the chain recursively. A molecule identified as an acceptor but not a donor is considered the terminus (highlighted in carmine). Here, four chains of varying length (7, 4, 9, and16 molecules) have been identified with a common terminus (molecule number 179). Redundancies among the chains can be identified and eliminated by working backward from their common terminus. The remaining 22 unique molecules comprise a chain with 3 branch points. Each of these 22 molecules is thus assigned a structural identification number of 4 for this configuration.

Preliminary data for structure-associated dynamics calculated in this way suggest that structural dynamics fail to correspond to the timescales observed in either the frame time contributions or jump time contributions to $C_2(t)$. However, chain structures such as the one represented in Figure 3.15 are found in all the alcohols, and the chains lengthen for longer alkyl chains. Accordingly, the structural approach taken here can be used in studies focused on the increased ordering with increased alkyl chain length.

3.4 Higher Alcohol Reorientation Summary

The series of linear alcohols of increasing chain length, from methanol to *n*-hexanol, were investigated by MD to investigate their reorientation dynamics within the context of the extended jump model. The long-time reorientation occurs on two timescales for longer alcohols, an effect that can be traced to the hydrogen bond switching dynamics. The distribution of jump angles for hydrogen bond switching can be traced to local hydrogen bonding relationships among hydrogen bond donor, current acceptor, and future acceptor. Free energy decompositions show increased molecular ordering in the liquid and the emergence of new free energy barriers. These barriers result in multi-exponential timescales, but to make the results quantitative, additional effects, such as viscosity, should be considered.

During investigation of the origin of emergent timescales in higher alcohols, several alternative hypotheses were proposed and tested. Excluded volume fluctuations in the alcohols were investigated as these fluctuations in supercooled water

were able to explain emergent timescales in supercooled water. The hydroxyl coordination number was investigated, as changes in the number of locally available hydrogen bond exchange partners were hypothesized to change the reorientational timescales. Lastly, it was hypothesized that the larger scale structures in which a hydroxyl group participates could have associated with them distinct timescales. While none of these hypotheses satisfactorily explain the emergent timescales in Äreorientation dynamics in linear alcohols, their pursuit has resulted in additional dynamic and structural information about the bulk liquids.

Chapter 4

Solvation Dynamics in Confined Systems

Time-dependent fluorescence (TDF) has been used extensively to measure solvation dynamics, and has been nearly exclusively used to study changes in dynamics in nanoconfined systems, as discussed in Chapter 1. However, the reported timescales for a given solvent can depend strongly on the properties of the reporter dye. As discussed in Section 1.4, the TDF signal in confinement generally shows elongated timescales and often shows new or emergent timescales that have no bulk counterpart. The origins of these emergent timescales is still unclear, and several hypotheses have been proposed to explain them. In the solute diffusion hypothesis, the motion of the dye itself manifests in the TDF signal and thereby contributes new timescales. The present Chapter uses equilibrium molecular dynamics (MD) simulations of a model solute to test this hypothesis and provide insight about nanoconfined systems in general.

4.1 Model Systems for Nanoconfined Ethanol

A spherical, dipolar model solute molecule used in this work consists of three approximately collinear sites—one of center of positive charge (P), center of mass (COM), and center of negative charge (N)—placed in the sphere, with the COM at the center. The P-N distance was maintained at $R_{P-N} = 3.2$ Å so that the change in dipole moment is fully attributable to changes in the electrostatic charges assigned to the P and N sites. In this way, the dipole moments, given in Table 4.1, arise from

Table 4.1: Stockmayer solute charges and dipole moments

q (e)	μ (Debye)
0.32532	5
0.65064	10
0.97596	15

equal positive and negative charges (also listed). Masses of 50 u were assigned to each charge site. All three sites are contained within a Lennard-Jones sphere centered on the COM site. Values of $\sigma = 7.5$ Å and $\varepsilon = 0.500$ kJ mol^{-1} were maintained for all dipole moments of the solute. Within the confined solvent systems, the COM site was also used to fix the solute in position. Thus, the model solute comprises a dipole that rotates within an approximately spherical bubble that interacts with both the solvent and the confining interface, and how the solute interacts with solvent and confining framework can be studied as a function of the solute location within the confining framework.

The dipole moments in Table 4.1 also allow different transitions to be studied. That is, transitions from ground state to excited state corresponding to either

$5D \rightarrow 10D$, or $5D \rightarrow 15D$, or $10D \rightarrow 15D$ can be used to model absorption, while the corresponding transitions $10D \rightarrow 5D$, $15D \rightarrow 5D$, and $15D \rightarrow 10D$ can be used to model fluorescence.

To confine ethanol and the model Stockmayer solute, the mesoporous amorphous silica models developed by Gulmen et al. [**?**] were used. Specifically, the pore is approximately cylindrical in shape with radius $\sim$ 12 Å and axis length 30 Å. The small size was chosen because the effects of confinement typically increase with decreasing size of the confining framework. The pore contains 36 silanol groups and 6 geminal silanol groups, which facilitate study of specific chemistry within the pore. The same pore is rendered hydrophobic by setting the charges of all pore atoms to zero. Parameters describing the pore atoms are provided in Table 4.2 with any cross-term parameters calculated as before (Equations 2.4 and 2.5).

Table 4.2: Force field parameters for the silica pore

Atom	m (g mol^{-1})	q (e)	σ (Å)	ε (kJ mol^{-1})
$H_{silanol}$	1.00	0.420	1.295	0.00153
$O_{silanol}$	16.00	-0.740	3.070	0.71107
O_{SiO_2}	16.00	-0.640	2.700	1.91151
Si_{SiO_2}	28.00	1.280	2.500	0.00042

The bulk ethanol system described in Section 2.1 with the solute at the center of the box was confined in a silica nanopore by overlapping the bulk system and silica pore and subsequently eliminating molecules that had sites that overlapped with the silica framework. A total of 121 ethanol molecules remained, which is in quantitative agreement with grand canonical Monte Carlo simulations on neat ethanol. A cutaway of the resulting system is shown in Figure 4.1. Notably, the

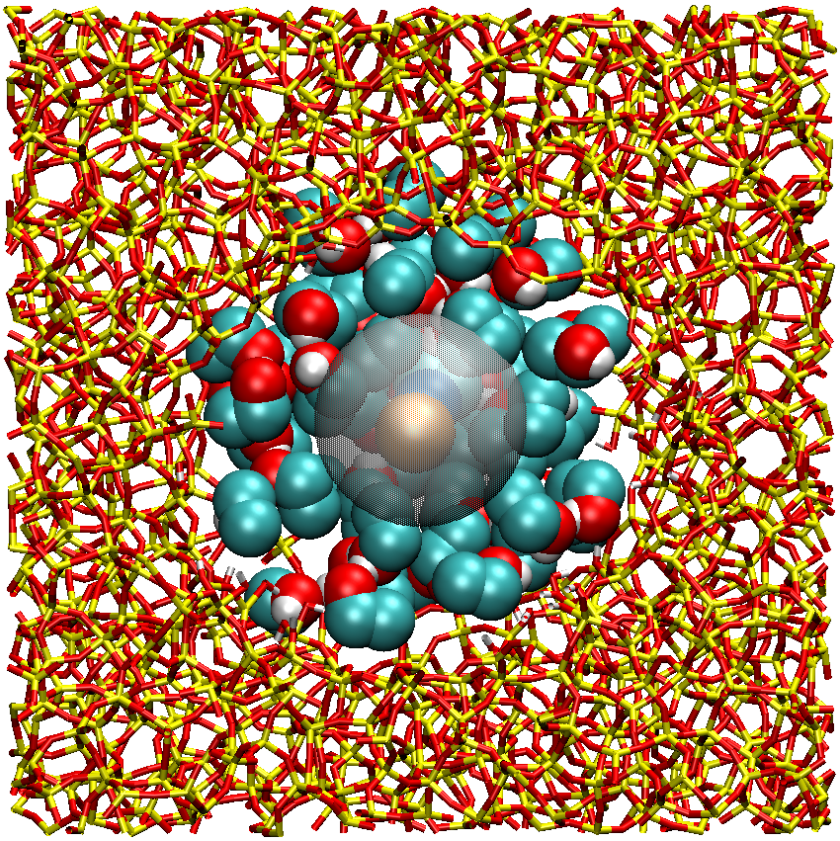

Figure 4.1: The model solute (centered, translucent sphere) dissolved in ethanol (space-filling, colored), and confined within a silica pore (licorice, colored) is shown. The hydrogen (white), oxygen (red), and methylene and methyl groups (cyan) of ethanol can be seen surrounding the solute and interacting with the silica surface. The silanol hydrogen (white) and oxygen (red) atoms can be seen near the interface. Notably, the silicon (yellow) and oxygen (red) density at the interface and in the framework is nonuniform, *i.e.*, it creates irregular recesses and voids that molecules can occupy.

ethanol Lennard-Jones parameters were changed from zero to $\sigma = 1.295$ Å and $\varepsilon = 0.00153$ kJ mol^{-1} to avoid spurious interactions with the silica pore. The introduced parameters showed no effect on the bulk ethanol structure. Classical MD simulations were run using the DL_POLY_2 [123] software package. Each system was run in the *NVT* ensemble and equilibrated for 200 ps, followed by a 2 ns collection stage using a 1 fs time step. Configurations were recorded every 100 fs except for calculation of solute position-dependent spectra, for which information was collected every 20 fs. Uncertainties were calculated at the 95% confidence level using Student's *t*-test and 5 blocks.

4.2 The Solute Diffusion Hypothesis

As described in Chapter 1, time-dependent fluorescence (TDF) measurements on nanoconfined systems frequently report the emergence of new timescales. All timescales are customarily attributed to motion of the solvent, as they are in the corresponding bulk cases. However, the nanoconfining framework introduces an anisotropy in the system. Both solvent and solute can interact with the confining framework near the framework interface, and may thus interact differently with one another near and away from the interface. This spatially-dependent interplay among system components can clearly complicate the TDF signal. Thus, the interpretation that the TDF signal carries information only about altered solvent dynamics in nanoconfined systems is incomplete at best. To better understand the

information content of the TDF signal, it is necessary to examine how the solute itself is affected by nanoconfinement.

If the TDF signal in nanoconfined systems is sensitive to solute motion, three requirements must be satisfied: 1) The solute must move within the confining framework during the experiment, and the solute must show a preferential residence in the confined system based on charge distribution. That is, the excitation must drive the motion of the solute within the confining framework. 2) The fluorescence energy must change with solute position in the confining framework. These two requirements imply that upon excitation, the solute moves across the confining framework and changes its fluorescence signal as it does so. The TDF signal would therefore also change. To what extent is this observable? The third requirement, which addresses this question, is that 3) this change in the TDF signal must occur on the experimental timescale and with measurable amplitude.

With a model confined system already in place (Section 4.1), the remainder of the present chapter outlines results from equilibrium (MD) simulations that test requirements 1 and 2. Addressing requirement 3) requires non-equilibrium simulations and forms the majority of Chapter 5.

4.3 Free Energy and Position Distributions

To address the possibility that the model solute exhibits a position preference within the pore based on charge distribution, a thermodynamic approach was taken. That is, Helmholtz free energies were calculated as function of solute position across

the pore, and the resulting free energy profiles were used to calculate position probability distributions.

The pore is centered on the origin with its axis along the z direction. Keeping in mind the periodic boundary conditions, the $z = -10$ Å, 0 Å, and $+10$ Å planes are evenly spaced along the pore axis. To explore these "cuts" across the pore more efficiently, the line $y = 0$ Å (*i.e.*, x axis) was used to move the solute across the pore at regularly spaced intervals, $\Delta x = 0.2$ Å. For each cut in z, a starting x_0 value was chosen to reflect strong repulsion of the solute by the pore wall. That each cut has a different x_0 position is a reflection of the surface heterogeneity of the pore. All thermodynamic integration calculations for a given cut always start at the associated x_0 value.

The potential on the solute COM site was calculated according to the equation

$$U = \sum_{i=1}^{N_{cut}} \left\{ 4\varepsilon \left[\left(\frac{\sigma}{r_{iCOM}} \right)^{12} - \left(\frac{\sigma}{r_{iCOM}} \right)^{6} \right] + \sum_{\alpha=N}^{P} \left[\frac{q_i q_\alpha}{4\pi\varepsilon_0 r_{i\alpha}} \right] \right\} \tag{4.1}$$

The index i runs over all N_{cut} solvent and pore sites that fall within a cutoff distance to the solute COM site, $r_{cut} = 15$ Å, and applying period boundary conditions. The index α runs over the charged solute sites P and N. Thus, $r_{iCOM} = |\underline{r}_i - \underline{r}_{COM}|$ and $r_{i\alpha} = |\underline{r}_i - \underline{r}_\alpha|$ represent distances between solvent and pore sites i and the solute sites. The potential on the solute, U, was then used to calculate the force acting on the solute in the direction $\hat{x}$, according to

$$F_{x'}(\vec{r}) = -\vec{\nabla}_r U(\vec{r}) \cdot \frac{\partial r}{\partial x}\hat{x} \tag{4.2}$$

Here, x and r refer to the solute COM only. Importantly, the position of the solute COM, indicated as x', was held fixed while the P and N sites were allowed to rotate. The forces acting on the solute at x' were then averaged over time. Performing this for solute positions in the pore beginning at x_0 and running to x' by increments of Δx results in a profile of average forces at each position in the pore. Integration of these average forces leads to the Helmhotz free energy, as per

$$\Delta A(x) \equiv A(x) - A(x_0) = -\int_{x_0}^{x} \langle F_x(x'; y, z) \rangle dx'. \tag{4.3}$$

This process was repeated for 5, 10, and 15 Debye solute models in hydrophilic and hydrophobic pores at $z = 0$ Å, and for the 5 and 10 Debye solute models in the hydrophilic pore at $z = -10$ Å and $z = +10$ Å. Notably, the resulting curves can be translated into the position probability distributions using the relationship

$$P(x) = \frac{e^{-\beta \Delta A(x)}}{\int e^{-\beta \Delta A(x')} \mathrm{d}x'}. \tag{4.4}$$

The results from the calculation of $\Delta A(x)$ and $P(x)$ for the model solute along x for the $z = 0$ Å cut across the hydrophilic pore are presented in Figure 4.2. For the free energies shown in the lower panel, the minimum for each $\Delta A(x)$ curve has been set to zero. The 5 D solute (black curve) shows a free energy profile that rises dramatically at $x = -9$ Å and $x = +7$ Å. The profile between these points shows very small undulations on an otherwise flat profile. The associated $P(x)$ profile shown in the upper panel indicates that the solute can sample most of the hydrophilic pore for this cut. A notable exception is the left side ($x < 0$ Å)

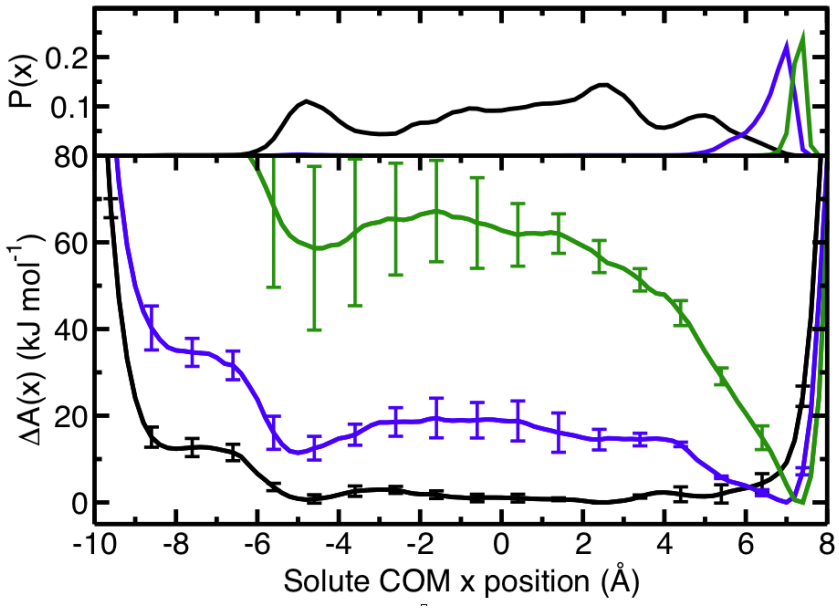

Figure 4.2: The lower panel shows the Helmholtz free energy as a function of the solute COM position, x, for the $z = 0$ cut across the hydrophilic pore for the 5 (black), 10 (blue), and 15 (green) Debye solute models. The free energy global minimum has been set to zero for each curve. The upper panel shows the corresponding position probability distribution $P(x)$ of the solute, as determined by Equation 4.4. The $P(x)$ curves for the 5 D and 15 D solute have been scaled by 5 and $1/2$, respectively.

of the pore, where a shoulder in the free energy profile exists. The 10 D solute (blue curve) is qualitatively similar to the 5 D case, although a defined free energy minimum appears on the right side ($x > 0$ Å) of the pore. Other features in the 5 D case, such as the free energy undulations and shoulder, are present for the 10 D case, but are magnified. The 10 D position probability distribution indicates that the solute is most likely found on the right side of the pore, near the interface. These trends continue for the 15 D solute (green line), and importantly, the free energy minimum becomes deeper and shifts slightly to the right. Notably, the $P(x)$ curves have been scaled by 5 and $1/2$ for the 5 D and 15 D solutes, respectively. Thus, it is clear that modest changes in charge distribution can result in large changes to the location of the solute within the pore. Importantly, the locations in the pore accessed by the 10 D and 15 D solute are not accessible to the 5 D solute. Thus, in the hydrophilic pore for $z = 0$ Å, it is clear that a change in charge distribution can result in a dramatic change in the solute location in the pore.

This appears to be a general phenomenon, as shown in Figure 4.3 and Figure 4.4, which show the free energy profiles ($\Delta A(x)$, lower panels) and position probability distributions ($P(x)$, upper panels) for 5 D (black) and 10 D (blue) solutes for the cuts at $z = -10$ Å and $z = +10$ Å in the hydrophilic pore. In each case, the 5 D free energy profile is mostly flat, and the solute can sample the pore interior. The free energies and distributions differ between the two cuts. Of the two, the $z = +10$ Å case is the more interesting. In Figure 4.4, a minimum in the free energy appears on the right side of the pore ($x > 0$ Å), the same location a shoulder exists for the 5 D solute. Thus, the corresponding position probability distributions show that the

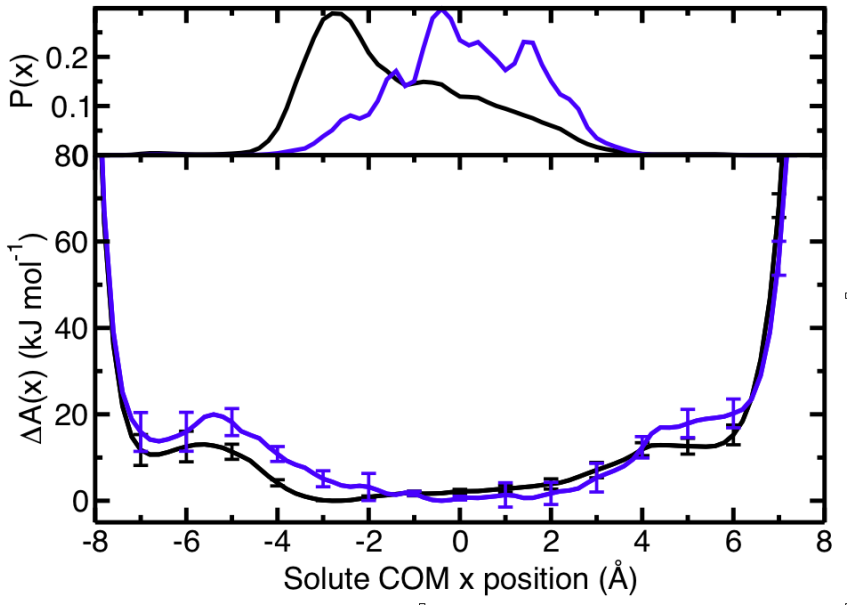

Figure 4.3: The Helmholtz free energy as a function of solute COM position, x, along the cut $z = -10$ Å within a hydrophilic pore are shown in the lower panel for the 5 (black) and 10 (blue) Debye solute. The upper panel displays the corresponding position probability distributions, $P(x)$.

10 D solute can sample regions near the pore interface where the 5 D solute does not. This is similar to observations made in the $z = 0$ Å case. The pore features that give rise to this behavior are explored in Section 4.3.2.

The free energy profiles for solutes of various dipole moment in the hydrophobic pore along the $z = 0$ Å cut are shown in Figure 4.5 and can be compared to the hydrophilic case in Figure 4.2. The overall shape of the free energy profiles shown in the bottom panel are similar to those in the hydrophilic pore case. Large free energy values are found near $x = -9$ Å and $x = +7$ Å; a shoulder and small undulations are present in the region between these values. Note that in the

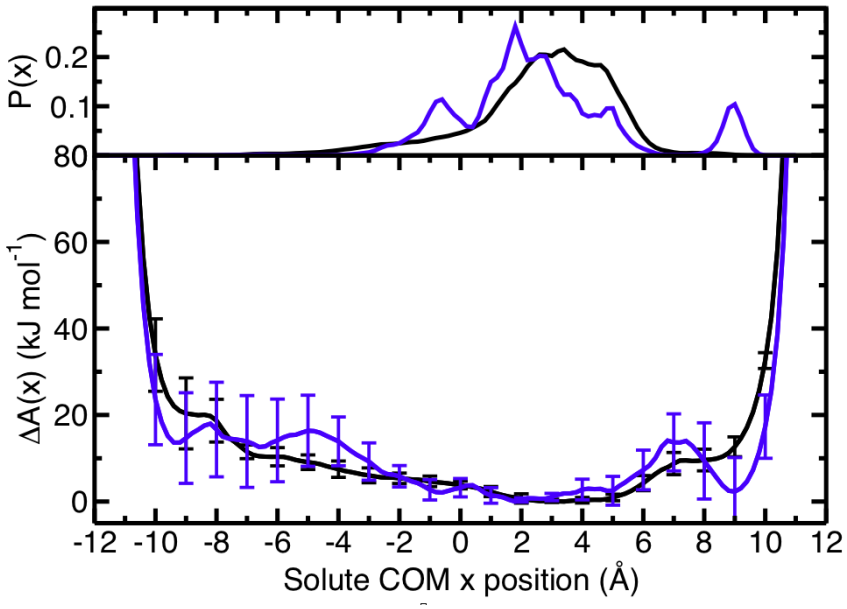

Figure 4.4: The Helmholtz free energy as a function of solute COM position, x, along the cut $z = +10$ Å within a hydrophilic pore are shown in the lower panel for the 5 (black) and 10 (red) Debye solute. The upper panel displays the corresponding position probability distributions, $P(x)$.

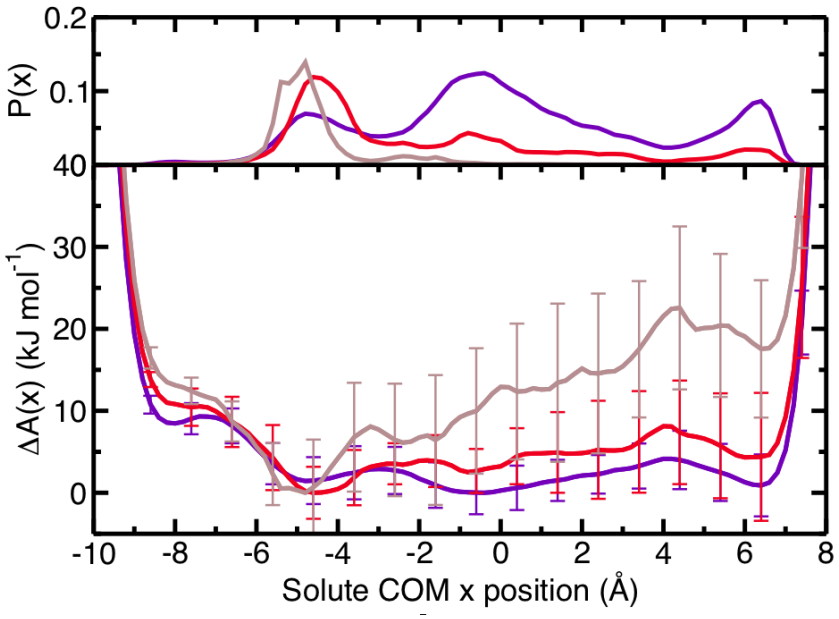

Figure 4.5: The Helmholtz free energy as a function of solute COM position, x, within a hydrophobic pore are shown in the lower panel for the 5 (purple), 10 (red), and 15 (brown) Debye solute. The upper panel displays the corresponding position probability distributions, $P(x)$. Notably, the scale of the free energy is markedly decreased from the corresponding curves in Figure 4.2.

hydrophobic case, too, small effects in the free energy profile for the 5 D solute are amplified for larger solute dipole moments. Taken together, these effects mean that the 5 D solute shows little bias in x position for the $z = 0$ Å cut. The 10 D and 15 D solute show some localization, but in a location that can be accessed by the 5 D solute.

Previous theoretical investigations have also found state-dependent solute positions in nanoconfined systems. The key differences with the present study are the solute size, confining framework chemistry, and pore roughness. A Monte Carlo study using a smooth, spherical confining surface and a small dye model dissolved in methyl iodide or acetonitrile found that the ground-state solute preferentially resides at the interface while the the most likely position for the excited-state solute is the pore interior[73]. Subsequent nonequilibrium MD simulations of $S(t)$ for the same system found a contribution of solute diffusion to the solvation dynamics resulting from this difference in ground- and excited-state equilibrium positions[78]. These position biases are reversed from those found in this work, in which the excitation of the solute drives it to the pore interface. The difference is likely attributable to the favorable solute-pore interactions, absent in the previous study, and the solute size, which allows the present model to span several layers of varying solvent polarity. Additionally, the simple nature of the confining frameworks used in this earlier work[73, 78, 80] eliminated any effects of surface roughness and chemistry.

A state-dependent solute position was also observed in MD simulations of reverse micelles (RM).[138] Using I_2^+ and I_2^- models of solute “excited states"

of I_2, Faeder and Ladanyi showed that each excited state exhibited a distinct location preference within the RM, which they used to explain differences in the nonequilibrium behavior of the two excited-state models.[138]

Summarily, the position distribution, $P(x)$, is always a function of dipole moment for both hydrophilic and hydrophobic pores; the results are most dramatic in the hydrophilic pore. (For this reason, expensive calculations at $z = \pm 10$ Å for the hydrophobic case were not performed.) Additionally, some locations within the pore strongly attract 10 D and 15 D solutes, which implies that heterogeneity influences solute location.

4.3.1 Free Energy Decompositions

The factors that dictate the forms of the $\Delta A(x)$ curves can be explored by decomposing them into contributions from the silica pore and the solvent. Each of these contributions, in turn, can be decomposed into Lennard-Jones interactions and Coulombic interactions. In other words, $\Delta A(x) = \Delta A_{pore}(x) + \Delta A_{solv}(x)$, with $\Delta A_{pore}(x) = \Delta A_{pore,LJ}(x) + \Delta A_{pore,C}(x)$ and $\Delta A_{solv}(x) = \Delta A_{solv,LJ}(x) + \Delta A_{solv,C}(x)$.

The results of this decomposition of the free energy profile, $\Delta A(x)$, for the $z = 0$ Å cut across the hydrophilic pore are shown for the solvent in Figure 4.6. The top, middle and bottom panels show $\Delta A_{solv}(x)$ (solid lines), $\Delta A_{solv,LJ}(x)$ (dot-dashed lines), and $\Delta A_{solv,C}(x)$ (dashed lines) for the 5 D (black), 10 D (blue), and 15 D (green) solute models. The energy scale for each panel is different. Though difficult to discern due to the scaling, the shape of each $\Delta A_{solv}(x)$ curve is similar. Each curve shows a shoulder in the free energy near the pore interface, and small

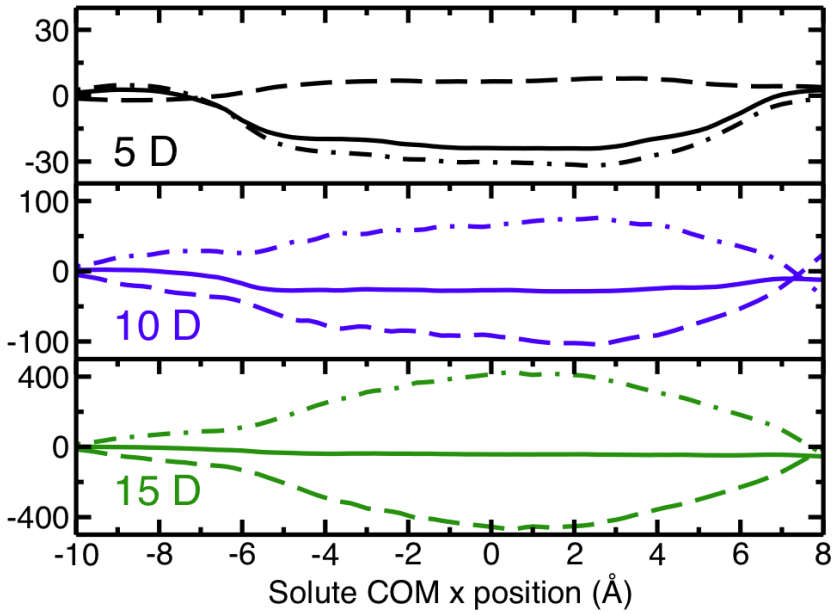

Figure 4.6: The figure shows the solvent contribution to the Helmholtz Free Energy as a function of solute COM x position within the hydrophilic pore at $z = 0$ Å for the 5 (black), 10 (blue), and 15 (green) Debye solute. Notably, the energy scale, in kJ mol^{-1}, differs for each dipole moment of the solute. The solid lines represent the total free energy contributions from the solvent, ΔA_{solv}. These are further decomposed into solvent Lennard-Jones ($\Delta A_{solv,LJ}$, dot-dashed lines) and solvent Coulombic ($\Delta A_{solve,C}$, dashed lines) contributions.

undulations are present in the pore interior. In the profile for the 5 D solute, it is evident that $\Delta A_{solv,LJ}$ contributes the shoulders near the pore interface. Elsewhere in the pore, the Lennard-Jones and Coulombic contributions are offset by a nearly constant amount, but near the interface these contributions nearly cancel. The net effect is an increase in free energy due to the solvent near the interface, which indicates that the 5 D solute is better solvated in the pore interior. For the 10 D (and less clearly, the 15 D) solute, the shoulder in the total solvent contribution to the free energy ($\Delta A_{solv}(x)$) on the right side ($x > 0$ Å) of the pore disappears. The value there becomes negative, as the Lennard-Jones and Coulombic contributions fail to cancel in this region. Thus, the 10 D and 15 D solutes are better solvated near the hydrophilic pore interface for the $z = 0$ Å cut. Interestingly, the roles of the Lennard-Jones and Coulombic contributions are reversed from their roles in the 5 D solute case. That is, the Lennard-Jones component is generally positive in the pore interior, while the Coulombic contribution is negative. It is the Lennard-Jones contribution that stabilizes the solute near the pore interface. Similarly, this result implies that electrostatic interactions pull solvent molecules toward the solute in the pore interior, where the solute access to the solvent is greatest. This will be examined further in Section 4.3.2.

Examining in Figure 4.7 the pore contribution to the free energy, $\Delta A_{pore}(x)$ (solid lines), for the $z = 0$ Å cut across the hydrophilic pore, it is clear that the steep rise in free energy away from the pore interior in *all* total free energy profiles comes from interactions with the silica pore. Moreover, this behavior can be attributed to the Lennard-Jones contribution ($\Delta A_{pore,LJ}(x)$, dot-dashed lines), indicating that

the strong repulsion comes from pushing the solute against the pore interface. Switching focus to the Coulombic contributions ($\Delta A_{pore,C}(x)$, dashed lines), it is clear that on the left side of the pore ($x < 0$ Å), the electrostatic interactions between the solute and the interface are not strong. In contrast, on the right side of the pore, the Coulombic contribution from the pore wall becomes increasingly negative with increasing dipole moment. The decreasing Coulombic energy near the interface added to the typical Lennard-Jones interaction energy result in a curve with a strong minimum near the interface. Thus, the interaction primarily responsible for the increased localization near the pore interface for increasing solute dipole moment comes from Coulombic interactions with the confining framework. As discussed in Section 4.4, this interaction with the interface has consequences beyond solute localization.

Turning attention to the same cut across the pore ($z = 0$ Å) but for the hydrophobic case, Figure 4.8 shows that interactions of the solute with the solvent are largely the same in the hydrophobic pore as they are in the hydrophilic pore. The solute is better solvated by the solvent in the pore interior, where the solvent access to the solute is maximal. It is also clear that the role that Lennard-Jones and Coulombic interactions play depends upon the solute dipole moment. As before, for the 5 D solute, the Lennard-Jones interactions with the solvent stabilize the solute. For the 15 D solute, the Coulombic interactions are stabilizing. Interestingly, the 10 D case in the hydrophobic pore appears to capture, in part, this role reversal.

The silica contribution to the solute free energy in the hydrophobic pore for $z = 0$ Å is shown in Figure 4.9. The fact that the hydrophobic pore is generated

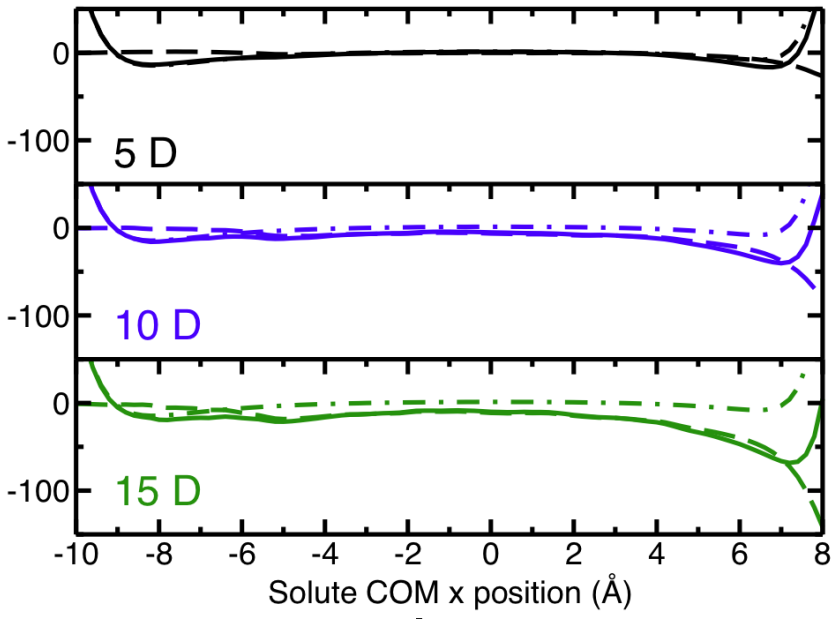

Figure 4.7: The silica contributions to the free energy are shown as a function of position is shown for the 5 (black), 10 (blue), and 15 (green) Debye solute in the hydrophilic pore. The ordinate unit of energy is kJ mol^{-1} for all three panels. In contrast to the solvent decomposition of Figure 4.6, the energy scale for each panel is the same. Similarly to Figure 4.6, the solid lines present the total contributions from the silica pore, ΔA_{pore}. These have been further decomposed into contributions from the silica Lennard-Jones interactions ($\Delta A_{pore,LJ}$, dot-dashed lines) and silica Coulombic interactions ($\Delta A_{pore,C}$, dashed lines).

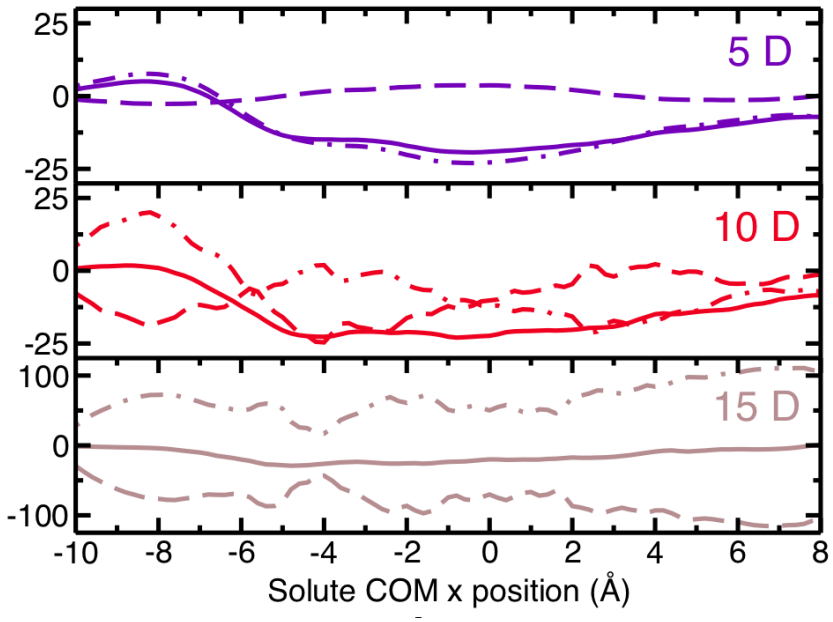

Figure 4.8: The solvent contribution to the free energy is shown as a function of position, x, within the hydrophobic pore for the 5 (purple), 10 (red), and 15 (brown) Debye solute models. As for the solvent contribution in the hydrophilic pore (Figure 4.6), the energy scale (in kJ mol^{-1}) differs for each solute dipole moment. The magnitudes, however, are different from those of hydrophilic pore case. Solid lines indicate the total solvent contribution (ΔA_{solv}), dashed lines indicate the solvent Coulombic contribution ($\Delta A_{solv,C}$), and dot-dashed lines indicate the solvent Lennard-Jones contribution ($\Delta A_{solv,LJ}$). Notably, the energies for ΔA_{solv} and $\Delta A_{solve,LJ}$ have been shifted by 400 kJ mol^{-1} for plotting purposes.

by setting the pore charges to zero is reflected in the dashed line ($\Delta A_{pore,C}$) at zero. Thus, the total contribution from the silica pore (ΔA_{pore}, solid line) and the Lennard-Jones contribution from the silica pore ($\Delta A_{pore,LJ}$, dot-dashed line) coincide. Additionally, the pore structure is unchanged, so that the 5 D (purple, top panel), 10 D (red, middle panel), and 15 D (brown, bottom panel) solute results are the same; each case is included for completeness and to facilitate comparison to other figures. The Lennard-Jones interactions are stronger on the left ($x < 0$ Å) side of the pore than the right ($x > 0$ Å) side of the pore. That is, Lennard-Jones interactions alone would favor the solute on the left side of the pore and only by a few kJ mol^{-1}.

For $z = 0$ Å, it is clear that Coulombic interactions with a heterogeneous silica surface control solute position within the pore. Free energy decompositions for the $z = -10$ Å and $z = +10$ Å cuts across the hydrophilic pore support this (data not shown). The right ($x > 0$ Å) side of the pore for the $z = +10$ Å cut shows a decrease in $\Delta A_{pore,C}(x)$ near the silica interface, although this decrease is not as pronounced as the $z = 0$ Å case. For the $z = -10$ Å cut, the Coulombic contributions from the silica pore are weak. The result is that both sides of the pore show profiles similar to the left ($x < 0$ Å) side of the $z = 0$ Å profile. These effects show up clearly in the position probability distributions, $P(x)$ in the top panels of Figures 4.2, 4.3, and 4.4.

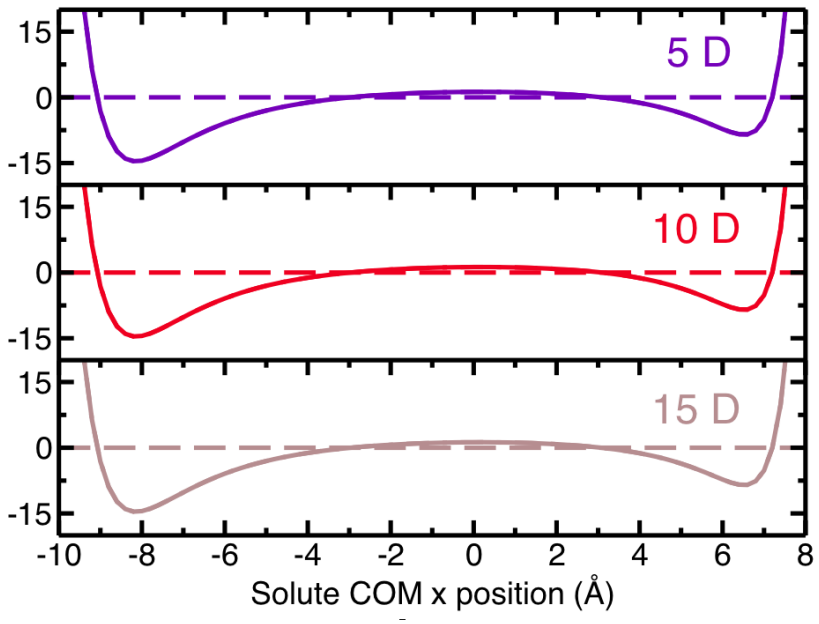

Figure 4.9: The hydrophobic pore silica contributions to the free energy as a function of solute position, x, for 5 (purple), 10 (red), and 15 (brown) Debye solute molecules. The ordinate axes indicating energy (in kJ mol^{-1}) are scaled the same for all dipole moments, in contrast to the solvent contributions in Figure 4.8. Because the Coulombic contributions ($\Delta A_{pore,C}$, dashed lines) are zero, the dot-dashed lines indicating the silica Lennard-Jones contributions ($\Delta A_{pore,LJ}$) and solid lines indicating the total (ΔA_{pore}) are coincident.

4.3.2 Structural Relationships

To explain the shapes of the decomposed curves, it is instructive to examine structural relationships among the silica pore, the solvent, and the solute.

The pair distribution function for the solute COM and solvent COM is shown in Figure 4.10. The function is shown for the 5 D (black), 10 D (blue), and 15 D (green) solute in bulk ethanol (top panel), in the hydrophilic pore (middle panel), and in the hydrophobic pore (bottom panel). The abscissae start at $R_{solute-solvent} =$ 3.0 Å, reflecting the large size of the solute molecule. In each case, increasing the solute dipole moment decreases the solute-solvent separation. The $g(R)$ curves for hydrophilic and hydrophobic confinement agree well with one another, and in both confined systems, the solvent tends to be closer to the solute than for the bulk case. Clearly, confinement alters the degree to which the solute and solvent interact, as the curves $g(R)$ for higher solute dipole moments in confined systems begin at shorter distances than those of the corresponding bulk cases. Importantly, because the $g(R)$ calculation in the confined systems was performed with the solute in the center of the pore, these results do not reflect directly how solvent organization about the solute might change near the pore interface.

From Figure 4.2, it is clear that the pore influences the behavior of the solute. The TDF signal, which comes from the solute, may be influenced by the solute's location in the pore. The anisotropy imposed by the confining framework has clear consequences for the behavior of the solute in the confining framework. It is also important to understand the consequences of confinement for the solvent, particularly because the TDF signal is largely attributed to solvent dynamics.

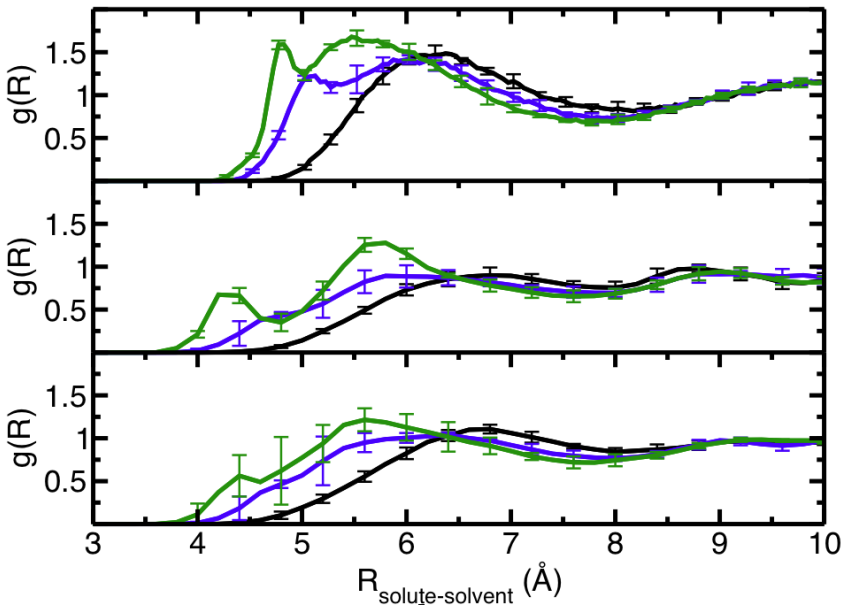

Figure 4.10: The pair distribution function between the solute center of mass (COM) and solvent COM is shown for bulk (top panel), the hydrophilic pore (middle panel), and the hydrophobic pore (bottom panel.) Each panel shows curves for the 5 (black), 10 (blue), and 15 (green) Debye solute.

Specifically, solvent dynamics are slowed near the confining interface; this is supported by both theoretical and experimental observations.

Previous theoretical investigations of solvents in hydrophobic confinement show solvent layering to be an important phenomenon when describing dynamics in confined systems [73,80]. To investigate solvent layering within the hydrophobic and hydrophilic pores employed here, solvent density profiles were constructed along the same x direction ($y = 0$ Å) for the cut $z = 0$ Å, where the influence of the pore on the solute appears to be strongest. A 4×4 Å^2 box in the $y-z$ plane was constructed and extended along the x direction. Solvent density profiles along the x direction were constructed by histogramming the solvent sites falling within the box. (Notably, solvent perturbations by the solute were avoided by using the 5 D system with the solute in the $z = +10$ Å plane. This approach is reasonable, given the solute-solvent pair distributions in Figure 4.10.) The results of this calculation are presented in the lower panel of Figure 4.11. For comparison, the upper panel shows the (total) solute free energy profiles with definite local maxima highlighted by arrows. In the bottom panel, the ethanol COM site shows large peaks near the pore interface. Moving away from the pore interface, the COM density peaks are broadened and diminished in intensity. A very broad, low-intensity distribution sits over the center of the pore. The COM density profile is roughly symmetric about the center of the pore. Decomposing the solvent density profile into atomic and group sites provides a very different picture. The density profiles of the methylene (purple) and methyl (brown) groups are similar to that of the COM site. The density profiles for hydrogen (red) and oxygen (blue) are remarkably different

for the two sides of the pore. On the left ($x < 0$ Å) side, any maximum is likely a consequence of the methylene and methyl packing against the interface; the hydrogen and oxygen maxima on the left side of the pore point toward the pore interior. On the right ($x > 0$ Å) side of the pore, the density profile for hydrogen is very sharply peaked and is positioned closer to the pore interface than the nearest methylene and methyl peaks. The peak in the oxygen density is also prominent, but less sharply distributed than that of hydrogen. Additionally, it resides between the methylene/methyl and hydrogen peaks. This suggests that the solvent on the right side of the pore is both strongly associated with and strongly oriented by the silica interface.

Several factors may contribute to the weaker correspondence between solvent layering and free energy seen here compared to previous reports. In those studies, the solute models were comparable in size to the solvent, leading to solutes lying within a solvent layer or spanning across two layers[73, 78, 80]. Here, the influence of the solvent on the solute free energy is complicated by the fact that the solute spans several solvent layers of differing effective polarity. In addition, the heterogeneous chemistry (placement of silanol groups) and roughness of the pore surface also influences the solvent layering, as discussed below. Finally, the correlation between solvent layering and solute free energy appears to be stronger for linear solvents (*e.g.*, CH_3I, CH_3CN) than for nonlinear solvents like methanol or ethanol,[80] presumably due to packing effects.

Particularly strong evidence supporting the idea that the two sides of the pore present different environments comes from probing the local pore environments

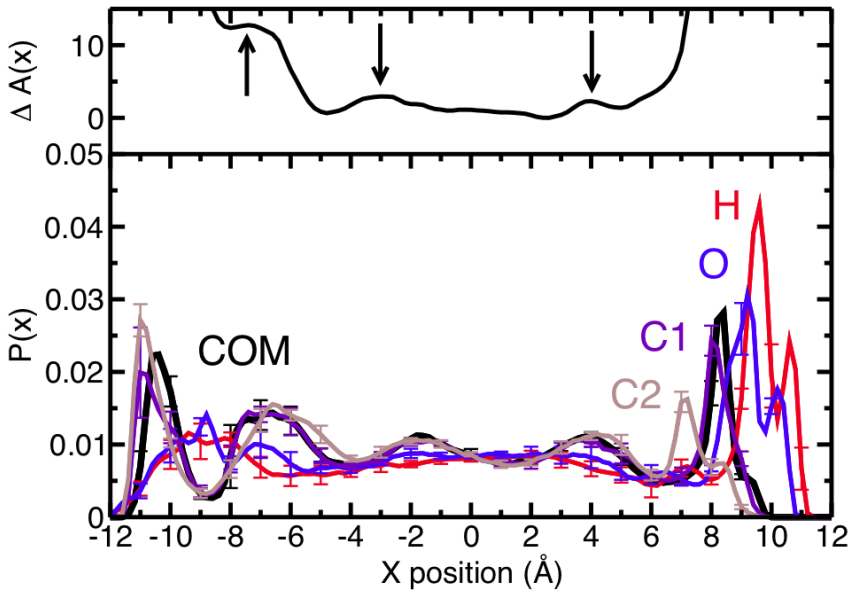

Figure 4.11: Solvent density profiles along the $z = 0$ Å cut across the hydrophilic pore are shown in the lower panel. Ethanol COM (black), hydrogen (red), oxygen (blue), methylene (purple), and methyl (brown) densities are provided. The upper panel shows the solvent contribution to the free energy profile. Arrows indicate where the free energy local minima occur in the total free energy profile.

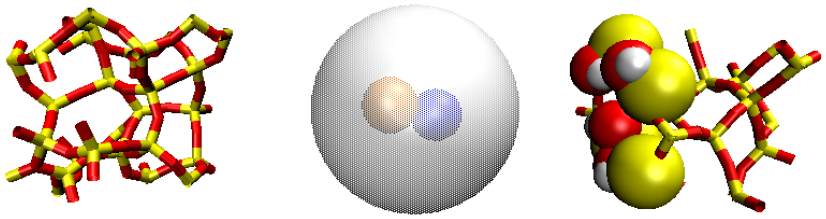

Figure 4.12: The figure shows the left ($x < 0$ Å) and right ($x > 0$ Å) silica interfaces for the $z = 0$ Å cut across the pore. The silica framework is shown in licorice representaiton, while silanol groups are shown in space-filling representation. Silicon atoms are shown in yellow, oxygen atoms are red, and hydrogens atoms are white. The solute is included in the center of the pore and is shown as a large, translucent sphere with the *P* and *N* sites enclosed. Clearly, the two sides of the pore present distinct chemical environments to the solute.

directly. Figure 4.12 shows the left ($x < 0$ Å) and right ($x > 0$ Å) pore interfacial regions for the $z = 0$ Å cut across the pore. The model solute is shown in the center, and the solvent has been eliminated. The silicon (yellow) and oxygen (red) atoms of the silica framework are shown in licorice representation. The silicon, oxygen and hydrogen (white) atoms comprising silanol groups are shown in space-filling representation. Clearly, the two sides of the pore present different environments to both solute and solvent. The left side offers only a small cavity composed of the framework. The right side provides several silanol groups for hydrogen bonding. Thus the results for the solute position probability distributions, $P(x)$, of Figure 4.2, the pore electrostatic contribution to the free energy, $\Delta A_{pore,C}(x)$, of Figure 4.7, and the solvent density profiles of Figure 4.11 might be rationalized by considering the differential silanol coverage with the pore, *i.e.*, pore heterogeneity.

The same solvent density calculation performed for the hydrophobic pore for the same $z = 0$ Å cut shows density profiles that are approximately symmetric

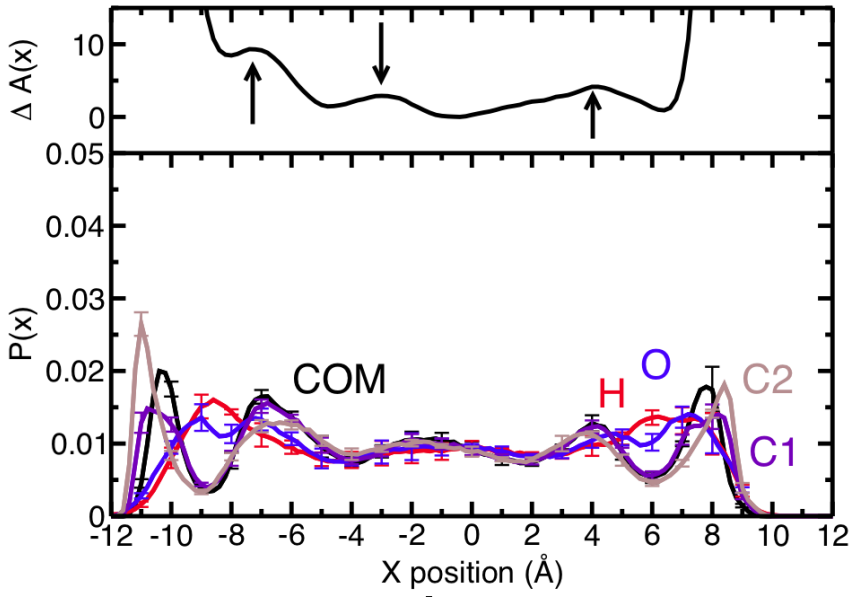

Figure 4.13: Solvent density profiles are shown in the bottom panel for $z = 0$ Å in the hydrophobic pore. Color coding of the bottom panel curves and the explanation of the upper panel are as in Figure 4.11

.

for COM, hydrogen, oxygen, methylene, and methyl sites. Moreover, the profiles resemble those found on the left side of the hydrophilic pore. That is, the bulky methylene and methyl groups (and hence COM sites) pack strongly against the silica interface. The oxygen and hydrogen atoms point inward. Moving toward the pore interior, the distributions of methylene and methyl groups become broader but remain distinct. This result might also be anticipated by considering Figure 4.12. When the charges for all pore atoms are identically zero, the difference between interaction with the pore interface on the left and right sides reduces to the differences in the left and right sides of Figure 4.9.

The spacing between maxima in the COM profile in the hydrophilic pore is $\approx 4-5$ Å. The spacing between peaks in the free energy in the hydrophilic pore is $\approx 3.5-4$ Å. Similarly, the spacing between maxima in the COM profile in the hydrophobic pore is $\approx 4-5$ Å, and the spacing between peaks in the free energy in the hydrophobic pore is $\approx 3-5$ Å. Such a result supports the notion that the undulations in the free energy profiles are the result of solvent packing within the pore. However, this evidence is suggestive but not conclusive. The packing of solvent near the pore interface, however, in both the hydrophobic and hydrophilic pore (left sides) correlates well with the appearance of shoulders in the free energy profiles. The shoulders in the $\Delta A(x)$ profiles can then be interpreted as the energy required to displace the solvent molecules that are strongly associated with the interface.

4.4 Simulated Equilibrium Spectra

The results presented above show that the solute position within the pore is clearly a function of its charge distribution. Additionally, strong biasing of the solute position is a consequence of pore heterogeneity, and specifically, the Coulombic interaction between interfacial silanol groups and the solute. Thus, the solute experiences a different electric field at different positions within the pore. Because spectral properties depend upon the charge distribution of the solute molecule, it is reasonable to suspect that spectral properties—fluorescence peak position, for example—will also be a function of the solute position within the pore. This is

requirement two in the solute diffusion hypothesis—that the solute position within a pore controls the fluorescence energy, and its testing is of critical importance in determining if motions of the solute molecule can contribute to TDF spectra.

Equilibrium spectra can be calculated from the MD simulation trajectories. Additionally, whereas solute position has no meaning within the context of a bulk solution, useful conclusions can be drawn from comparisons between spectra recorded in bulk and confined solutions. To simulate bulk spectra, a simulation box of 500 OPLS-UA ethanol molecules was constructed as previously described in Section 2.1. Five ethanol molecules were removed within the center of the box to accommodate the model solute described below, leaving 495 ethanol molecules.

To investigate the possibility that electronic spectra depend upon the position of the solute within the pore, individual spectra were calculated for each solute COM x position according to

$$I_{abs}(\Delta E;x) = \langle \delta(E_{ex} - E_{gr} - \Delta E) \rangle_{gr,x} \tag{4.5}$$

$$I_{fl}(\Delta E;x) = \langle \delta(E_{ex} - E_{gr} - \Delta E) \rangle_{ex,x} \tag{4.6}$$

In Equation 4.5, the solute at position x in the pore is in its ground state, and the solvent is equilibrated to it. In the Franck-Condon approximation, the solute electronic redistribution is assumed to occur instantaneously with respect to the nuclear coordinates, so that neither solute nor solvent nuclear positions are affected by the new solute charge distribution at the time of excitation. Then, using the solute and solvent coordinates at that instant, the ground-state energy is calculated

using Coulomb's law (2.2), the ground-state solute charges, and the solvent charges. For the same system configuration, the excited state energy is calculated using the excited state solute charges and the solvent charges. The absorption energy is taken as the difference in these energies, $E_{ex} - E_{gr}$. As is common, in Equation 4.5, the delta function for practical purposes is assumed to have a small, finite width, and the absorption energy is histogrammed. This calculation is performed for many ground state solvent configurations with fixed solute position x, and these results are averaged, as indicated by the subscripted brackets $\langle - \rangle_{gr,x}$. The full result is a distribution of excitation energies or absorption spectrum. The fluorescence spectrum is calculated in a similar way in Equation 4.6. Importantly, the averaged subscript in Equation 4.6 indicates that the solvent is equilibrated to the solute excited state charge distribution.

These spectra for the solute confined in hydrophilic and hydrophobic pores are calculated for each solute position x. The total absorption or fluorescence spectrum is then the total of each position-dependent spectrum weighted by the probability that the solute is in that particular position x within the pore. This is described mathematically by the equations

$$I_{abs}^{tot}(\Delta E) = \int \mathrm{d}x \, P_{gr}(x) \, I_{abs}(\Delta E; x), \tag{4.7}$$

$$I_{fl}^{tot}(\Delta E) = \int \mathrm{d}x \, P_{ex}(x) \, I_{fl}(\Delta E; x). \tag{4.8}$$

Obviously, the absorption and fluorescence spectra for the bulk system can be obtained simply using Equations 4.5 and 4.6, and no subscript for x is necessary.

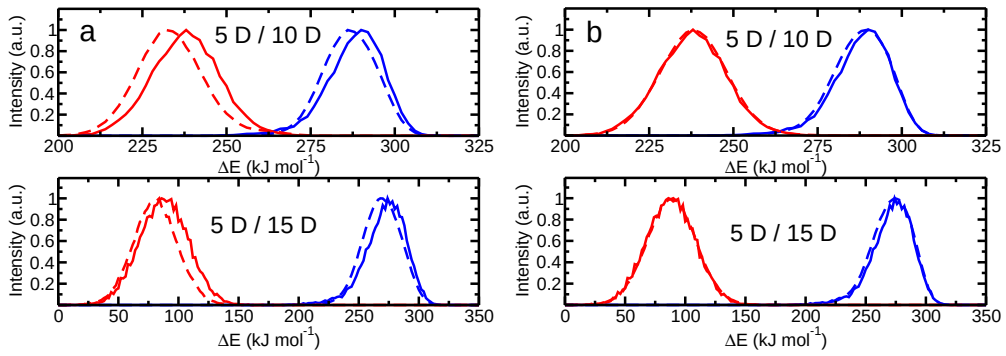

Figure 4.14: (a) Absorption (blue) and fluorescence (red) spectra are shown for the solute dissolved in ethanol in bulk (solid lines) and in hydrophilic confinement (dashed lines). The upper panel shows these spectra for the 5 D / 10 D ground state / excited state system, while in the lower panel, the excited state is 15 D. The energy scale of the abscissa is different for the two panels. (b) Corresponding spectra are shown for solutes confined in the hydrophobic pore.

The total spectra are considered first. Figure 4.14a shows that confinement (dashed lines) changes the bulk (solid lines) absorption (blue) and fluorescence (red) spectra for both the 5 D / 10 D (top panel) and the 5 D / 15 D (bottom panel) solute systems. The energy scale of the abscissa in each panel is different. The simple solute model captures the well-known effect of red-shifting the fluorescence energy upon nanoconfinement for both the 5 D / 10 D and the 5 D / 15 D solute systems. Experimentally, blue-shifted absorption spectra are also sometimes observed [].

The calculated full absorption and fluorescence spectra for the 5 D / 10 D and 5 D / 15 D solute systems in the hydrophobic pore are shown in Figure 4.14b. Again, the energy scale differs for the 5 D / 10 D system and the 5 D / 15 D system. In each case, the bulk and confined spectra overlay well, indicating no significant shifting of the spectra. Together, these results indicate that only confinement in the

hydrophilic pore results in significant shifting of the absorption and fluorescence spectra. A more quantitative approach can be taken by calculating for each curve the mean spectral position given by Equation 4.9.

$$\langle \Delta E \rangle = \int \mathrm{d}x \int \mathrm{d}\Delta E \; \Delta I(\Delta E; x) \, P(x) \, \Delta E \tag{4.9}$$

Spectral shifts (in both kJ mol^{-1} and nm) calculated this way are provided in Table 4.3. The results indicate that results for the 5 D / 15 D system, the fluorescence

Table 4.3: Mean spectral positions*

5 D / 10 D system								
	bulk		-philic		shift	-phobic		shift
	$\langle \Delta E \rangle$	λ	$\langle \Delta E \rangle$	λ	$\Delta\langle \Delta E \rangle$	$\langle \Delta E \rangle$	λ	$\Delta\langle \Delta E \rangle$
abs.	288.2_2	415	286.6_1	417	-1.6_2	287.9_1	416	-0.3_2
flu.	237.9_2	503	233.5_1	512	-4.4_3	238.1_2	502	0.2_3
S. S.†	50.3_5	88	53.1_3	95	—	49.8_5	86	—
5 D / 15 D system								
	bulk		-philic		shift	-phobic		shift
	$\langle \Delta E \rangle$	λ	$\langle \Delta E \rangle$	λ	$\Delta\langle \Delta E \rangle$	$\langle \Delta E \rangle$	λ	$\Delta\langle \Delta E \rangle$
abs.	273.0_3	438	269.4_2	444	-2.6_5	272.1_2	440	-0.9_5
flu.	87.5_6	1367	80.9_6	1479	-6.6_{12}	88.6_5	1350	1.1_{11}
S. S.	185.5_{10}	929	188.5_9	1035	—	183.5_8	910	—

*ΔE is in kJ mol^{-1}, λ in nm. "Shift" indicates shift from bulk upon confinement, $\Delta\langle \Delta E \rangle = \langle \Delta E \rangle_{conf} - \langle \Delta E \rangle_{bulk}$. Subscripts indicate uncertainty in the last digit. Quantities are based on spectra calculated along the $z = 0$ Å cut across the pore.
† S. S. indicates the Stokes shift.

wavelengths are in the IR region of the spectrum. While this does not correspond to experimental fluorescence wavelengths, the 5 D / 15 D system may be useful in evaluating trends. The results in Table 4.3 indicate that in hydrophilic confinement, the Stokes shift increases above that of the bulk system for both the 5 D / 10 D and

the 5 D / 15 D solute system. Interestingly, for both cases the shift is approximately 3 kJ mol^{-1}.

4.4.1 Spectral Decompositions

From Figure 4.14, it is clear that hydrophilic confinement changes the spectra of the solute. Spectra as a function of solute position in the pore must now be examined. Additionally, it is useful to know if the results for the $z = 0$ Å cut are general or unique. To what extent the solute position in the pore influences the fluorescence energy can be seen by examining the mean fluorescence energy as a function of position, $\langle \Delta E_{fl} \rangle (x)$, which is calculated as

$$\langle \Delta E_{fl} \rangle (x) = \int \Delta E \, I_{fl}(\Delta E;\, x) \, \mathrm{d}\Delta E. \tag{4.10}$$

This has been calculated for the hydrophilic pore (solid lines) for the cuts along $z = -10$ Å (black), $z = 0$ Å (blue), and $z = +10$ Å (green) and for the hydrophobic pore (dashed line) along the cut $z = 0$ Å. The results are presented in Figure 4.15. All profiles are qualitatively flat from the left ($x < 0$ Å) side of the pore through the pore interior, indicating little to no movement of the spectral peak as a function of solute position. Near the right ($x > 0$ Å) side of the pore, however, the mean fluorescence energy redshifts for the solute in the hydrophilic pore. In the hydrophobic system, no redshift is observed. To partly address if these shifts might manifest in the TDF signal, the most probable solute positions have been indicated with arrows for ground (g) and excited (e) solutes. A change in fluorescence signal

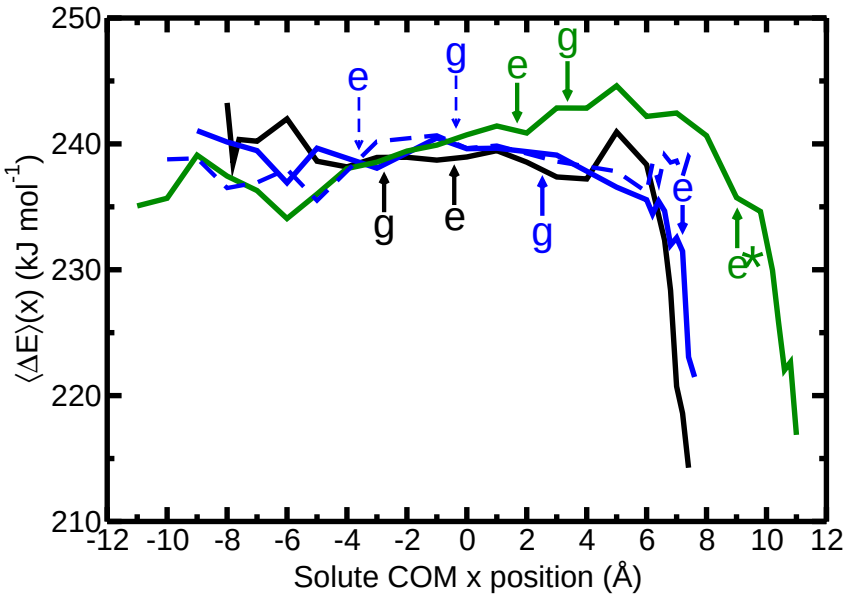

Figure 4.15: Mean fluorescence energy as a function of solute position, $\langle \Delta E_{fl} \rangle (x)$, is shown for the 5 D / 10 D solute system in the hydrophilic (solid lines) and hydrophobic (dashed lines) pore for the cuts $z = -10$ Å (black), $z = 0$ Å (blue), and $z = +10$ Å (green). The most likely position for the solute in its ground (g) or excited (e) state is indicated by arrows of the corresponding line type and color. Notably, the excited state solute can sample regions near the pore interface for the cut $z = +10$ Å, as indicated by e^*.

in the $z = 0$ Å cut across the hydrophilic pore is anticipated, as the excited state solute will be in a location where the fluorescence energy is redshifted. Similarly, the excited state solute for the $z = +10$ Å cut can sample the region near the interface (indicated by e^*) where some redshifting of the fluorescence energy occurs. (The excited state also samples regions toward the interior of the pore, as shown in Figure 4.15.)

To what extent this is a property of the 5 D / 10 D solute system, and to what extent absorption spectra are also altered for the model solutes employed

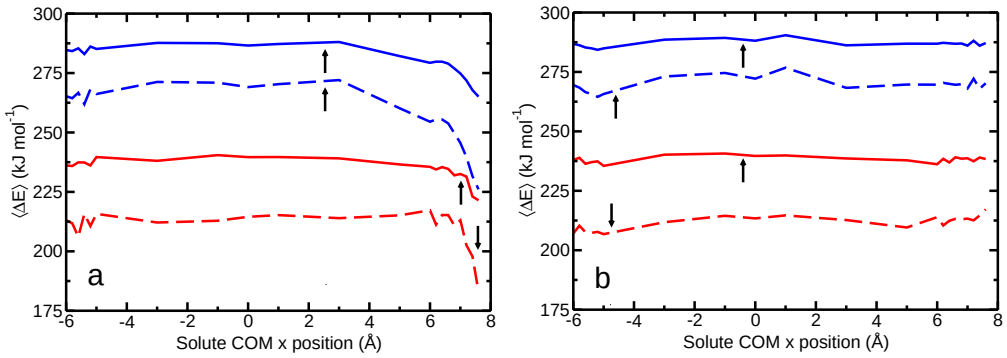

Figure 4.16: The figure shows the mean absorption (blue) and fluorescence (red) energies as a function of the solute position within the hydrophilic pore for both the 5 D / 10 D solute system (solid lines) and 5 D / 15 D solute system (dashed lines). Arrows indicate the global maxima in the respective position probability distributions in Figure 4.2 for reference.

here is addressed in Figure 4.16. Figure 4.16a shows both absorption (blue) and fluorescence (red) for the 5 D / 10 D system for the $z = 0$ Å cut through the hydrophilic pore. The effect of increasing the excited state dipole to 15 D (dashed lines) results in a general shift to lower energies than are seen for the 10 D solute. Additionally, the induced shift near the pore interface is more dramatic. The profiles for the absorption curves (blue) indicate that while changes to the spectrum may occur near the pore interface for both the 10 D and 15 D excited state solutes , the most probable position for the solute is in the pore interior in both cases. Accordingly, the shift in the absorption spectrum near the interface is not anticipated to contribute substantially to the total observed spectrum. In the hydrophobic pore, the mean spectral position is relatively insensitive to the solute location within the pore, as seen by the mostly flat curves in Figure 4.16b. The

dominant feature is the general shift that accompanies the change in solute dipole moment.

The spectral width—and specifically the full-width-at-half-maximum (FWHM)—is of particular interest, as it is frequently used to provide indirect information about solute environment through inhomogeneous line broadening. Figure 4.17 shows the results of calculating the FWHM for the 5 D / 10 D solute system (solid lines) and 5 D / 15 D solute system (dashed lines) for both absorption (blue) and fluorescence (red) spectra for the $z = 0$ Å cut across the pore. The picture is qualitatively similar to the results for the mean spectral position, in that dramatic changes occur near the pore interface in the hydrophilic pore (Figure 4.17a), while the changes to spectral width near the pore interface in the hydrophobic pore (Figure 4.17b) are absent. On the right side ($x > 0$ Å) of the hydrophilic pore, the FWHM is decreased, relative to those for spectra for solutes in the pore interior. That is, the spectra for solutes near the interface are narrowed, which, within the context of inhomogeneous broadening, suggests decreased solvent fluctuations and perhaps decreased solvent access near the pore interface. However, additional study is required to confirm this.

The collective results suggest that spectra for solutes in the pore interior are generally similar, while solutes near the interface show altered spectral properties. Accordingly, to enhance sampling while investigating in more detail the ways in which spectra depend on solute position, the spectra for solutes residing near the left ($x < 0$ Å) pore and also in the pore interior can be averaged. The spectra for solute positions approaching the right ($x > 0$ Å) side of the pore are averaged over

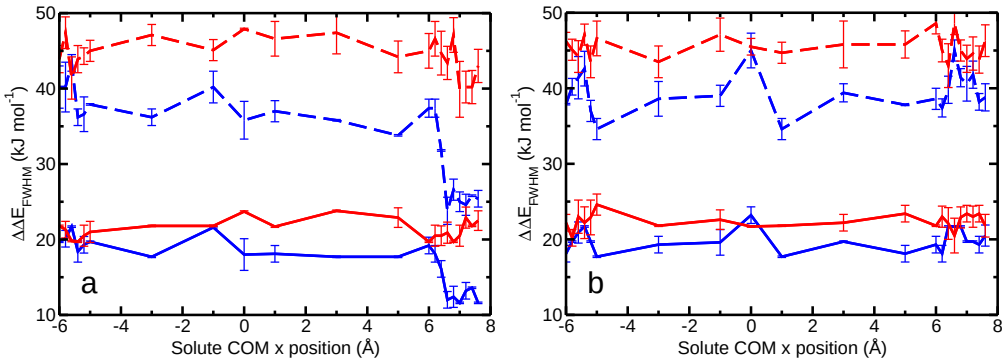

Figure 4.17: The full width at half maximum is presented for absorption (blue) and fluorescence (red) spectra as a function of solute position, x, across the hydrophilic pore for both the 5 D / 10 D solute system (solid line) and the 5 D / 15 D solute system (dashed line).

small intervals in x. The results for position-dependent spectra calculated this way are presented for the 5 D / 10 D solute system in the hydrophilic pore (Figure 4.18a) and hydrophobic pore (Figure 4.18b).

The resulting spectra in the hydrophobic pore overlap with one another. This result indicates that the solvent does not appreciably change the spectra. It also supports the notion that averaging over regions in the pore where the mean spectral energy is mostly constant is not problematic (*i.e.*, does not lead to artifacts in the averaged spectra). The results for the hydrophilic pore (Figure 4.18a) indicate that stronger redshifting occurs as the solute approaches the cluster of silanol groups on the right ($x > 0$ Å) side of the pore. The solid lines represent the spectra averaged over the pore left side and pore interior, from -6 to $+5$ Å for the $z = 0$ Å cut. The long dashed lines represent spectra for the solute at $+6.4$ Å, the short-dashed lines represent spectra for the solute at $+7.0$ Å, and the dot-dashed lines

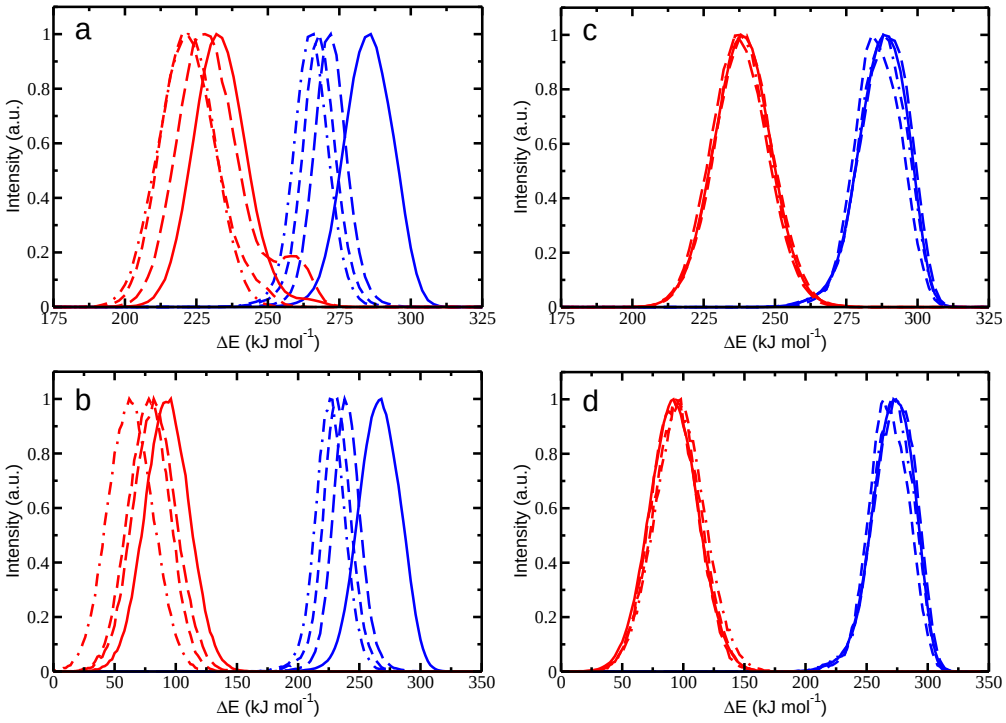

Figure 4.18: (a) Absorption (blue) and fluorescence (red) spectra are shown for the 5 D / 10 D solute system dissolved in the hydrophilic pore. Each spectrum is the normalized average of spectra for the solute at a range of positions within the pore. Note that both the absorption and fluorescence red shift as the solute approaches the pore wall. (b) Spectra for the 5 D / 10 D solute system dissolved in the hydrophobic pore show little to no shift. (c) Absorption and fluorescence spectra are shown for the 5 D / 15 D solute system in the hydrophilic pore. The abscissa scale has been changed to reflect the lower energies contributed by the 15 D solute. (d) Spectra for the 5 D / 15 D solute system in the the hydrophobic pore also exhibit little to no shift.

represent spectra for the solute at $+7.6$ Å. Interestingly, new features can be seen that are not observed in measures such as the mean spectral energy or the full-width-at-half-maximum, such as the blue-shifted shoulders in some fluorescence spectra.

The same calculations have been performed for the 5 D / 15 D solute system. The results for the hydrophilic pore are presented in Figure 4.18c, and those for the hydrophobic pore are presented in Figure 4.18d. These results are similar to the 5 D / 10 D case, although, as anticipated, changes to the spectra are amplified for the greater difference in dipole moment, $\Delta\mu = \mu_{ex} - \mu_{gr}$.

4.5 Solute Equilibrium Properties in Confinement

The equilibrium simulations presented in this Chapter indicate that the solute position in a confining framework can be a function of its charge distribution, as shown in Section 4.3. The spectral properties—fluorescence energy, absorption energy, and spectral width—associated with the solute are, in turn, a function of the solute position in hydrophilic (but not hydrophobic) pores, as shown in Section 4.4. Thus, requirements 1 and 2 are satisfied for the model solute in the hydrophilic pore. Additionally, it was shown that the satisfaction of these requirements is associated with specific chemistry at the pore interface, as indicated in Section 4.3.2.

Investigation of the extent to which the solute contributions are observable in the TDF spectrum requires non-equilibrium simulations. If the results from equilibrium

simulations presented in this Chapter are any indication of the challenges inherent in proper sampling in these systems, non-equilibrium studies will likely require alternative approaches. The initial results from non-equilibrium simulations and the development of a number of models aimed at improving physical understanding together constitute the bulk of the next Chapter.

Chapter 5

Non-Equilibrium Studies of Confined Systems

The emergent timescales observed in the time-dependent fluorescence (TDF) spectra of nanoconfined systems may originate with solute motions within the confining framework. As outlined in Section 4.2, this requires that the system satisfies three properties. First, the solute position must be a function of the charge distribution of the solute, and, second, the fluorescence energy must in turn be a function of the solute position within the confining framework. Using equilibrium molecular dynamics (MD) simulations and a model Stockmayer solute, it was shown in Chapter 4 that the solute position is a function of its charge distribution in both hydrophilic and hydrophobic confinement. However, only for confinement in a hydrophilic pore is the fluorescence a function of solute position. The third required property is that the contribution to the time-dependent fluorescence spectrum must be experimentally observable—that is, it must occur on an experimentally accessible timescale with measurable amplitude. To address this third requirement, non-equilibrium molecular dynamics (NEMD) simulations must be employed.

The results in Chapter 4 also indicate that solute position biasing and spectral properties within the pore depend strongly on surface chemistry. The importance of molecular-level effects suggests that properties of both the confining framework and solute molecule may affect the TDF signal upon nanoconfinement of the solution. Ideally, combinations of confining framework and solute molecule would be systematically tested to determine which effects are important in changing the spectrum. For example, are changes in the spectrum observed for the Stockmayer solute confined in an atomically smooth cylinder? Clearly, changes to the spectrum are observed when the solute is near a cluster of silanol groups in a silica pore. Do changes to the spectrum grow in linearly with the number of clustered silanol groups? How does the arrangement of silanol groups alter spectral properties? Similarly, hydrogen bonding was observed to be important. Does a change in spectral signature occur as a consequence of the specific chemistry of the dye molecule? For example, does the TDF signal change when a silanol group donates a hydrogen bond to a solute carbonyl group *vs.* a nitro group? Such questions are of direct chemical relevance, particularly in applications of nanoconfinement in separations, sensing, and catalysis. Addressing these questions requires the development and systematic testing of several models for both the confining framework and solute molecule.

The first part of this Chapter is dedicated to nonequilibrium simulations of time-dependent fluorescence for the Stockmayer solute. The solute biasing and spectral changes described in the equilibrium simulations of Chapter 4 are reestablished for the NEMD simulations, and TDF spectra are calculated and interpreted.

The second part of this Chapter is dedicated to the development of models for identification and quantification of molecular-level effects associated with TDF signals in nanoconfined systems.

5.1 Non-equilibrium Simulation Methods

To determine if the solute movement and spectral signatures occur as predicted by equilibrium simulations, the same confined system described in Section 4.1 was treated using non-equilibrium molecular dynamics (NEMD). To generate initial conditions for NEMD trajectories, an equilibrium trajectory for the 5 D solute was equilibrated for 500 ps and followed by a 60 ns collection phase. Configurations, velocities, and forces were recorded every 100 fs. From this output, 4000 starting conditions were collected at evenly spaced time intervals of 1 ps (*i.e.*, every tenth configuration was used from the initial 4 ns of the 60 ns equilibrium trajectory). Temperature and long-range electrostatics were handled as before (see Section 4.1).

The charge distribution for the solute was switched to that of the excited state (10 D for the Stockmayer solute) in each of the 4000 prepared systems, which were equilibrated in the ground state. Thus, time-dependent quantities include effects from solvent reorganization in response to the new excited state charge distribution. For each system, a 200 ps trajectory was collected with sampling every 0.5 ps for a total of 401 configurations (including time t_0). Time-dependent analyses were therefore limited to 200 ps.

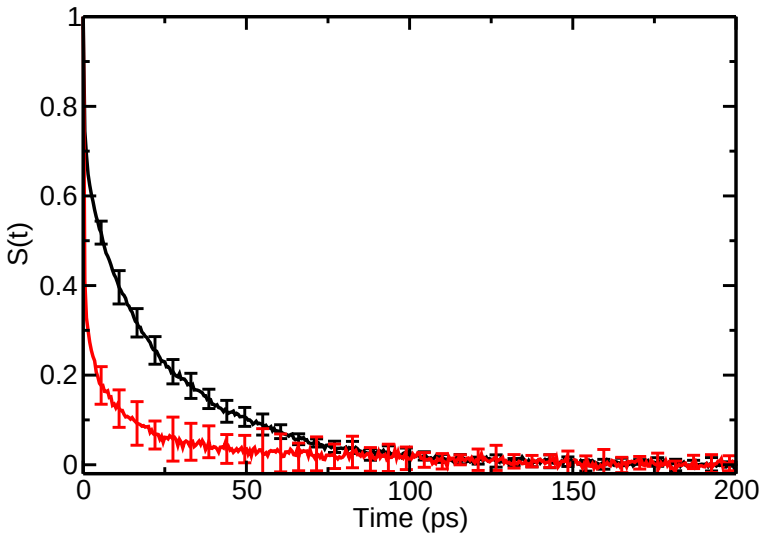

Figure 5.1: Time-dependent fluorescence signal, $S(t)$, for the Stockmayer solute (black) and coumarin 153 (red) dissolved in ethanol and confined in the hydrophilic pore.

5.2 Time-Dependent Fluorescence Signal

The function $S(t)$ is discussed in Section 1.3 and calculated according to Equation 1.10. The decay of $S(t)$ is reflective of the dynamics of the surrounding solvent. Figure 5.1 shows $S(t)$ for the Stockmayer solute (black curve), and the function is well-fit by a tri-exponential function. The resulting amplitudes and timescales for the Stockmayer solute, as well as the faster decaying coumarin 153 molecule (c153) that is discussed below in Section 5.4.1, are provided in Table 5.1.

It is also interesting to compare the Stockmayer and c153 TDF signals. From Table 5.1, the fast decay of the c153 dye occurs with twice the amplitude of

Table 5.1: TDF timescales (in ps) for Stockmayer and coumarin 153 solutes in ≈ 2.4 nm diameter silica pores.

Solute	A_1	τ_1	A_2	τ_2	A_3	τ_3
Stockmayer	0.30	0.35	0.21	7.8	0.49	31.4
Coumarin 153	0.67	0.27	0.24	7.0	0.09	53.1

the corresponding timescale for the Stockmayer solute, and their intermediate timescales are approximately the same. The long-time decay for c153 is slightly less than twice as fast as that for the Stockmayer solute. However, the amplitude associated with it is about 5 times smaller than that for the Stockmayer solute. The amplitude for the short time component may have a simple explanation. The roughly spherical nature of the Stockmayer solute means that the volume to surface area ratio is small. Accordingly, for this volume—similar to the volume of the atomistic coumarin 153 dye—there are a minimal number of solvent molecules participating in the solvation response. There are correspondingly more solvent molecules distributed around the c153 molecule, which has a larger surface area. This may partly explain the larger short-time decay associated with the atomistic dye molecule. Similarly, if the long timescale is interpreted as reorientational motion of the surrounding solvent, the flat nature of the atomistic dye may lead to slower timescales with small amplitude due to solvent packing effects against the dye. Such packing effects would be smaller for the Stockmayer solute. Additionally, specific solvent-solute interactions, which are absent in the Stockmayer solute, may play a role in the differential solvation response. Such hypotheses might be better investigated using a series of solute models, in which the effects just described "grow in" over the series of molecules. Such a series is described in Section 5.4.

First, the extent to which requirements 1 and 2 of the solute diffusion hypothesis (Section 4.2) are satisfied in NEMD simulations should be investigated. Accordingly, the following Section is devoted to examining solute positions within the pore and the position-dependence of the fluorescence energy for both the Stockmayer solute and the model c153 dye.

5.3 Non-equilibrium Solute Positions and Spectra

Results in Chapter 4 indicate that the solute position in a hydrophilic silica nanopore is a function of its charge distribution. Additionally, the spectral characteristics (including fluorescence wavelength) are, in turn, a function of the solute position. This was demonstrated using equilibrium simulations along several "cuts" across the pore. That is, the solute was studied along a single coordinate (arbitrarily chosen as x), and this was repeated for several positions along the pore axis (in z). Using average forces on the solute at a series of positions in the pore, the free energy profiles and associated position probability distributions were constructed. While this thermodynamic approach can be used to determine equilibrium properties within the pore—for example, implied movement upon excitation—it cannot address the timescales on which such motions occur. Because the timescales are the key result in TDF measurements, a non-equilibrium approach must be taken. Before examining the TDF spectra in detail, however, it is important to determine the extent to which requirements 1 and 2 are satisfied in the NEMD simulations.

5.3.1 Solute Position within the Pore

While the excitation-driven movement of the solute within the pore can be quantified in several ways, a particularly instructive way is to examine the time-dependent displacement of the solute relative to the pore interface, as implied by the results in Chapter 4. In each of four thousand 200-ps NEMD simulations, the minimum distance to the pore is determined at each time. To address periodicity in z when determining the nearest pore atom, replicas in the $-z$ and $+z$ direction were constructed. To save calculation time, the periodic images were only considered when the solute z position in the primary image was $z < -7$ or $z > +7$ Å, respectively. Accordingly, for each configuration, the distances, $d = \sqrt{\Delta x^2 + \Delta y^2 + \Delta z^2}$, between each site of the Stockmayer solute and each pore atom within $(\Delta x, \Delta y, \Delta z) = (15.0, 15.0, 8.0)$ Å were calculated (keeping in mind periodicity in z), and the minimum distance was determined. In addition to determining the minimum solute-silica distance at each time, the displacement relative to the pore interface was calcuated. That is, for each simulation, $\Delta d_{min,rel}(t) = d_{min}(t) - d_{min}(0)$ was calculated. The average over the 4000 NEMD trajectories is presented in the top panel of Figure 5.2. The result is a small, -0.5 Å net displacement over the course of the trajectory. Notably, the net displacement is just outside of statistical uncertainty. Because $\Delta d_{min,rel}(t) = d_{min}(t) - d_{min}(0)$, negative displacements indicate that $d_{min}(t) < d_{min}(0)$, and on average and at long times, the solute has moved closer to the pore wall.

The large uncertainty in the net displacement suggests that alternative ways of thinking about the displacement should be considered. One way is to group

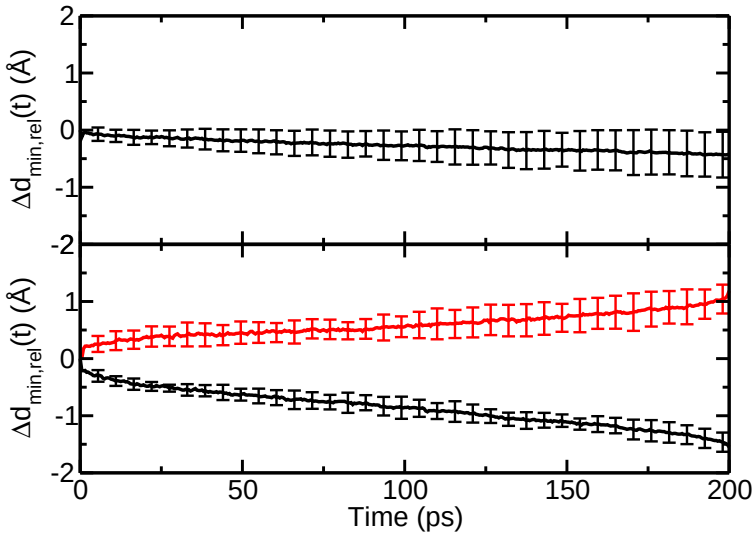

Figure 5.2: The Stockmayer solute in a hydrophilic pore shows a small (0.5 Å) net displacement toward the silica interface by 200 ps after excitation, as shown in the top panel. This can be decomposed (bottom panel) into displacements toward (black) or away from (red) the silica interface. Neither direction shows, on average, displacements much more than 1.5 Å.

$d_{min,rel}(t)$ curves by the direction of their overall displacement. For example, trajectories showing net solute displacements over 200 ps that are negative (*i.e.*, toward the pore wall) are averaged. Similarly, trajectories in which the net displacement of the solute is away from the wall are considered together. The result of such a calculation is shown in the bottom panel of Figure 5.2. The black curve represents the average of all trajectories with solutes that move toward the wall. If the solute moves toward the pore wall, on average it moves approximately 1.5 Å. Similarly, if the solute moves away from the wall, on average it moves approximately 1 Å. Thus net effect (shown in the top panel), can be thought of as the weighted sum of molecules moving to and away from the interface. The result is the previously discussed weak, but statistically significant, average displacement of approximately 0.5 Å toward the pore interface.

Because the equilibrium MD simulations discussed in Chapter 4 indicated that spectra are a function of solute position within the pore, and because of the weak (albeit statistically significant) post-excitation displacement observed here, it is reasonable to speculate that displacement is also a function of position at the time of excitation (initial position). To this end, the displacement relative to the pore interface as a function of time has been parsed by the minimum distance to the pore interface at $t = 0$ by 1 Å increments. Additionally, the minimum distance to the pore interface averaged over the initial 10% of the trajectory (20 ps) has also been used to parse the relative displacements. The results of the former method are presented in Figure 5.3. The latter was motivated by noting that the solute displacements (relative to the minimum distance to the pore wall) at early times are

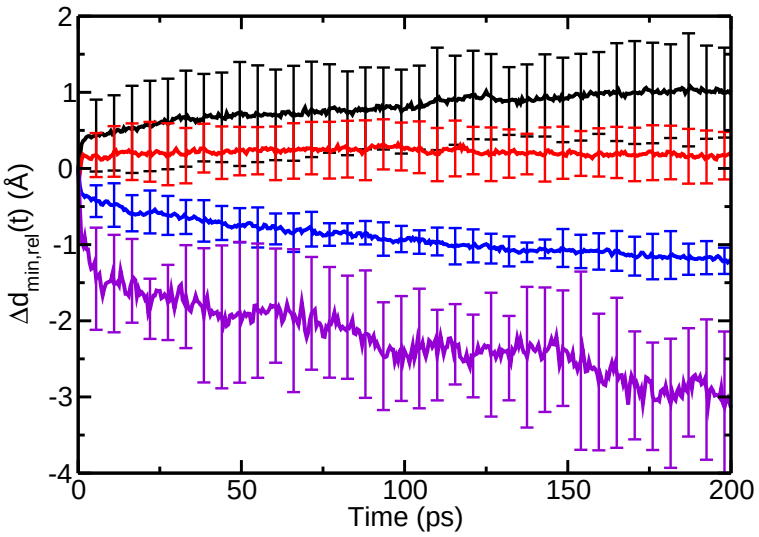

Figure 5.3: The solute displacement as a function of time is shown for initial minimum distances to the pore of 5 (black), 7 (red), 9 (blue), and 11 (purple) Å. Solutes near the interface travel slightly away from it, whereas solutes in the pore interior are strongly drawn toward the pore interface.

often unpredictable and sometimes change sign. It was suspected that averaging the position over the initial 10% and using that value for decomposition would result in "proper binning," with the result that the curves would become smoother. This, however, was not the case. In fact, this allows curves with different $t = 0$ positions to be averaged together, which results in erratic displacement profiles as a function of time.

In Figure 5.3, the minimum distance to the pore interface at $t = 0$ distinguishes the curves. The black, red, blue, and purple curves represent $d_{min}(0)$ =5, 7, 9, and 11 Å from the wall, respectively. A schematic interpretation of these results is provided in Figure 5.4. Because the solute molecule is large, $d_{min}(0) = 5$ Å is already near the pore interface. The results of Chapter 4 suggest that the energy to displace solvent near the pore interface is large. Additionally, increased direct contact with the interface is eventually disfavored by strong Lennard-Jones repulsions. It is speculated that for these reasons, the black curve shows a net displacement over 200 ps that is slightly positive or away from the pore interface. For initial solute positions further from the interface, the net displacement is larger and toward the wall. Notably, this is at odds with a simple physical model based strictly on the Coulombic potential, in which the larger charges associated with the excited state solute result in stronger attraction to the pore interface, where movement would be most dramatic. A simple explanation (implied previously) may be that solutes already at the interface at time $t = 0$ have only one direction to move—away from the interface. Currently, the role of the solvent in displacement of the solute after excitation is unclear. The results presented here, however,

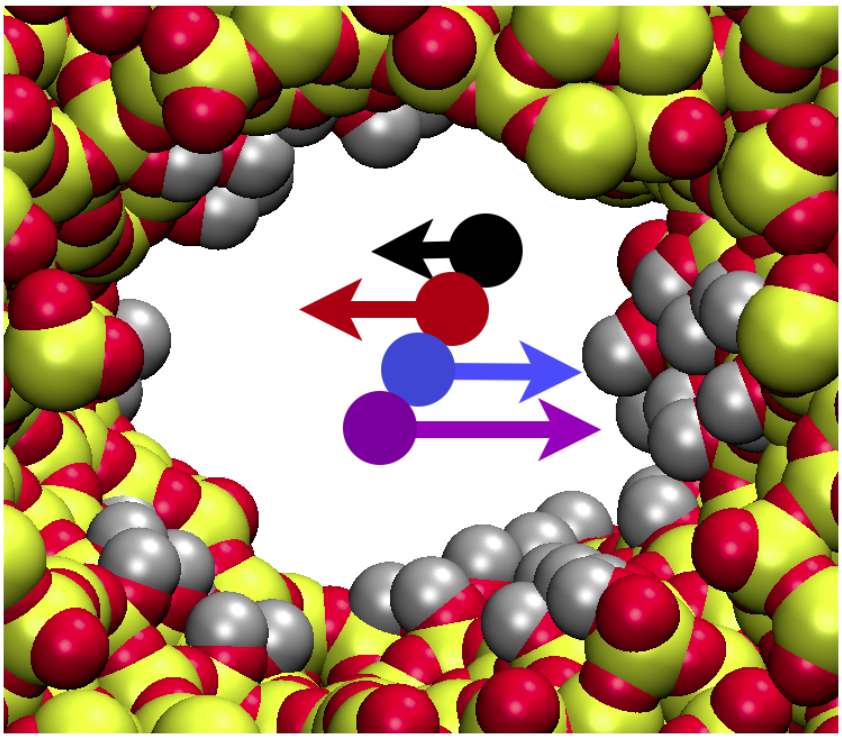

Figure 5.4: The curves of Figure 5.3 are schematically interpreted. For solute t_0 minimum distances to the pore interface (dots) of 5 (black), 7 (red), 9 (blue), and 11 (purple) Å, displacements relative to the pore interface (arrows) over 200 ps are shown.

indicate that for the Stockmayer solute in the hydrophilic pore, a change in charge distribution can lead to a net displacement–in this case toward the pore interface. Thus, the first requirement in the solute diffusion hypothesis is satisfied in these NEMD simulations.

5.3.2 Solute Spectra

The spectral dependence upon the solute position within the pore—requirement two in the solute diffusion hypothesis—is now examined. At each time in a NEMD trajectory, the Coulombic energy difference between the excited and ground state is calculated as $\Delta E_{fl} = E_{e.s.}^{Coul} - E_{g.s.}^{Coul}$. The energy difference, ΔE_{fl}, is then histogrammed according to the minimum distance to the pore interface, which was partitioned in 1 Å increments. Similarly to the displacements, spectra associated with selected initial minimum distances to the pore are shown in Figure 5.5. In Figure 5.5, the black curve represents spectra associated with solute molecules with a minimum distance to the pore interface of approximately 4 Å. Comparing the positions of peak maxima, the spectrum for solutes near 4 Å is noticeably redshifted by about 10 kJ mol^{-1}. Notably, the larger uncertainties associated with the black curve are a consequence of decreased sampling of the solutes 4 Å from the interface. The solutes toward the pore interior (red, blue, purple curves) are similar to one another and show no shifting. These spectra, like those from equilibrium simulations, show blue-shifted shoulders that have not been further investigated. The results here are consistent with those of Chapter 4 and indicate that the solutes near the interface of the hydrophilic pore show redshifted spectra.

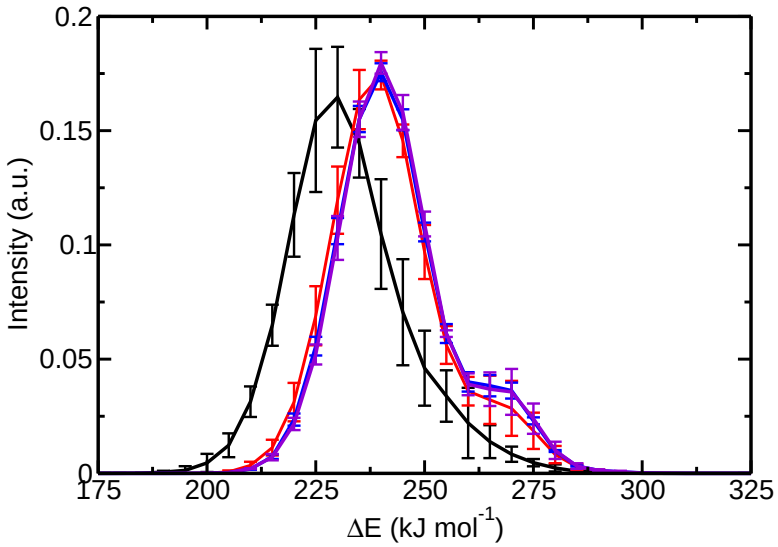

Figure 5.5: Fluorescence spectra are a function of the solute minimum distance to the silica interface. Representative spectra for minimum distances of 4 (black), 6 (red), 8 (blue), and 10 (purple) Å are shown.

Thus, requirement 2 for the solute diffusion hypothesis is satisfied in NEMD simulations of the Stockmayer solute.

5.3.3 Relationship to Atomistic Dye Molecules

To what extent the Stockmayer solute describes dynamics in "real" systems can be addressed by comparing results with those from simulations of an atomistic solute. To this end, a model for the coumarin 153 (c153) fluorescent dye [139], described in detail in Section 5.4, has been simulated and analyzed in the same manner as the Stockmayer solute. The complex nature of the dye (36 sites, planar/non-planar regions, decoration with functional groups) suggests that displacements relative to the pore interface should be calculated for several sites. If net translation toward the pore interface occurs after excitation at $t = 0$, the displacements at each site should have the same sign (*i.e.*, all selected sites show $\Delta d_{min,rel}(t) < 0$ or $\Delta d_{min,rel}(t) > 0$). To this end, the displacement analysis has been performed for the center of mass (COM, purple), nitrogen (N11, blue), trifluoromethyl carbon (C14, black), and carbonyl oxygen (O16, red), and the results are presented in Figure 5.6. The displacements for c153 are smaller than those for the Stockmayer solute and also have greater uncertainty associated with them. Importantly, the selected sites show displacements in different directions relative to the pore interface—some toward and some away from the interface. The nitrogen atom (Figure 5.6) shows a statistically significant but very small shift of ≈ 0.25 Å toward the pore interface. No other sites within the molecule show a significant displacement with respect to the pore interface. This is inconsistent with a strongly directed displacement

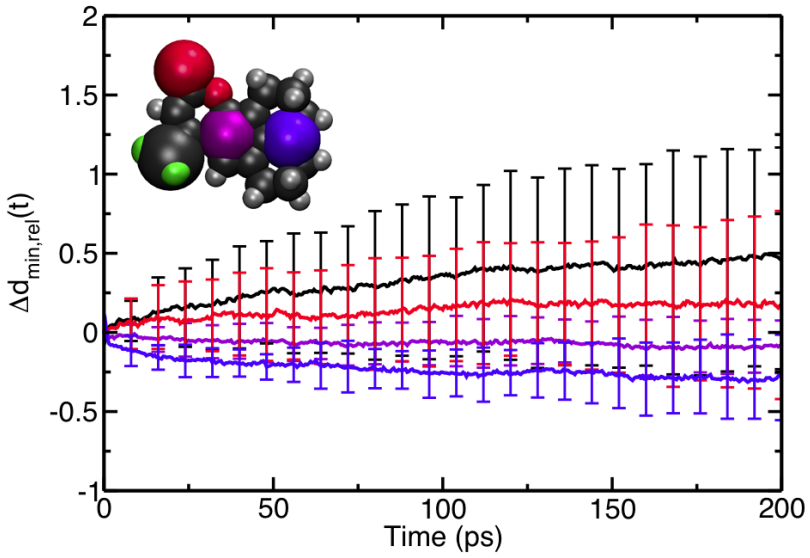

Figure 5.6: The relative minimum distance to the pore wall as a function of time for several sites on the c153 molecule. These sites are shown enlarged in the inset model and include the carbonyl oxygen (red), nitrogen (blue), the trifluoromethyl carbon (black), and center of mass (purple).

after excitation. The data presented here are also consistent with net rotation of the c153 molecule, although such an argument is speculative at best, given the magnitudes in the uncertainties. Decomposition based on initial minimum distance to the interface has not been performed for each of the four selected solute sites, as it would likely require better sampling and statistics than are currently accessible. Additionally, the extension of this analysis to longer times may be appropriate.

Spectroscopic properties can also be investigated for the c153 molecule and compared to the results for the Stockmayer model. Several sites in the c153 model are spectroscopically important (*e.g.*, the nitrogen atom) or chemically important (*e.g.*, the carbonyl oxygen). Thus, a spectroscopic analysis similar to that for the Stockmayer solute was conducted for multiple sites of interest on the c153 molecule. The results are presented in Figure 5.7. In each panel, the atom of interest is enlarged in the representation of the molecule. Thus the upper left, lower left, upper right, and lower right panels correspond to decompositions based on the COM site (purple), nitrogen atom (blue), trifluoromethyl carbon atom (black), and carbonyl oxygen atom (red), respectively. For each site, the fluorescence energy, ΔE, was histogrammed (using a 1 Å bin width) based on the site's minimum distance to the pore interface at time $t = 0$, $d_{min}(0)$. Thus, each panel shows a spectrum for selected $d_{min}(0)$ = 4 (black), 6 (red), 8 (blue), and 10 (purple) Å from the pore interface.

As for the relative displacements, the spectra presented in Figure 5.7 are difficult to interpret due to the large uncertainties associated with each curve. The large uncertainties come from two factors. Small shifts among block spectra used in

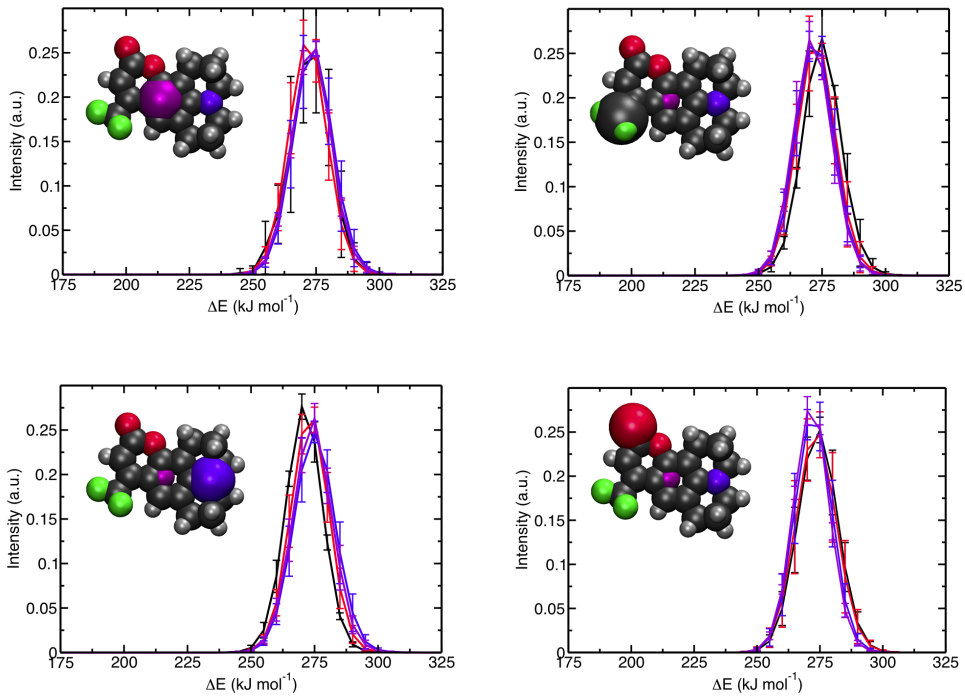

Figure 5.7: Fluorescence spectra have been calculated as a function of minimum distance to the pore interface at t_0 for different sites on the coumarin 153 molecule. For each panel, the c153 site of interest has been highlighted by enlargement. In all panels, spectra for $d_{min}(0)$ = 4 (black), 6 (red), 8 (blue), and 10 (purple) Å are shown.

calculating the uncertainty result in larger error bars, particularly where the curve is rapidly varying. Additionally, the solute does not sample all areas within the pore evenly. Accordingly, there are fewer data for solute atom locations near the pore interface, and the black curves representing $d_{min} = 4$ Å show correspondingly larger error bars. In a few cases, statistically meaningful redshifting can be observed, for example when N11 is around 4 Å from the pore interface. This is likely a consequence of the fact that N11 shows the largest change in charge upon excitation (see Table 5.4), and therefore undergoes a large change in Coulombic interactions when it is near the pore interface. Thus, while spectroscopic differences based on site position are difficult to discern for the c153 model, due in part to sampling issues, the preliminary results presented here are encouraging.

The position of the Stockmayer solute in the pore is a function of its charge distribution, and its spectral characteristics, in turn, depend on its position in the pore. However, due to insufficient sampling, it can only be said that results for the c153 solute are encouraging and require additional study.

5.4 Extended Dye and Confinement Descriptions

The behavior of the Stockmayer solute in confinement and how this behavior is broadcast through the TDF signal are not readily extrapolated to more sophisticated systems. Instead, a more systematic approach is appropriate. To deconvolute effects from molecular shape, size, and functionality, a series of dye models and confining frameworks have been developed. It is hoped that their systematic investigation

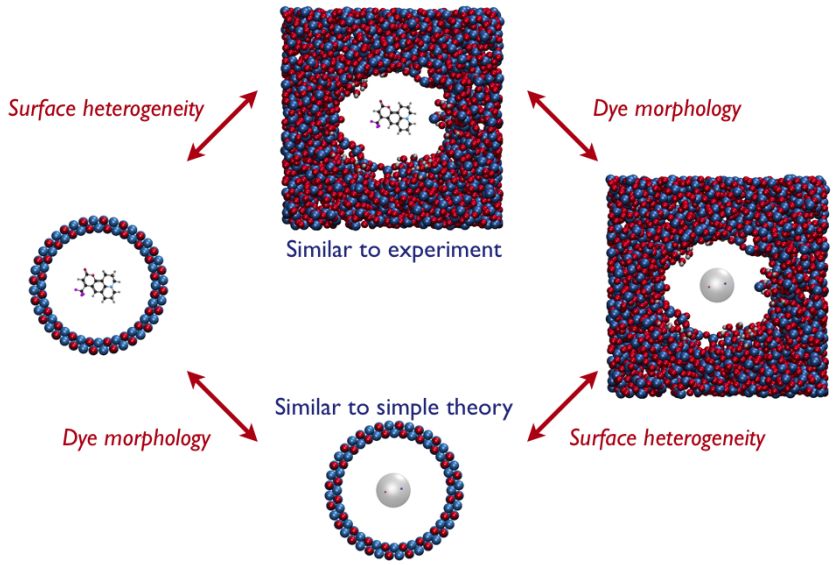

Figure 5.8: The Stockmayer solute and c153 dye models can be confined in atomically smooth cylinders or in rough, chemically heterogeneous silica pores.

can provide insight about these molecular-level effects, in the spirit of Figure 5.8. Figure 5.8 presents two models each for solute and confining framework. The Stockmayer solute and c153 can be confined in the same framework; differences in the results might be attributable to molecular shape or functional group chemistry. Similarly, the same dye can be confined in two different frameworks to investigate effects associated with surface roughness.

Notably, this simple example uses the two dye molecules already discussed, and comparison will still be complicated by the fact that the two dyes differ in several respects. A more systematic approach involves use of a longer series of dye models and confining frameworks. The development and description of these models are the subject of Section 5.4.

5.4.1 Atomistic Dye Models

Comparing NEMD results between the Stockmayer solute and coumarin 153, it is clear that, whereas results for the Stockmayer solute are demonstrative, results from the c153 model are only suggestive. To address why features that appear for the Stockmayer solute are weak or absent in the case of the atomistic dye, it may be useful to examine the behavior of a series of model solutes, similar in spirit to a shorter solute series used in bulk simulations[140]. Specifically, four models have been chosen to address effects of molecular shape and the presence of functional groups on fulfillment of the requirements of the solute diffusion hypothesis. These models are presented in Figure 5.9, and the advantages and limitations of each are discussed in turn.

To examine the effects of changing the charge distribution of the Stockmayer solute (*i.e.*, exciting the dye), the centers of positive and negative charge were held at a fixed length so that the dipole moment could be controlled through the magnitudes of the charges. This can be seen in Figure 5.9a. The charge sites (purple, gold) giving rise to the dipole are prevented from directly contacting either solvent or pore by housing them within a Lennard-Jones sphere located at the center of mass of the solute.

Real fluorescent dye molecules, however, are generally planar and have weakly charged sites distributed across the molecule. As a transition to realistic, atomistic dye models, the same dipole moments used in the Stockmayer solute (5, 10, 15 D) can be embedded in a simple benzene molecule shown in Figure 5.9b. The benzene model is based on the Optimized Potentials for Liquid Simulation (OPLS)

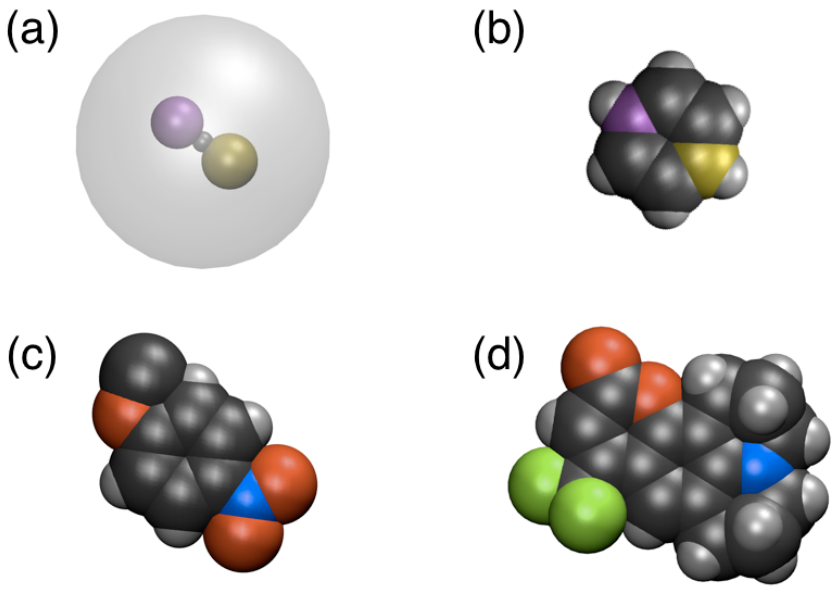

Figure 5.9: A series of dye models can be used to examine the effects of molecular shape and functional group chemistry. (a) The Stockmayer solute is a dipole within a spherical cavity. (b) A dipole has been embedded in a benzene ring. (c) Para-nitroanisole is a disubstituted benzene ring capable of hydrogen bonding. (d) Coumarin 153 has a complex shape and contains several chemically interesting sites. Color key: dipole site of negative charge (purple), dipole site of positive charge (gold), hydrogen (silver), carbon (black), oxygen (red), nitrogen (blue), fluorine (green).

force field. Centers of positive and negative charge (Figure 5.9b, gold and purple sites) have been substituted for carbon atoms 180° apart. Thus the dipole moment is directed along and controllable through the modified sites. A comparison of results for a modified benzene model and the Stockmayer solute can be used to determine how planarity versus sphericity influences solute position and spectral properties. Also, the Stockmayer solute can be reduced in size through a decrease in the Lennard-Jones σ value. Thus one can determine how the solute size and the number of nearest solvent molecules impacts the $S(t)$ response.

This approach can be explored further, in that the dipole moment of the modified benzene model can be matched to that of a small, atomistic dye model. Figure 5.9c shows para-nitroanisole (pNA), a dye with both a nitro group and methoxy group on opposite sides of a benzene ring, which has been studied experimentally [141]. Geometric parameters, which are provided in Tables 5.2 and 5.3, have been developed by combining parameters from several force fields [142–144].

The parameters in Table 5.2 associated with bond stretching and bending motions are described by

$$U_{bond} = K_r(r - r_{eq})^2 \tag{5.1}$$

and

$$U_{angle} = K_\theta(\theta - \theta_{eq})^2. \tag{5.2}$$

The remaining terms in the force field are Lennard-Jones, Coulombic, and torsional potentials, as described in Section 2.1. Development of the full model—and

Table 5.2: *p*-Nitroanisole geometric parameters

Bonds				
Sites			r_{eq} (Å)	$K_r^{\dagger}$
N	O(N)		1.225	550.00
N	C(N)		1.460	400.00
C(N)	C		1.400	489.00
C	C		1.400	489.00
C(O)	C		1.400	489.00
C(O)	O(C)		1.327	214.00
O(C)	CH_3		1.410	320.00
C	H		1.080	340.0
Angles				
Sites			θ_{eq} (deg)	$K_{\theta}^{\dagger}$
O(N)	N	O(N)	125.0	80.0
O(N)	N	C(N)	117.5	80.0
N(O)	C(N)	C	120.0	80.2
CX‡	C	C	120.0	80.2
C	C(O)	O	120.0	85.0
C(O)	O	CH_3	109.5	60.0
CX	C	H	120.0	35.0

† All force constants are reported in kcal mol^{-1}.
‡ CX indicates any carbon atom, regardless of its bonding partners.

particularly one for use in spectroscopic studies—will require electronic structure calculations to determine the ground- and excited-state charges.

The preliminary model proposed here may be useful in examining equilibrium behavior, and comparison of results between modified benzene and pNA can be used to provide insight into the role of specific functional groups in phenomena such as position distribution within the pore, interaction with the pore interface, and hydrogen bonding properties with both solvent and silanol groups. That is,

Table 5.3: *p*-Nitroanisole torsional parameters

Torsions						
Sites				$V_1^{\dagger}$	V_2	V_3
O(N)	N	C(N)	C	0.00000	6.835	0.00000
N	C(N)	C	C	0.00000	7.250	0.00000
N	C(N)	C	H	0.00000	7.250	0.00000
C(N)	C	C	C(O)	0.00000	7.250	0.00000
C(N)	C	C	H	0.00000	7.250	0.00000
C	C(N)	C	C	0.00000	7.250	0.00000
C	C(N)	C	H	0.00000	7.250	0.00000
C	C	C(O)	C	0.00000	7.250	0.00000
C	C(O)	C	C	0.00000	7.250	0.00000
C	C(O)	C	H	0.00000	7.250	0.00000
H	C	C	H	0.00000	7.250	0.00000
C	C	C(O)	O	0.00000	7.250	0.00000
C	C(O)	O	CH_3	0.00000	2.200	0.00000
H	C(O)	O	CH_3	0.00000	2.200	0.00000
Improper Torsions						
Sites				V_1	V_2	V_3
O(N)	O(N)	C(N)	C	0.00000	21.000	0.00000
C	C	C(N)	N	0.00000	2.200	0.00000
X	C	C	H	0.00000	2.200	0.00000
C	C	C(O)	O(C)	0.00000	2.200	0.00000

† All torsional parameters are reported in kcal mol^{-1}.
‡ X indicates any atom.

differences may be attributed largely to the specific chemistry imparted by the functional groups.

Lastly, it would be interesting to compare this small atomistic solute to a much larger atomistic solute, such as c153, shown as Figure 5.9d. Parameters for the model can be found in reference [139]. Modified force field parameters for the rigid c153 model are provided in Table 5.4. The published values for the difference

Table 5.4: Force field parameters for coumarin 153

Atom	M (g mol^{-1})	$q_{g.s.}$ (e)	$q_{e.s.}$ (e)	Δq (e)	σ (Å)	ε (kcal mol^{-1})
C2	12.01	-0.03410	0.07880	0.11290	3.550	0.29284
C4	12.01	-0.31180	-0.02480	0.28700	3.550	0.29284
C6	12.01	-0.26570	-0.19860	0.06710	3.550	0.29284
N11	14.01	-0.20580	0.01280	0.21860	3.300	0.71131
C14	12.01	0.57470	0.61150	0.03680	3.500	0.27612

in excited- and ground-state charnges, Δq, result in an excited state molecule with a small net charge of -0.0005e. To maintain charge neutrality of the excited state molecule, the Δq parameters for sites C2, C4, C6, N11, and C14 were each increased by $+0.0001$ e. These sites were chosen because they represent the 5 largest positive Δq values. The small increase in magnitude of Δq combined with the distributed positions of these sites within the c153 model suggest that this correction should not dramatically alter the results.

As shown previously in Sections 5.2 and 5.3.3, comparisons between simple and atomistic models are complicated by molecular size, shape, and chemistry. This does not, however, indicate which effects are due to the geometric restrictions imposed by the confining framework and associated effects (such as increased solvent layering), and which effects are due to surface roughness of silica pore and which are due to surface chemistry.

5.4.2 Alternative Confinement Descriptions

In a spirit similar to the development of a series of solutes, a series of confining frameworks can be used to investigate which effects are due to confining framework

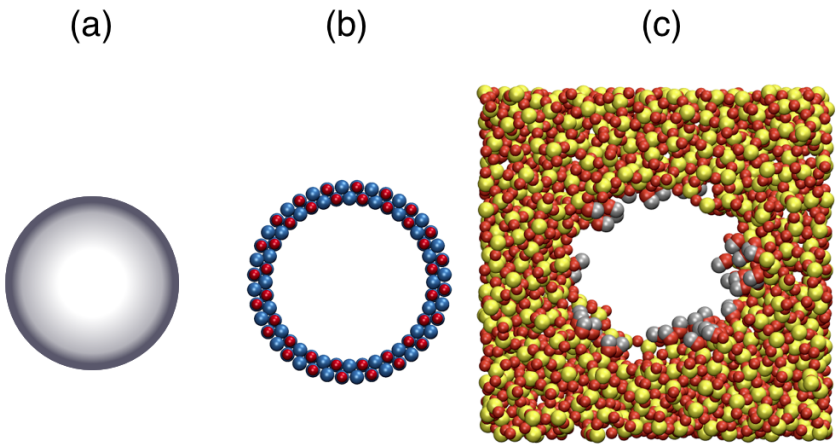

Figure 5.10: Several different confining systems can be used to investigate the effects of the confining framework. In the simplest form of confinement (a), a smooth potential is used to restrict molecular motion to a small cylinder. This can be expanded to an "atomically smooth" system (b), in which a cylinder of atoms is constructed. Lastly, the atomistic amorphous silica pore (c) can be used to investigate the effects of surface roughness and chemical functionality.

size, surface roughness, and surface chemistry. Such a set of models is shown in Figure 5.10.

The simplest way to confine the solvent/solute system is to use a potential with cylindrical symmetry (Figure 5.10a) to mimic confinement in the silica pore. No atomistic features then contribute to the TDF signals associated with confinement with such a potential. The confining potential approach has the added advantage that the effective radius of the cylinder can be easily changed. This can be exploited to study the effect of increasing solvent layering, which has been shown to influence position within the confining framework for small diatomic solutes.

Smooth cylindrical confinement cannot easily address effects associated with charge. A simple cylindrical arrangement of atoms of alternating charge (Figure 5.10b) can be used to address electrostatic effects. The sizes of the atomic cylinders can be made similar to those of the smooth cylindrical confinement to determine how charge changes solvent packing and solute position. Additionally, small defects at the surface can be added (two atoms at a time to maintain charge neutrality) as a way of adding in the effects of surface roughness without specific chemistry. Because these defects are expected to change the electric field, and thus potential, across the pore, they are of particular relevance to both the solute position distribution and solute fluorescence energy.

Lastly, the solvent and solute systems can be confined within amorphous silica pores (Figure 5.10c), as has been done in this study. The pores show a large degree of surface roughness and are chemically modified such that they present silanol groups to the pore interior. While surface irregularity can be investigated using modified atomically smooth cylinders, the placement of atoms in those systems is well-ordered. In the amorphous silica pore, the atomic arrangement is glass-like, and surface roughness may lead to slightly different effects than those in the modified atomically smooth cylinders. Additionally, the silica pore presents silanol and geminal silanol groups, and both solvent and solute are both strongly affected by surface chemistry, as shown in Section 4.3.2.

These effects of both surface roughness and surface chemistry can be quantified within the context of the extended jump model, which has been modified to account for increased reorientation timescales of water. In essence, the excluded volume

effect described in Section 2.4.2 for bulk alcohols should also apply to silica atoms at the pore interface. That is, the pore itself slows solvent reorientation by reducing the number of possible hydrogen bond exchange partners. Moreover, this effect will be site-specific, since different parts of the pore interface show different geometric arrangements of pore atoms and thus preclude hydrogen bond exchange to different degrees. Accordingly, the solvent jump time contribution should increase in the pore over that of the bulk solvent according to Equation 5.3,

$$\langle \tau_{conf}^{jump} \rangle = \frac{\sum_{i=1}^{N_{sites}} \rho_{V,i} \tau_{bulk}^{jump}}{N_{sites}} = \frac{\sum_{i=1}^{N_{sites}} \left(\frac{1}{1-f_i} \right) \tau_{bulk}^{jump}}{N_{sites}}, \tag{5.3}$$

where the sum runs over all interfacial sites, i, and V indicates that the effect is associated with excluded volume. Recall that f_i is the excluded volume fraction so $\rho_{V,i}$ is the slowdown factor. Similarly, the distribution of silanol groups within the pores will affect solvent reorientation dynamics through hydrogen bonding strength. This effect is absent in the alcohols, where all hydrogen bonding is roughly equivalent. In the silica pore, the dipole associated with silanol groups is different than that for the alcohols, and a solvent molecule can interact with one or several silanol groups. Moreover, the arrangement of silanol groups can vary. This reorientational slowing is anticipated to follow Equation 5.4

$$\langle \tau_{conf}^{jump} \rangle = \frac{\sum_{i=1}^{N_{sites}} \rho_{HB,i} \tau_{bulk}^{jump}}{N_{sites}} = \frac{\sum_{i=1}^{N_{sites}} e^{\beta \Delta \Delta G^{\ddagger}} \tau_{bulk}^{jump}}{N_{sites}}, \tag{5.4}$$

where $\Delta\Delta G^{\ddagger} = \Delta G^{\ddagger}_{SiOH} - \Delta G^{\ddagger}_{ROH}$. Each ΔG term is a free energy for elongating a hydrogen bond between an alcohol and the subscripted species.[23, 24] The slowdown factor ρ_{HB} therefore reflects the relative free energy cost for hydrogen bond exchange with the confining framework over that of the bulk liquid. These two effects—entropy and enthalpy through excluded volume and hydrogen bond strength, respectively—should combine uniquely at each site on the silica surface [145] so that

$$\langle \tau^{jump}_{conf} \rangle = \frac{\sum_{i=1}^{N_{sites}} \rho_{V,i} \rho_{HB,i} \tau^{jump}_{bulk}}{N_{sites}}. \tag{5.5}$$

The application of this model to alcohol reorientation in the silica pore will be particularly important when assigning timescales observed in the TDF spectrum to either solvent or solute contributions.

5.5 Time-Dependent Fluorescence Summary

The results presented in this Chapter indicate that in NEMD simulations, both the Stockmayer solute and c153 dye model show TDF spectra that decay on three timescales when confined in hydrophilic silica pores. The Stockmayer solute shows a small net displacement toward the pore interface after excitation, while displacements of different sites on the c153 model suggest rotational motion. Additionally, as the Stockmayer solute moves toward the silica interface, its fluorescence energy redshifts. An analysis of fluorescence energy as a function of position relative to the silica interface for selected sites on the c153 model suggest similar redshifting occurs for atomistic dye models. Thus, requirements 1) and 2) in the solute diffu-

sion hypothesis are satisfied in NEMD simulations of simple and atomistic dyes in confinement, a result which is consistent with the equilibrium MD results in Chapter 4. To what extent these appear in the TDF spectrum will require enhanced sampling.

Because chemistry happens at interfaces, which molecular-level effects lead to the satisfaction of each requirement in the solute diffusion hypothesis is of chemical interest beyond explaining emergent timescales in TDF spectra. A series of dye models comprising the Stockmayer solute, modified benzene, *p*-nitroanisole, and coumarin 153 can be used to determine how solute size, morphology, charge distribution, and functional group chemistry affect solute diffusion, reorientation and spectral properties, particularly at the interface. In a similar spirit, a series of confining framework is offered to systematically investigate effects from confinement size, charge distribution, surface heterogeneity and interfacial chemistry.

Chapter 6

Conclusions and Future Outlook

The present work is aimed at investigating trends in reorientation dynamics in bulk linear chain alcohols as well as investigating the information content in time-dependent fluorescence experiments in confined systems, which show emergent dynamics beyond those observed in the bulk. While the studies described here only begin to touch upon dynamics in liquid alcohols, many important conclusions have been drawn. Moreover, it is hoped that these results—what worked and what did not—can find utility in the future.

6.1 Conclusions from This Work

Studies of reorientation of linear alcohols have indicated that hydroxyl reorientation slows with increased alkyl chain length[25–29, 129]. The chemical similarity between water and alcohols (*i.e.*, they all contain hydroxyl groups) suggests that alcohol reorientation may be described similarly to water reorientation. Thus, to

investigate the origin of this reorientation trend, molecular dynamics (MD) simulations were performed for models of water, methanol, and ethanol. The lack of long-lived non-hydrogen bonded hydroxyl groups eliminates alcohol reorientation *via* the Debye mechanism [15]. Additionally, the Ivanov jump model[16] requires that intact hydrogen bonds are orientationally static between hydrogen bond switching events, which is not observed. Instead, the extended jump model proposed by Laage and Hynes[17, 18], and subsequently developed to describe water dynamics near hydrophobic solutes[20], describes well the trend that reorientation slows with increasing alkyl chain length.

The model consists of two contributions to reorientation—a fast, large amplitude reorientation during hydrogen bond switching ("jump" contribution) and the tumbling motion of intact hydrogen bonds ("frame" contribution). The jump time contribution follows the same trend in reorientation. Notably, the reorientation slowing is not an effect of hydrogen bond strength. Further, hydrogen bond exchange geometries are very similar across the series, as shown by bimodal distributions in the jump angle for each molecule. The trend in the jump time contribution then originates with the characteristic hydrogen bond jump time for each, an effect that is well-explained using excluded volume arguments. In essence, the increased alkyl bulk results in fewer incoming hydrogen bond exchange partners, which increases the time for a hydrogen bond switching to occur. The timescale for reorientation of intact hydrogen bonds ("frame" contribution) also increases, but it increases less than the increase in the jump time. Importantly, for alcohols, the relative jump and frame contributions therefore indicate that hydrogen bond

tumbling is the dominant reorientation pathway, whereas hydrogen bond switching is dominant in water reorientation.

For higher alcohols through *n*-hexanol, reorientation timescales continue to increase with increasing alkyl chain length, and the overall excluded volume fraction continues to increase. However, in higher alcohols, additional timescales are observed with the interesting trend of decreasing amplitude.

Several attempts have been made at explaining these, a number of which proved unsuccessful. As observed for supercooled water, the extended jump model can result in the longtime reorientation becoming split between two timescales–k_{short} and k_{long}—as a consequence of the distribution of jump rate constants, which in alcohols can be related to the distribution of excluded volume fractions. Correlation functions in the excluded volume fraction have been calculated in a preliminary fashion, but their calculation is expensive. Accordingly, alternative hypotheses were investigated. Trends in nonspecific, local coordination shells and exchange rates between them failed to describe the dynamics. Additionally, a more global picture that higher order structures show different dynamics also fails to describe reorientation in higher alcohols.

A reasonable explanation for these effects was found, however, through additional calculations. Local hydrogen bond relationships successfully explain the bimodal distribution of hydrogen bond jump angles. Specifically, hydrogen bond exchange occurs at low jump angle when the current and future acceptor are hydrogen bonded to one another, while the exchange generally occurs at higher jump angle when these molecules have no hydrogen bonding relationship.

Two-dimensional free energy plots (in distance and angle coordinates) show the growing-in of new free energy minima (and associated barriers) with increased alkyl chain length, which successfully explains the emergent timescales. The quantitative agreement between free energy barriers and reorientation timescales, however, may require additional considerations such as solvent viscosity.

Additional timescales also emerge in the time-dependent fluorescence (TDF) spectra of nanoconfined systems, but their origin remains similarly unclear. One hypothesis—the solute diffusion hypothesis—is that because the confining framework introduces an anisotropy in the system, solute properties, including fluorescence energy, change across the confining framework, and that emergent timescales actually report on motion of the reporter dye itself. For this to be observed, the solute position within the confining framework must depend on the solute charge distribution, the fluorescence energy must depend on the solute position, and the net effect—the motion across the confining framework with a change in spectrum—must occur on experimentally accessible timescales and with measurable amplitude.

The first two qualifications were addressed using equilibrium MD simulations of a model Stockmayer solute dissolved in ethanol and confined within a silica pore. The results indicate that for 5, 10, and 15 D dipole moments on the solute, the solute position within the hydrophilic pore is strongly biased, while it is more modestly biased in the hydrophobic pore. Additionally, spectral properties, including fluorescence energy, absorption energy, and spectral line width, all depend upon the solute position within the hydrophilic pore, but not the hydrophobic pore. Free energy decompositions indicate that interactions with the silica interface are

primarily responsible, while contributions from solvent organization play a smaller role. Investigation of several locations within the hydrophilic pore suggest that specific chemistry, *i.e.*, hydrogen bonding with silanol groups at the pore interface, is primarily responsible these effects.

To determine the extent to which solute motion manifests in the TDF signal, two different dye molecules—the simple Stockmayer solute and the more chemically relevant and well-studied coumarin 153 (c153) dye—were dissolved in ethanol and confined in a hydrophilic silica pore. The relevant post-excitation solute properties—solute displacement within the pore and solute fluorescence energy—were followed for 200 ps in non-equilibrium molecular dynamics (NEMD) trajectories. The results for the solute displacement indicate a net movement toward the pore interface for the Stockmayer solute, while a net rotation is suggested for the c153 solute. Additionally, the Stockmayer solute shows a redshift in fluorescence spectrum near the pore interface, while the results for the c153 solute suggest that a similar change can occur for certain sites on the molecule. The TDF spectrum for c153 decays much faster than that for the Stockmayer solute, an effect which may be attributable to solute morphology. Additional timescales are not resolvable, and confirmation that changes to the TDF signal can arise from solute motions within the nanoconfining framework will require further investigation, preferably with the use of enhanced sampling techniques.

From the difference in TDF spectra and static spectra as a function of their position on the atomistic dye molecule, it is clear that both morphological and chemical effects are important in determining the solute contribution to the TDF

spectrum. Obviously, the two solutes provided here do not constitute a solute series large enough to determine how shape and chemistry alter spectral properties. To this end, two additional solute models—modified benzene (mBz) and *para*-nitroanisole (pNA)—have been preliminarily constructed. The adjustability of the dipole moment of mBz means that comparisons of results between mBz and the Stockmayer solute can be made, with differences attributable to the shape and size of the molecule, *i.e.*, the distribution of surrounding solvent. Similarly the dipole moment of mBz can be tuned to that of pNA, so that differences in the results for each solute can be (at least in part) attributed to specific functional group chemistry. This growing-in of effects may lead to better interpretation of c153 spectral properties and assist in identification of which dye properties are important if a dye molecule is to contribute to the TDF spectrum. This is of particular importance, as no general principles have yet been identified to predict which confined systems show emergent timescales and which do not.

6.2 Imminent Work

The results of the present work have left several open questions and, as good science should, have raised possibilities for further study. The remainder of this work is then oriented toward future investigations, both imminent and distant, for which the present work serves a foundational role.

6.2.1 Reorientation of Bulk Alcohols

Hydroxyl group reorientation times in lower alcohols can be well-explained using excluded volume arguments within the context of the extended jump model. However, new timescales emerge in the reorientation of higher alcohols, as 4-exponential functions are required for reasonable fitting of $C_2(t)$ for the total, jump, and frame contributions to reorientation. Thus, assigning the additional timescale to either the jump contribution or frame contribution is not possible. To the end of identifying a mechanism for the emergent timescales, analysis of trends in free energy profiles should be completed. Additionally, while the longest timescale increases with increasing alkyl chain length, its amplitude decreases, an effect that is not readily explained. Lastly, several properties trend with viscosity. The calculation of viscosity for simulated alcohol systems, and its relationship to jump and frame times and amplitudes, should be pursued.

Another direction for continued research is the development of a predictive model for reorientation dynamics in alcohols. To this end, the effects of increasing steric bulk at a single site (in addition to effects from increasing steric bulk in series) should be investigated. Preliminary results for the ethanol/*iso*-propanol/*tert*-butanol series indicate that branching dramatically increases hydroxyl reorientation timescales. The mechanism for this is unclear, in part due to limited data. That is, the precise calculation of long timescales requires long trajectories, and precise values of excluded volume are required if they are to be related to these timescales, largely as a consequence of the reciprocal relationship between excluded volume fraction and timescale. Also, because molecular interactions are increasingly

important for longer alcohols (that is, more intermolecular interactions contribute to overall molecular behavior), all-atom force fields should be investigated and their results compared with those contained herein.

6.2.2 Reorientation of Confined Alcohols

It is anticipated from preliminary results that solute motion contributes to the TDF spectrum in nanoconfined systems. However, how different solute, solvent, and confining framework properties combine so as to enhance or suppress this effect in a measured spectrum remains unclear. The most relevant combinations are anticipated to involve solute and confining framework interactions, based on the results from the present work. Thus, while a series of solute and confining frameworks have been developed, their systematic testing has yet to be performed.

While the role in TDF spectra played by the solute is important, the role of the confining framework should also be investigated through simulations of neat linear-chain alcohols in nanoconfining silica pores. Results on studies of confined water,[145] as well as results presented in this work, suggest that pore heterogeneity plays a large role in solvent mobility, including reorientation. Pore heterogeneity, which includes surface topology and chemical functionality (*i.e.*, silanol groups), should induce site-specific reorientation slow-down factors that arise from both excluded volume, ρ_V, and hydrogen bond number and strength, ρ_{HB}. Thus, for a particular pore site, i, a characteristic slow-down factor, $\rho_i = \rho_{i,V}\,\rho_{i,HB}$,[23, 24] should give rise to a reorientation rate constant specific to the site, $\tau_i = \rho_{i,V}\,\rho_{i,HB}\,\tau_{bulk}$. The long-time reorientation timescale should then be an

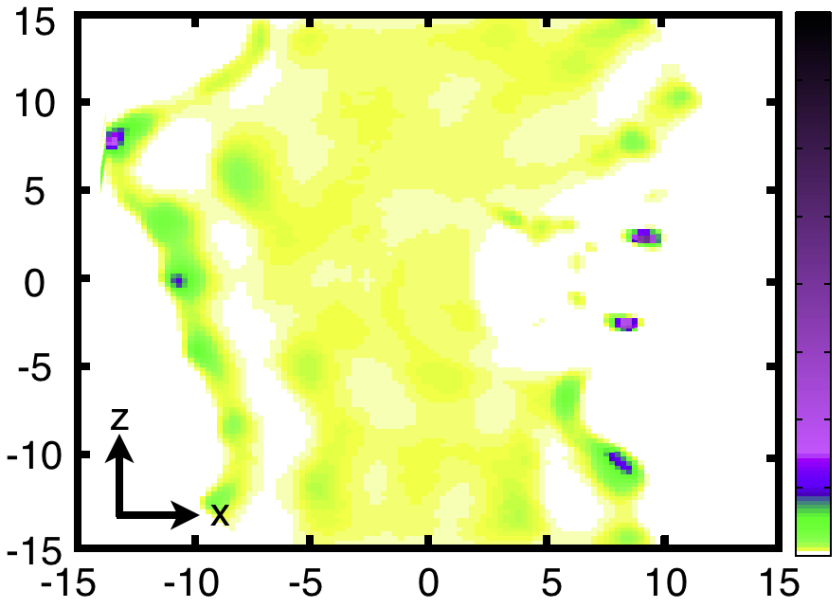

Figure 6.1: The probability of finding the ethanol COM site in the *xz* plane increases near the hydrophilic pore interface. Several sharp peaks are also present, indicating particularly strong associations between solvent and silica pore. The distribution was calculated from a 2 ns trajectory.

average over all site-specific timescales. Additional evidence for solvent slowing based on unique pore environments has already been obtained for ethanol through simple analysis of 2-dimensional position probability distributions within the pore, shown in Figure 6.1. In this Figure, regions near the pore interface ($\approx \pm 10$ Å) show increased probability that the solvent is found there. Peaks represented in purple suggest limited mobility, strong association, or both. To what extent such peaks are associated with site-specific dynamics, and how those dynamics originate, is a direct extension of the bulk work presented here, and will be critical in determining the information content in the TDF spectrum in confined ethanol systems.

6.2.3 Time-dependent Fluorescence in Confined Systems

A key extension of this work will be to relate timescales for solvent and solute motions to the timescales observed in TDF spectra in nanoconfined systems. To determine how solvent reorientation appears in the TDF spectrum requires the calculation of both site-specific and site-averaged timescales for confined ethanol predicted by the extended jump model (above). The reorientation dynamics are collective and related to interactions with the solute, and therefore, these dynamics are different from those discussed in Section 6.2.1. Additionally, timescales for solute diffusion (Sections 5.3.1 and 5.4.1) and reorientation within the pore should be compared to the directly calculated timescales derived from higher resolution TDF spectra. Lastly, the set of solute-nanoconfining framework combinations should be simulated to determine how different solute-framework interactions give rise to TDF-relevant phenomena, such as magnitude and direction of displacement, spectral shifting, overall TDF spectrum contribution, and any associated TDF amplitude.

6.3 Future Directions

6.3.1 Branched Alcohols

The previous discussion of reorientation in alcohols has focused on the effects of the extension of linear alkyl chains. For alcohols beyond ethanol, structural isomerism is possible. (For alcohols beyond propanol, stereoisomerism also becomes a

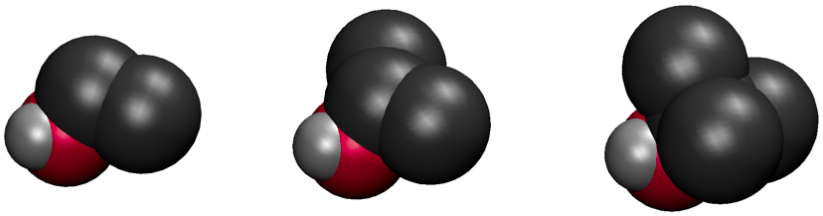

Figure 6.2: Ethanol, *i*-propanol, and *t*-butanol comprise a series over which steric bulk is increased at the β-carbon position.

consideration.) Thus, one can investigate not only the effect of linear chain length, but also the increase of steric bulk at a particular molecular site. Experimentally, the site of chain branch has been shown to have consequences for dynamics.[92, 114, 146, 147] Consider the series ethanol/*i*-propanol/*t*-butanol shown in Figure 6.2. Ethanol, *i*-propanol, and *t*-butanol can be viewed as methanol molecules with 1, 2, and all 3 of the the alkyl hydrogens replaced by methyl groups. How does the series constituted by ethanol/*i*-propanol/*t*-butanol compare to that of ethanol/*n*-propanol/*n*-butanol? Also, if a predictive model of excluded volume is to be developed, it is important to understand how increased substitution at a particular site influences access to the hydroxyl group.

In the interest of addressing such questions, OPLS-UA models for *i*-propanol and *t*-butanol were constructed. The force field parameters are the same as those reported in Table 2.1 Notably, the OPLS-UA description of *i*-propanol cannot be properly implemented in MD studies. (For a discussion of the problem, as well as a description of the corrective measures taken, see Appendix B.) Instead, the

torsional parameters presented in Table 6.1 are used in Equation 6.1.

$$V(\phi) = V_0 + \frac{1}{2}V_1(1+\cos(\phi-\delta)) + \frac{1}{2}V_2(1-\cos 2(\phi-\delta)) + \frac{1}{2}V_3(1+\cos 3(\phi-\delta)) \tag{6.1}$$

The α carbon and two/three methyl groups were treated as a rigid body for *iso*-

Table 6.1: OPLS-UA torsional parameters for branched alcohols.

Molecule	$V_0^{\dagger}$	V_1	V_2	V_3	δ (°)
i-PrOH	1.79494	3.28026	0.52300	-2.89114	-59.77
t-BuOH	0.00000	0.00000	0.00000	0.90650	0.00

† All values are reported in kJ mol^{-1}.

propanol/*tert*-butanol, respectively. Notably, the *i*-PrOH torsional potential in Table 6.1 was applied to a single site, while the *t*-BuOH torsional potential was applied to each methyl group. The resulting dihedral angle distributions were checked for both cases and agreed well with the results of Jorgensen[121].

The results for the calculation of $C_2(t)$ for the branched alcohols are presented in Figure 6.3. The branched alcohols *i*-propanol and *t*-butanol show similar $C_2(t)$ decays to about 100 ps. For both branched alcohols (solid lines), the reorientation time is much longer than their linear chain counterparts (dashed lines). Interestingly, it also appears that the short time behavior for *t*-butanol is faster than that of *i*-propanol, while the long time behavior for *t*-butanol is slower than that for *i*-propanol. However, the results presented in Figure 6.3 are only suggestive. Longer simulation times will be required to fully describe the reorientation dynamics in branched alcohols.

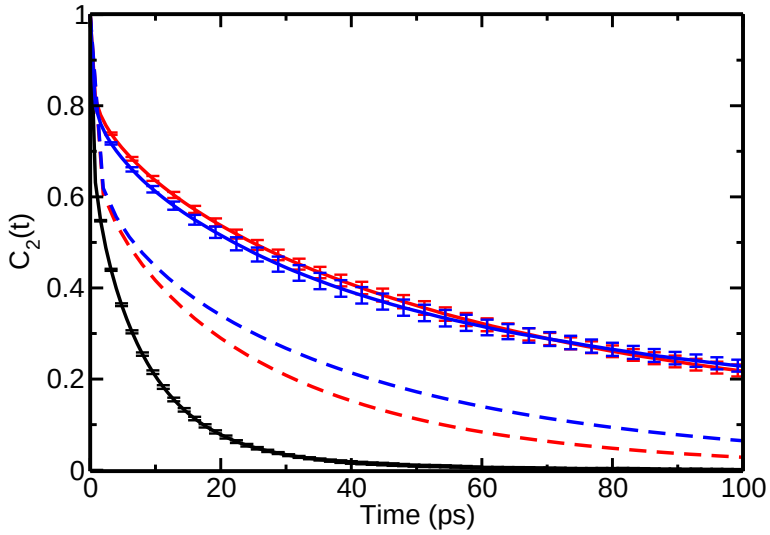

Figure 6.3: Hydroxyl reorientational correlation functions $C_2(t)$ for the ethanol (black)/*i*-propanol (red)/*t*-butanol (blue) series, in which steric bulk is increased at C_β (solid lines). For comparison, the corresponding linear series (dashed lines) comprising ethanol/*n*-propanol/*n*-butanol is included.

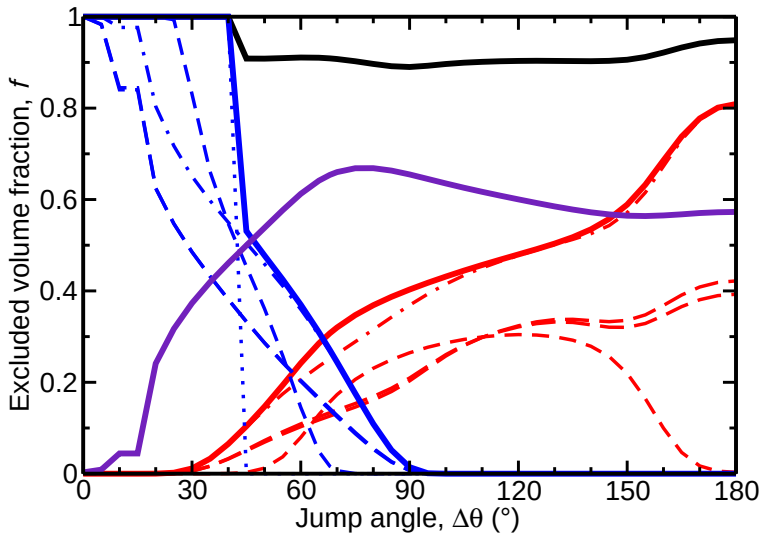

Figure 6.4: The excluded volume as a function of jump angle, $f(\Delta\theta)$, is shown for *i*-propanol. Solid lines represent total (black), hydrogen bond donor (blue), hydrogen bond acceptor (red), and all other (purple) contributions to f. Donor excluded volume is further decomposed into contributions from oxygen (dotted line), C_α (dashed line), individual C_β methyl groups (dot-short dashed lines), and total C_β methyl groups (dot-long dashed line). Acceptor excluded volume is further decomposed into C_α (dashed line), individual C_β methyl groups (dot-short dashed lines), and total C_β methyl groups (dot-long dashed line).

Initial examination of excluded volume profiles for the branched alcohols results in similar complications as for long chain alcohols: large values of f have intrinsically larger uncertainties with their associated time constants. As shown in Figures 6.4 and 6.5, the average excluded volume is anticipated to be large (*e.g.*, $f > 0.93$). Figures 6.4 and 6.5 also suggest that the excluded volume at C_β is strongly non-additive.

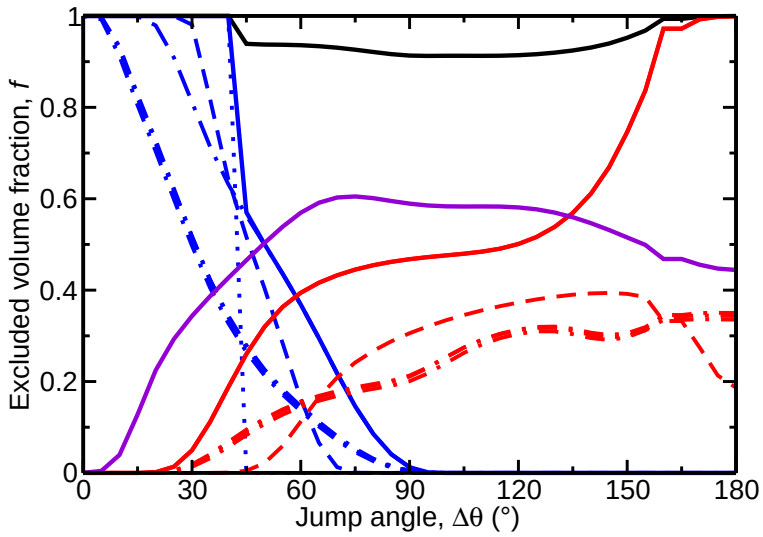

Figure 6.5: Same as Figure 6.4, except donor excluded volume is further decomposed into contributions from oxygen (dotted line), C_α (dashed line), individual C_β methyl groups (dot-short dashed lines), and total C_β methyl groups (dot-long dashed line). Acceptor excluded volume is further decomposed into C_α (dashed line), individual C_β methyl groups (dot-short dashed lines). The total contribution from C_β methyl groups (dot-long dashed line) is coincident with the full acceptor contribution (solid red line).

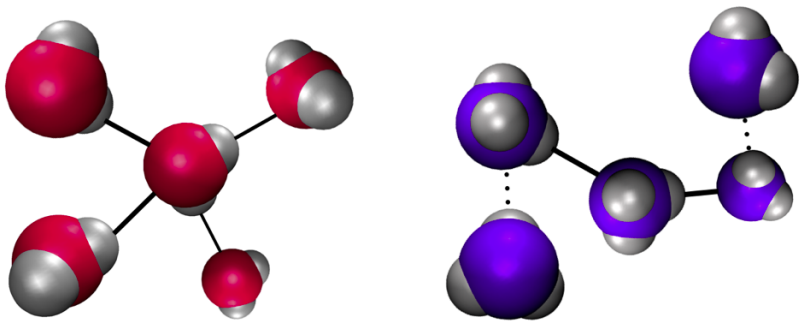

Figure 6.6: Left: Water molecules (oxygen, red; hydrogen, silver) are schematically shown engaged in a hydrogen bond network. The central molecule accepts two hydrogen bonds and donates two hydrogen bonds. Right: In ammonia (nitrogen, purple; hydrogen, silver), the central molecule accepts one hydrogen bond and donates one hydrogen bond. Two NH groups on the central molecule are not participating in hydrogen bonding.

Dynamic behavior in branched alcohols departs strongly from that observed in the series of linear chain alcohols. Explaining how the increased steric bulk at a single site, rather than along a chain, alters hydroxyl reorientation dynamics across a series of branched alcohols represents an additional path for future research.

6.3.2 Reorientation in Ammonia

In water, non-hydrogen bonded (or "dangling") hydroxyl groups persist for very short times (*i.e.*, < 1 ps). This is largely a consequence of the match in hydrogen bond donor and acceptor sites. In liquid ammonia, each molecule has 3 donor NH groups and only 1 acceptor (lone pair) site. The difference in hydrogen bond networking is depicted schematically in Figure 6.6. Because there is only one

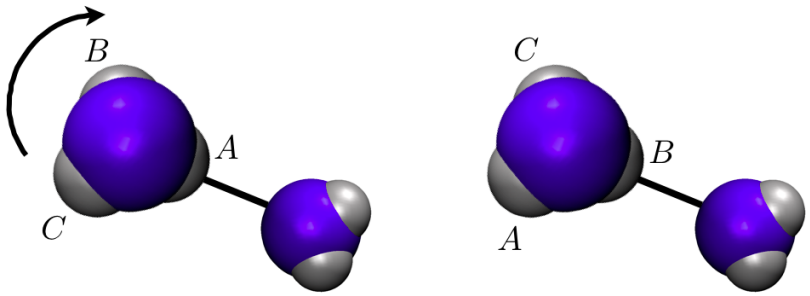

Figure 6.7: The three hydrogens (silver) bonded to a central nitrogen (purple) are labeled A, B, and C. The ammonia molecule is donating a hydrogen bond to a nearby acceptor. With rotation of 120°, the initial hydrogen bond involving H_A is broken and replaced by an equivalent hydrogen bond involving H_B.

acceptor site, each ammonia molecule can donate one hydrogen bond and accept one hydrogen bond. Therefore, each hydrogen bonded molecule may have 2 proximal dangling NH groups. This naturally raises the question: Between a donor and acceptor molecule, does hydrogen bond exchange occur between NH groups on the same donor, as in Figure 6.7? Due to comparisons[91, 112, 128] of NH dynamics in ammonia with OH dynamics in water, ammonia raises fundamentally interesting questions in the context of the extended jump model. The equivalence of the three NH groups suggests that hydrogen bond frustration may play a role in NH reorientation dynamics. Hydrogen bond jumps in ammonia might then be viewed as the change of hydrogen bond acceptor molecules for a given donor molecule. (The frame reorientation would retain its usual meaning.) Add to this the well-known effect that the barrier to inversion in ammonia is small. The overall reorientation might be viewed as a sum of three or four rate constants, *e.g.*, $k_2^{total} = k_2^{frustr} + k_2^{inv} + k_2^{jump} + k_2^{frame}$. What is the relative importance of each

reorientation pathway? Can the extended jump model be modified to account for additional reorientational mechanisms beyond those observed in water?

6.3.3 Reaction Rates in Solution

Lastly, as noted in Chapter 1, solvent reorientation is important in driving chemical transformation, such as charge transfer reactions. Do the excluded volume effects responsible for hydroxyl reorientation in alcohols also change the ability of alcohols to affect chemical reactions? While this is a difficult problem, a particularly simple system—2-(aminomethyl)phenol (Figure 6.8)—might be used to address this question. The amino group and hydroxyl group are positioned so that the hydroxyl hydrogen is directed toward the amino nitrogen. The model would be rigid, with the exception of the proton of interest. For methanol and *n*-hexanol, in what direction and to what extent is the equilibrium shifted (*i.e.*, to what extent is the proton associated with the nitrogen *vs.* the oxygen atom)? In each solvent, at what rate does proton transfer occur? If the equilibrium or dynamics are different between the two solvents, to what extent can excluded volume effects be used to explain the effect? Additionally, are solvent dynamics near versus far from the solute the same, or are solvent dynamics driven near the solute? Linking reorientation, particularly of alcohols in the context of the extended jump model, to chemical equilibria and reaction dynamics represents a large goal—one that is at the center of chemistry. It is hoped that the work contained herein serves as a small step toward achieving that goal.

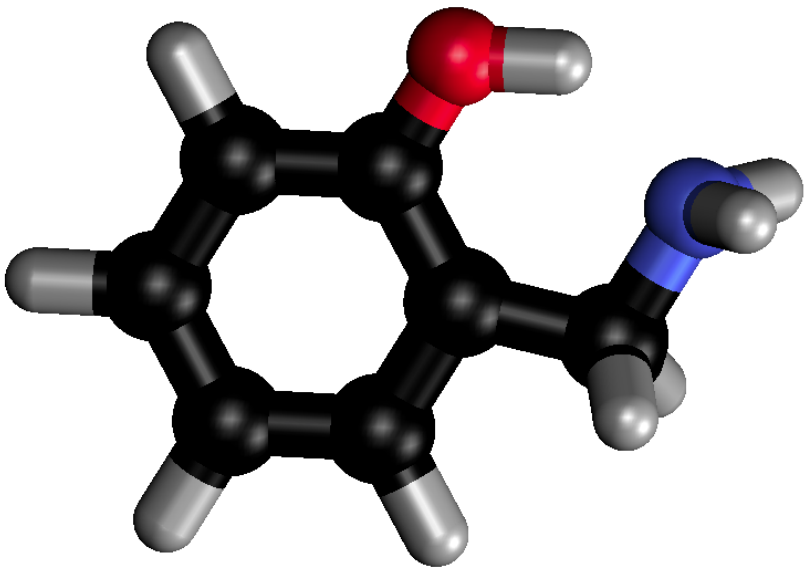

Figure 6.8: 2-(aminomethyl)phenol might be a molecule useful for studying proton transfer reactions in different alcohols to examine the effect of alcohol reorientation on chemical equilibrium and reaction dynamics. The hydrogen (silver) of interest is bonded to the oxygen atom (red) and positioned to interact with the nitrogen atom (purple).

Appendix A

Calculation of Excluded Volume

To adapt the excluded volume picture to the reorientation of alcohols and calculate f directly from the simulation trajectory, one assumes that the hydrophobic alkyl groups act as hydrophobic "solutes." In this case, the alkyl groups of the donor, acceptor, and any other molecule can block incoming hydrogen bond exchange partners. Additionally, the oxygen atom of the current acceptor can also block incoming exchange partners. The oxygen atoms of other molecules are not included in the list of exclusionary molecules, as they are considered incoming acceptors that comprise the transition state. For similar reasons, the donor oxygen atom is not considered when the excluded volume.

In practice, a ring of transition states is constructed using $R^{\ddagger} = 3.5$ Å, a user-specified transition state angle, $\Delta\theta^{\ddagger}$, and the number of ring points for the calculation, typically set to $n_{ring} = 200$. The calculation of the transition state ring (reference ring) occurs once, at the beginning of the calculation. The reference ring is calculated such that the $\underline{r}_{O_A - O_D}$ vector lies along the $+x$ axis, as in Figure A.1.

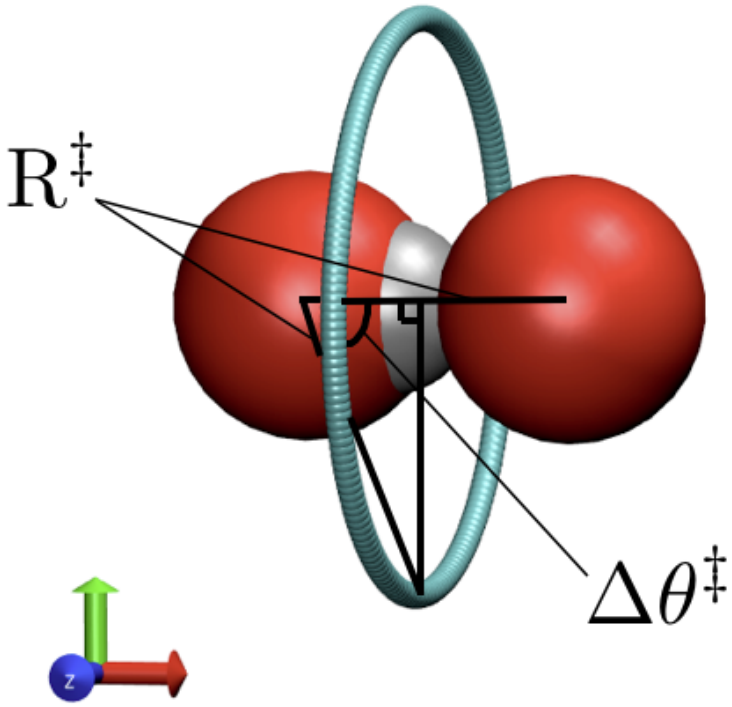

Figure A.1: A hydrogen bond with its $\underline{r}_{O_D-O_A}$ axis coincident with the $+x$ axis is used for calculation of the reference ring. The transition state distance, $R^{\ddagger}_{O_D-O_A} = 3.5$ Å and transition state angle, $\Delta\theta^{\ddagger}_{O_B-O_D-O_A} = 68^{\circ}$, are indicated. From these parameters, one can calculate the positions of the ring sites.

The coordinates for each ring site i are calculated as

$$\begin{aligned} x_i &= R^{\ddagger}\cos\Delta\theta^{\ddagger} \\ y_i &= (R^{\ddagger}\sin\Delta\theta^{\ddagger})\sin\left(2\pi\times\frac{i_{ring}}{n_{ring}}\right) \\ z_i &= (R^{\ddagger}\sin\Delta\theta^{\ddagger})\cos\left(2\pi\times\frac{i_{ring}}{n_{ring}}\right) \end{aligned} \tag{A.1}$$

and i runs from 1 to n_{ring}.

For identified hydrogen bonds, this ring is then copied and rotated into place along the identified hydrogen bond. The rotation of the vector requires two angles, θ and ϕ. Due to the limitations of the intrinisic inverse trigonometric functions (that is, $\sin^{-1}$ is defined on the interval $[-\frac{\pi}{2}, +\frac{\pi}{2}]$ and $\cos^{-1}$ is defined on the interval $[0, \pi]$), they cannot be used to determine orientations within the octants of the Cartesian coordinate system used in this study. Instead, the angles θ and ϕ were defined the following way:

Donor and acceptor oxygen displacements are given by

$$\begin{aligned} \mathrm{d}x &= \underline{x}_{O_A} - \underline{x}_{O_D} \\ \mathrm{d}y &= \underline{y}_{O_A} - \underline{y}_{O_D} \\ \mathrm{d}z &= \underline{z}_{O_A} - \underline{z}_{O_D} \end{aligned} \tag{A.2}$$

Then to determine ϕ,

$$\begin{aligned} &\text{if } \mathrm{d}x = 0, \text{ then} \\ &\qquad \text{if } \mathrm{d}y > 0, && \phi = \tfrac{\pi}{2} \\ &\qquad \text{if } \mathrm{d}y < 0, && \phi = \tfrac{3\pi}{2} \\ &\qquad \text{else} && \phi = 0 \\ &\text{else} \\ &\qquad \phi = \cos^{-1}\left(\frac{\mathrm{d}x^2}{\sqrt{\mathrm{d}x^2(\mathrm{d}x^2+\mathrm{d}y^2)}}\right) \\ &\qquad \text{if } \mathrm{d}x < 0, && \phi = \pi - \phi \\ &\qquad \text{if } \mathrm{d}y < 0, && \phi = -\phi \\ &\text{end if} \end{aligned} \tag{A.3}$$

Similarly, to determine θ,

$$
\begin{array}{lll}
\text{if } \mathrm{d}z = 0, \text{ then} & & \\
 & \theta = 0 & \\
\text{else} & \theta = \cos^{-1}\left(\frac{\mathrm{d}z^2}{\sqrt{\mathrm{d}z^2(\mathrm{d}x^2+\mathrm{d}y^2+\mathrm{d}z^2)}}\right) & \\
 & \text{if } \mathrm{d}z > 0, & \theta = \theta - \frac{\pi}{2} \\
 & \text{if } \mathrm{d}z < 0, & \theta = \frac{\pi}{2} - \theta \\
\text{end} \quad \text{if} & &
\end{array}
\tag{A.4}
$$

The angles defined in this way can be used with rotations about the y and z axes that are applied to the copied reference ring along the x axis. Each point on the reference ring, described by $(x_{ref}, y_{ref}, z_{ref})$, is subjected to a rotation about the y axis, $\hat{\mathrm{R}}_y(\theta)$, followed by a rotation about the z axis, $\hat{\mathrm{R}}_z(\phi)$, to generate the ring encircling the $\underline{r}_{O_D-O_A}$ vector of interest in the bulk solution, as in equation

$$\underline{r}_{sol'n} = \hat{\mathrm{R}}_z(\phi)\,\hat{\mathrm{R}}_y(\theta)\,\underline{r}_{ref}$$

or more explicitly,

$$
\begin{pmatrix} x_{sol'n} \\ y_{sol'n} \\ z_{sol'n} \end{pmatrix} = \begin{pmatrix} \cos\phi & -\sin\phi & 0 \\ \sin\phi & \cos\phi & 0 \\ 0 & 0 & 1 \end{pmatrix} \begin{pmatrix} \cos\theta & 0 & \sin\theta \\ 0 & 1 & 0 \\ -\sin\theta & 0 & \cos\theta \end{pmatrix} \begin{pmatrix} x_{ref} \\ y_{ref} \\ z_{ref} \end{pmatrix} \tag{A.5}
$$

Extensive tests, including visualizations, were performed for each Cartesian octant, plane, and axis to validate the definitions of angles and rotations explained above.

When a hydrogen bond donor is identified in the simulation trajectory, a reference ring of transition states is rotated to align with the $\underline{r}_{O_D-O_A}$ vector as described above. The distance between each point on the ring and each atom in the simulation is then calculated. If the distance is less than the Van der Waals radius of the current atom, the site on the ring is marked as "excluded." Notably, the Van der Waals radius is taken as the first non-zero value in the pair distribution function, $g(R_{OX})$, where X indicates the site of interest (*e.g.*, O, $CH_{2,\alpha}$, etc.). The ratio of excluded points to all points comprising the ring of possible transition states is the excluded volume fraction, f. To obtain a reliable estimate of f, this is performed over many configurations for all molecules.

Appendix B

Modification of OPLS-UA Isopropanol

The optimized potentials for liquid simulations united atom (OPLS-UA) force field for alcohols parametrizes alkyl carbon groups so that the hydrogen and carbon atom effects (*e.g.*, size, interaction strength, etc.) are parametrized together. Thus, fully-substituted carbons, methine, methylene, and methyl groups are considered single sites in the simulation, each with a distinct set of parameters. This presents a problem for the case of *i*-propanol.

In Jorgensen's 1986 paper, it is stated that "2-propanol also has a trans form with the hydroxyl hydrogen between the two methyl groups and two mirror-image gauche forms (Figure 2)." Accordingly, at 180°, one should observe a local minimum between two large energy barriers representing hydroxyl hydrogen-methyl interactions, which is what is depicted in Figure 2 of that work. The statement and corresponding Figure are in agreement with one another.

However, there are two problems here. Firstly, the parameters for the torsional parameters for 2-propanol provided in Table III of that work fail to produce the

curve presented in Figure 2 of that work. Secondly, in the united-atom description, there is no explicit methine hydrogen to serve as a "handle" for the potential. That is, even if one had the set of parameters that reproduces the potential in Figure 2, there is no atom to which one can apply it.

Figure B.1 shows the *i*-propanol torsional potential (top) using the provided parameters, which are reproduced in Table B.1. A reconstruction of the Jorgensen Figure is provided as Figure B.2 (top). In each case, the corresponding Newman projection has been provided (bottom).

Table B.1: Torsional parameters for OPLS-UA *iso*-propanol

parameter	Table values[†]
V_0	0.429
V_1	0.784
V_2	0.125
V_3	-0.691

[†] Values are reported in kcal mol^{-1}.

Comparing the potential and Newman projection of Figure B.1, it is clear that the *cis*, rather than *trans*, conformation is represented by the torsional parameter set. Comparison of Figures B.1 and B.2 suggests that a simple phase shift of 180° can remedy the problem. However, as noted by the asterisk in the Newman projection of Figure B.2, the atom to which the phase-shifted potential should be applied does not exist in the OPLS-UA model.

Two approaches can be taken in applying a phase-shifted potential. In the first approach, the model is modified by introducing a new site between the two methyl sites. The site is assigned a hydrogen mass (subtracted from the UA α-carbon site)

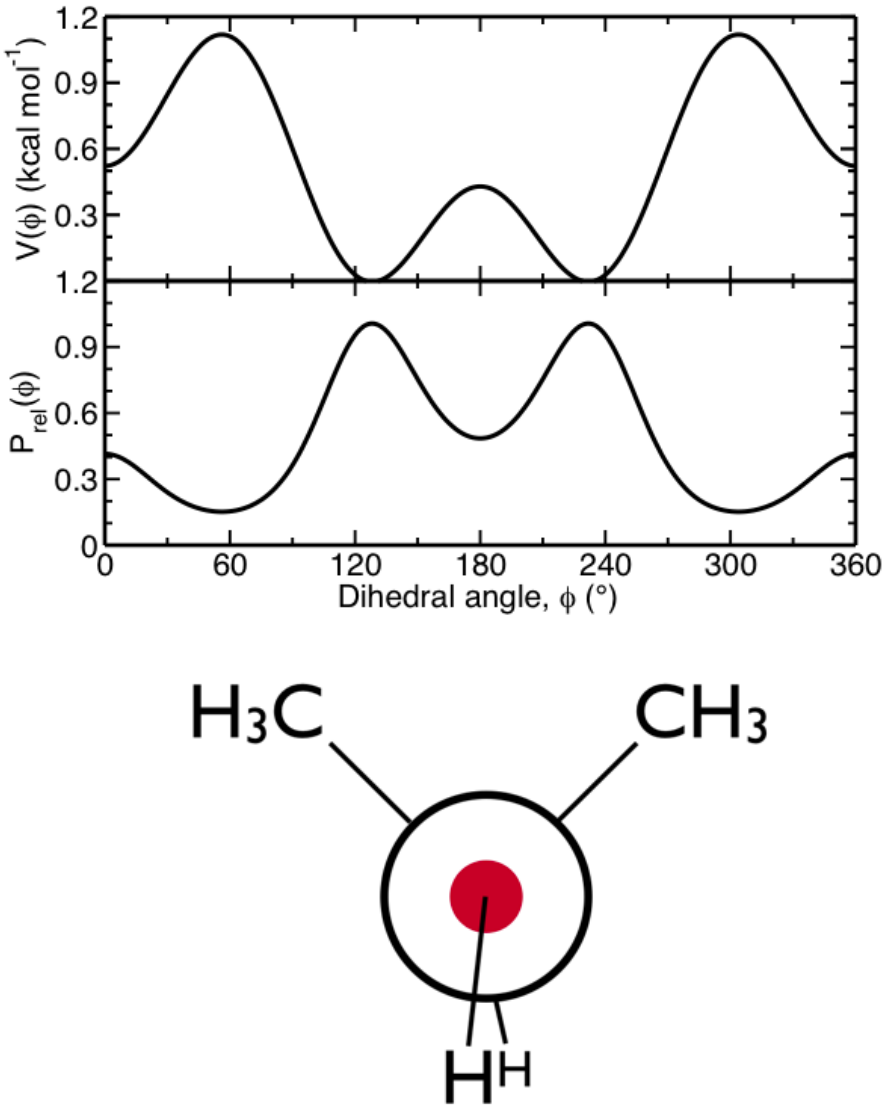

Figure B.1: The published OPLS-UA torsional parameters for *i*-PrOH result in a torsional potential curve (top, top panel) shifted by 180° relative to the published Figure (Figure B.2, top). The corresponding relative likelihood for dihedral angle $H-O-C_\alpha-H$ is also provided (top, bottom panel). The Newman projection (bottom) corresponding to the 180° "*trans*" conformation has been included, as viewed down the oxygen (red dot) - α-carbon (black circle) axis.

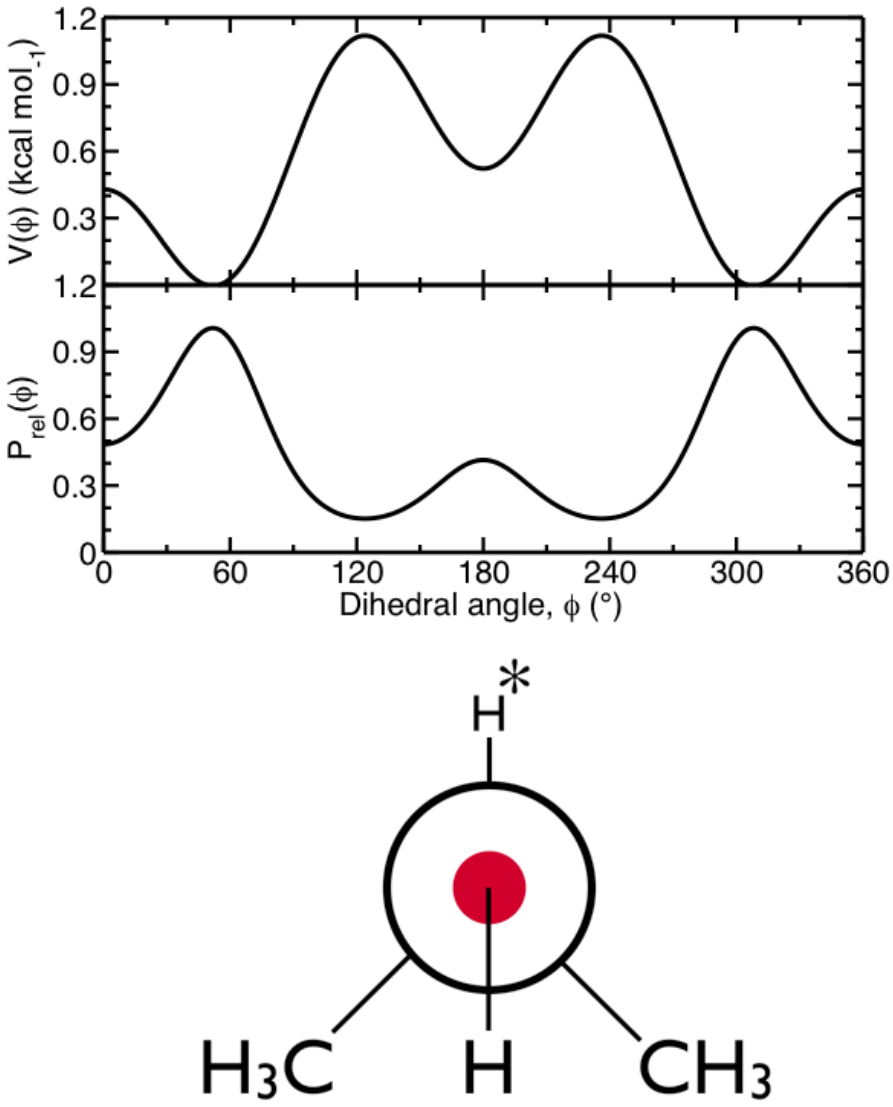

Figure B.2: The OPLS-UA torsional potential curve (top, top panel) has been reproduced from the published figure, which is shifted by 180° relative to the curve that results using the published torsional parameter set (Figure B.1, top). The corresponding relative likelihood for dihedral angle $H-O-C_\alpha-H$ is provided (top, bottom panel). The Newman projection (bottom) corresponding to the 180° "*trans*" conformation has been included, as viewed down the oxygen (red dot) - α-carbon (black circle) axis.

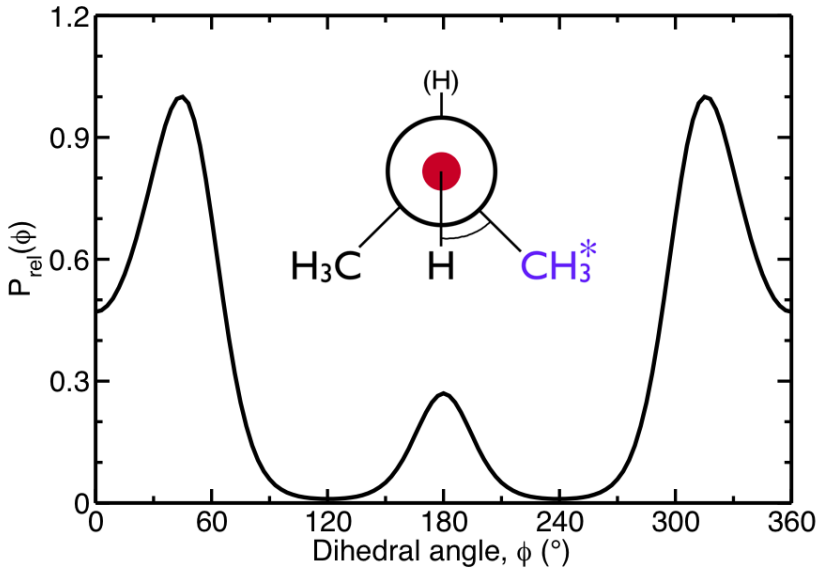

Figure B.3: The "handle" for the torsional potential (asterisk) is chosen as one of the united atom methyl sites (blue) and requires an approximately 60° phase angle. From the simulation data, the dihedral angles involving the implied α-hydrogen (in parentheses) can be calculated. The torsional potential applied this way results in an appropriate distribution of $H-O-C_\alpha-H_\alpha$ dihedral angles.

and is shortened to be an appropriate $(C-H)$ distance from the α-carbon. The 2 methyl groups, α-carbon, and new α-hydrogen can be considered a rigid body. The torsional parameters are modified by a phase-shift of 180° and applied to the α-hydrogen. Because this approach involves modification of the *i*-PrOH model, it has been avoided.

In the second—and preferred—approach, the torsional parameter is applied to an existing site with no modification of the model. As suggested by the Newman projection of Figure B.2 and depicted in the center of Figure B.3, a phase shift of approximately $\pm 60°$ can be applied to one or the other methyl site. For a selected

methyl site, the sign of the phase is determined by testing. Two simulations are run, in which the two methyl sites and methine site are treated as a rigid body, and the torsional potential is placed on the same methyl site in both simulations. The difference between the two simulations is the sign of the torsional phase angle.

Taking X to be a point midway between the C_{Me_1} and C_{Me_2} sites, the $H-O-C_\alpha-H_\alpha$ dihedral angle, ϕ, can be calculated as the angle between the HOC_α plane and the $OC_\alpha X$ plane phase shifted by 180°. The result should be the same as the dihedral angle made with the implied hydrogen (indicated in parentheses.) From the distribution of dihedral angles, $P(\phi)$, the correct sign of the phase angle is obvious, as use of the incorrect sign results in non-qualitative (let alone semi-quantiative) agreement with the distribution on the Right of Figure B.2.

Bibliography

[1] Shirota, H.; Horie, K. "Solvation dynamics in nonaqueous reverse micelles", *J. Phys. Chem. B* **1999,** *103,* 1437–1443.

[2] Yamaguchi, T.; Yoshida, K.; Smirnov, P.; Takamuku, T.; Kittaka, S.; Takahara, S.; Kuroda, Y.; Bellissent-Funel, M.-C. "Structure and dynamic properties of liquids confined in MCM-41 mesopores", *Eur. Phys. J.-Spec. Top.* **2007,** *141,* 19–27.

[3] Gil, M.; Wang, S.; Organero, J. A.; Teruel, L.; Garcia, H.; Douhal, A. "Femtosecond dynamics within nanotubes and nanocavities of mesoporous and zeolite materials", *J. Phys. Chem. C* **2009,** *113,* 11614–11622.

[4] Venables, D. S.; Huang, K.; Schmuttenmaer, C. A. "Effect of reverse micelle size on the librational band of confined water and methanol", *J. Phys. Chem. B* **2001,** *105,* 9132–9138.

[5] Takamuku, T.; Maruyama, H.; Kittaka, S.; Takahara, S.; Yamaguchi, T. "Structure of methanol confined in MCM-41 investigated by large-angle X-ray scattering technique", *J. Phys. Chem. B* **2005,** *109,* 892–899.

[6] Setua, P.; Seth, D.; Sarkar, N. "To probe the structure of methanol and Aerosol OT (AOT) in AOT reverse micelles by FTIR measurements", *Phys. Chem. Chem. Phys.* **2009,** *11,* 8913.

[7] Tan, H.-S.; Piletic, I. R.; Fayer, M. D. "Orientational dynamics of water confined on a nanometer length scale in reverse micelles", *J. Chem. Phys.* **2005,** *122,* 174501.

[8] Shevade, A. V.; Jiang, S.; Gubbins, K. "Adsorption of water-methanol mixtures in carbon and aluminosilicate pores: a molecular simulation study", *Mol. Phys.* **1999,** *97,* 1139–1148.

[9] Mukherjee, T. K.; Panda, D.; Datta, A. "Excited-state proton transfer of 2-(2 '-pyridyl)benzimidazole in microemulsions: Selective enhancement and slow dynamics in aerosol OT reverse micelles with an aqueous core", *J. Phys. Chem. B* **2005,** *109,* 18895–18901.

[10] Elola, M. D.; Rodriguez, J.; Laria, D. "Structure and dynamics of liquid methanol confined within functionalized silica nanopores", *J. Chem. Phys.* **2010,** *133,* 154707.

[11] Takahara, S.; Kittaka, S.; Mori, T.; Kuroda, Y.; Takamuku, T.; Yamaguchi, T. "Neutron scattering and dielectric studies on dynamics of methanol and ethanol confined in MCM-41", *J. Phys. Chem. C* **2008,** *112,* 14385–14393.

[12] Csanyi, E.; Kristof, T.; Lendvay, G. "Potential model development using quantum chemical information for molecular simulation of adsorption equilibria of water-methanol (ethanol) mixtures in zeolite NaA-4", *J. Phys. Chem. C* **2009,** *113,* 12225–12235.

[13] Thompson, W. H. "Solvation dynamics and proton transfer in nanoconfined liquids", 2011.

[14] Laage, D.; Hynes, J. T. "Do more strongly hydrogen-bonded water molecules reorient more slowly?", *Chem. Phys. Lett.* **2006,** *433,* 80–85.

[15] Debye, P. *Polar Molecules;* The Chemical Catalog Company, Inc.: New York, 1929.

[16] Ivanov, E. "Theory of rotational brownian motion", *Sov. Phys. JETP-USSR* **1964,** *18,* 1041–1045.

[17] Laage, D.; Hynes, J. T. "A molecular jump mechanism of water reorientation", *Science* **2006,** *311,* 832–835.

[18] Laage, D.; Hynes, J. T. "On the molecular mechanism of water reorientation", *J. Phys. Chem. B* **2008,** *112,* 14230–14242.

[19] Laage, D.; Stirnemann, G.; Sterpone, F.; Rey, R.; Hynes, J. T. "Reorientation and allied dynamics in water and aqueous solutions", *Annu. Rev. Phys. Chem.* **2011,** *62,* 395–416.

[20] Laage, D.; Stirnemann, G.; Hynes, J. T. "Why water reorientation slows without iceberg formation around hydrophobic solutes", *J. Phys. Chem. B* **2009,** *113,* 2428–2435.

[21] Stirnemann, G.; Laage, D. "Communication: On the origin of the non-Arrhenius behavior in water reorientation dynamics", *J. Chem. Phys.* **2012,** *137,* 031101-031101–4.

[22] Laage, D.; Hynes, J. T. "Reorientional dynamics of water molecules in anionic hydration shells", *Proc. Natl. Acad. Sci. USA* **2007,** *104,* 11167–11172.

[23] Sterpone, F.; Stirnemann, G.; Hynes, J. T.; Laage, D. "Water hydrogen-bond dynamics around amino acids: The key role of hydrophilic hydrogen-bond acceptor groups", *J. Phys. Chem. B* **2010,** *114,* 2083–2089.

[24] Stirnemann, G.; Hynes, J. T.; Laage, D. "Water hydrogen bond dynamics in aqueous solutions of amphiphiles", *J. Phys. Chem. B* **2010,** *114,* 3052–3059.

[25] Lankhorst, D.; Schriever, J.; Leyte, J. C. "Determination of the rotational correlation time of water by proton NMR relaxation in $H_2^{17}O$ and some related results", *Ber. Bunsen Phys. Chem.* **1982,** *86,* 215–221.

[26] Ludwig, R.; Gill, D. S.; Zeidler, M. D. "Molecular reorientation in liquid methanol", *Z. Naturforsch. A* **1991,** *46,* 89–94.

[27] Ludwig, R.; Weinhold, F.; Farrar, T. C. "Experimental and theoretical determination of the temperature dependence of deuteron and oxygen quadrupole coupling constants of liquid water", *J. Chem. Phys.* **1995,** *103,* 6941–6950.

[28] Ludwig, R.; Zeidler, M. D. "NMR relaxation in ethanol and propanol in their binary mixtures with carbon tetrachloride", *Mol. Phys.* **1994,** *82,* 313–323.

[29] Ludwig, R.; Rusbuldt, C.; Bopp, P. A.; Zeidler, M. D. "The anisotropy of the molecular reorientational motions in liquid methanol", *Z. Naturforsch. A* **1995,** *50,* 211–216.

[30] Ho, P.; Alfano, R. "Optical Kerr Effect in liquids", *Phys. Rev. A* **1979,** *20,* 2170.

[31] Harrison, N.; Jennings, B. "Optical Kerr Effect measurement for a series of alcohols", *J. App. Phys.* **1993,** *73,* 8076–8080.

[32] Błaszczak, Z.; Farhoud, M. "Optical Kerr effect in a series of n-alcohols", *J. Chem. Soc., Faraday Trans.* **1994,** *90,* 2455–2457.

[33] Laenen, R.; Rauscher, C. "Time-resolved infrared spectroscopy of ethanol monomers in liquid solution: Molecular reorientation and energy relaxation times", *Chem. Phys. Lett.* **1997,** *274,* 63–70.

[34] Asbury, J. B.; Steinel, T.; Fayer, M. D. "Hydrogen bond networks: Structure and evolution after hydrogen bond breaking", *J. Phys. Chem. B* **2004,** *108,* 6544–6554.

[35] Gulmen, T. S.; Sibert, III, E. L. "Vibrational energy relaxation of the OH(D) stretch fundamental of methanol in carbon tetrachloride", *J. Chem. Phys.* **2005,** *123,* 204508.

[36] Piletic, I. R.; Gaffney, K. J.; Fayer, M. D. "Structural dynamics of hydrogen bonded methanol oligomers: Vibrational transient hole burning studies of spectral diffusion", *J. Chem. Phys.* **2003,** *119,* 423–434.

[37] Laenen, R.; Simeonidis, K. "Energy relaxation and reorientation of the OH mode of simple alcohol molecules in different solvents monitored by transient IR spectroscopy", *Chem. Phys. Lett.* **1999,** *299,* 589–596.

[38] Laenen, R.; Gale, G. M.; Lascoux, N. "IR spectroscopy of hydrogen-bonded methanol: Vibrational and structural relaxation on the femtosecond time scale", *J. Phys. Chem. A* **1999,** *103,* 10708–10712.

[39] Iwaki, L. K.; Dlott, D. D. "Three-dimensional spectroscopy of vibrational energy relaxation in liquid methanol", *J. Phys. Chem. A* **2000,** *104,* 9101–9112.

[40] Asbury, J. B.; Steinel, T.; Stromberg, C.; Gaffney, K. J.; Piletic, I. R.; Goun, A.; Fayer, M. D. "Ultrafast heterodyne detected infrared multidimensional vibrational stimulated echo studies of hydrogen bond dynamics", *Chem. Phys. Lett.* **2003,** *374,* 362–371.

[41] Gaffney, K. J.; Piletic, I. R.; Fayer, M. D. "Hydrogen bond breaking and reformation in alcohol oligomers following vibrational relaxation of a non-hydrogen-bond donating hydroxyl stretch", *J. Phys. Chem. A* **2002,** *106,* 9428–9435.

[42] Lin, Y.; Pieniazek, P.; Yang, M.; Skinner, J. "On the calculation of rotational anisotropy decay, as measured by ultrafast polarization-resolved vibrational pump-probe experiments", *J. Chem. Phys.* **2010,** *132,* 174505.

[43] Moilanen, D. E.; Fenn, E. E.; Lin, Y.-S.; Skinner, J. L.; Bagchi, B.; Fayer, M. D. "Water inertial reorientation: Hydrogen bond strength and the angular potential", *Proc. Natl. Acad. Sci.* **2008,** *105,* 5295–5300.

[44] Piatkowski, L.; Eisenthal, K.; Bakker, H. "Ultrafast intermolecular energy transfer in heavy water", *Phys. Chem. Chem. Phys.* **2009,** *11,* 9033–9038.

[45] Wong, M.; Thomas, J. K.; Grätzel, M. "Fluorescence probing of inverted micelles. The state of solubilized water clusters in alkane/diisooctyl sulfosuccinate (Aerosol OT) soltuion", *J. Am. Chem. Soc.* **1976,** *98,* 2391–2397.

[46] Wong, M.; Thomas, J. K.; Nowak, T. "Structure and state of H_2O in reversed micelles. 3.", *J. Am. Chem. Soc.* **1977,** *99,* 4730–4736.

[47] Zinsli, P. E. "Inhomogeneous interior of aerosol OT microemulsions probed by fluorescence and polarization decay", *J. Phys. Chem.* **1979,** *83,* 3223–3231.

[48] Kondo, H.; Miwa, I.; Sunamoto, J. "Biphasic structure model for reversed micelles. Depressed acid dissociation of excited-state pyranine in the restricted reaction field", *J. Phys. Chem.* **1982,** *86,* 4826–4831.

[49] Liu, G.; Li, Y.-Z.; Jonas, J. "Confined geometry effects on reorientational dynamics of molecular liquids in porous silica glass", *J. Chem. Phys.* **1991,** *95,* 6892–6901.

[50] Gallegos, D. P.; Smith, D. M.; Brinker, C. J. "An NMR technique for the analysis of pore structure: Application to mesopores and micropores", *J. Colloid Interf. Sci.* **1988,** *124,* 186–198.

[51] Zhang, J.; Bright, F. V. "Nanosecond reorganization of water within the interior of reversed micelles revealed by frequency-domain fluorescence spectroscopy", *J. Phys. Chem.* **1991,** *95,* 7900–7907.

[52] Shirota, H.; Segawa, H. "Solvation dynamics of formamide and N,N-dimethylformamide in aerosol OT reverse micelles", *Langmuir* **2004,** *20,* 329–335.

[53] Sarkar, N.; Datta, A.; Das, S.; Bhattacharyya, K. "Solvation dynamics of coumarin 480 in micelles", *J. Phys. Chem.* **1996,** *100,* 15483–15486.

[54] Pal, S. K.; Sukul, D.; Mandal, D.; Sen, S.; Bhattacharyya, K. "Solvation dynamics of coumarin 480 in sol-gel matrix", *J. Phys. Chem. B* **2000,** *104,* 2613–2616.

[55] Pant, D.; Riter, R. E.; Levinger, N. E. "Influence of restricted environment and ionic interactions on water solvation dynamics", *J. Chem. Phys.* **1998,** *109,* 9995–10003.

[56] Riter, R. E.; Undiks, E. P.; Kimmel, J. R.; Levinger, N. E. "Formamide in reverse micelles: Restricted environment effects on molecular motion", *J. Phys. Chem. B* **1998,** *102,* 7931–7938.

[57] Willard, D. M.; Levinger, N. E. "Influence of morphology on polar solvation dynamics in lecithin reverse micelles", *J. Phys. Chem. B* **2000,** *104,* 11075–11080.

[58] Willard, D. M.; Riter, R. E.; Levinger, N. E. "Dynamics of polar solvation in lecithin/water/cyclohexane reverse micelles", *J. Am. Chem. Soc.* **1998,** *120,* 4151–4160.

[59] Pant, D.; Levinger, N. E. "Polar solvation dynamics in nonionic reverse micelles and model polymer solutions", *Langmuir* **2000,** *16,* 10123–10130.

[60] Corbeil, E. M.; Riter, R. E.; Levinger, N. E. "Cosurfactant impact on probe molecule in reverse micelles", *J. Phys. Chem. B* **2004,** *108,* 10777–10784.

[61] Hazra, P.; Chakrabarty, D.; Sarkar, N. "Solvation dynamics of Coumarin 153 in aqueous and non-aqueous reverse micelles", *Chem. Phys. Lett.* **2003,** *371,* 553–562.

[62] Mitra, R. K.; Sinha, S. S.; Pal, S. K. "Temperature-dependent solvation dynamics of water in sodium bis(2-ethylhexyl)sulfosuccinate/Isooctane reverse micelles", *Langmuir* **2008,** *24,* 49–56.

[63] Chakraborty, A.; Seth, D.; Setua, P.; Sarkar, N. "Dynamics of solvent and rotational relaxation of glycerol in the nanocavity of reverse micelles", *J. Phys. Chem. B* **2006,** *110,* 5359–5366.

[64] Corbeil, E. M.; Levinger, N. E. "Dynamics of polar solvation in quaternary microemulsions", *Langmuir* **2003,** *19,* 7264–7270.

[65] Bhattacharyya, K.; Bagchi, B. "Slow dynamics of constrained water in complex geometries", *J. Phys. Chem. A* **2000,** *104,* 10603–10613.

[66] Nandi, N.; Bhattacharyya, K.; Bagchi, B. "Dielectric relaxation and solvation dynamics of water in complex chemical and biological systems", *Chem. Rev.* **2000,** *100,* 2013–2045.

[67] Sahu, K.; Mondal, S. K.; Ghosh, S.; Bhattacharyya, K. "Ultrafast dynamics in biological systems and in nano-confined environments", *B Chem Soc Jpn* **2007,** *80,* 1033–1043.

[68] Bhattacharyya, K.; Bagchi, B. "On the origin of the anomalous ultraslow solvation dynamics in heterogeneous environments", *J. Chem. Sci.* **2007,** *119,* 113–121.

[69] Bhattacharyya, K. "Solvation dynamics and proton transfer in supramolecular assemblies", *Acc. Chem. Res.* **2003,** *36,* 95–101.

[70] Nandi, N.; Bagchi, B. "Dielectric relaxation of biological water", *J. Phys. Chem. B* **1997,** *101,* 10954–10961.

[71] Chowdhary, J.; Ladanyi, B. M. "Molecular dynamics simulation of aerosol-OT reverse micelles", *J. Phys. Chem. B* **2009,** *113,* 15029–15039.

[72] Morales, C. M.; Thompson, W. H. "Simulations of infrared spectra of nanoconfined liquids: Acetonitrile confined in nanoscale, hydrophilic silica pores", *J. Phys. Chem. A* **2009,** *113,* 1922–1933.

[73] Thompson, W. H. "A Monte Carlo study of spectroscopy in nanoconfined solvents", *J. Chem. Phys.* **2002,** *117,* 6618.

[74] Senapati, S.; Chandra, A. "Molecular dynamics simulations of simple dipolar liquids in spherical cavity: Effects of confinement on structural, dielectric, and dynamical properties", *J. Chem. Phys.* **1999,** *111,* 1223–1230.

[75] Faeder, J.; Ladanyi, B. M. "Solvation dynamics in reverse micelles: The role of headgroup-solute interactions", *J. Phys. Chem. B* **2005,** *109,* 6732–6740.

[76] Faeder, J.; Ladanyi, B. M. "Molecular dynamics simulations of the interior of aqueous reverse micelles", *J. Phys. Chem. B* **2000,** *104,* 1033–1046.

[77] Faeder, J.; Ladanyi, B. M. "Solvation dynamics in aqueous reverse micelles: A computer simulation study", *J. Phys. Chem. B* **2001,** *105,* 11148–11158.

[78] Thompson, W. H. "Simulations of time-dependent fluorescence in nanoconfined solvents", *J. Chem. Phys.* **2004,** *120,* 8125.

[79] Gomez, J. A.; Thompson, W. H. "Monte Carlo simulations of absorption and fluorescence spectra in ellipsoidal nanocavities", *J. Phys. Chem. B* **2004,** *108,* 20144–20154.

[80] Mitchell-Koch, K.; Thompson, W. H. "How important is entropy in determining the position-dependent free energy of a solute in a nanoconfined solvent?", *J. Phys. Chem. C* **2007,** *111,* 11991–12001.

[81] Pieniazek, P. A.; Lin, Y.-S.; Chowdhary, J.; Ladanyi, B. M.; Skinner, J. L. "Vibrational spectroscopy and dynamics of water confined inside reverse micelles", *J. Phys. Chem. B* **2009,** *113,* 15017–15028.

[82] Tsukahara, T.; Harada, M.; Tomiyasu, H.; Ikeda, Y. "NMR studies on effects of temperature, pressure, and fluorination on structures and dynamics of alcohols in liquid and supercritical states", *J. Phys. Chem. A* **2008,** *112,* 9657–9664.

[83] Veldhuizen, R.; de Leeuw, S. W. "Molecular dynamics study of the thermodynamic and structural properties of methanol and polarizable nonpolarizable carbon tetrachloride mixtures", *J. Chem. Phys.* **1996,** *105,* 2828–2836.

[84] Paolantoni, M.; Ladanyi, B. M. "Polarizability anisotropy relaxation in liquid ethanol: A molecular dynamics study", *J. Chem. Phys.* **2002,** *117,* 3856–3873.

[85] Guevara-Carrion, G.; Nieto-Draghi, C.; Vrabec, J.; Hasse, H. "Prediction of transport properties by molecular simulation: methanol and ethanol and their mixture", *J. Phys. Chem. B* **2008,** *112,* 16664–16674.

[86] Jiang, R.; Sibert, III, E. L. "How do hydrogen bonds break in small alcohol oligomers?", *J. Phys. Chem. A* **2009,** *113,* 7275–7285.

[87] Walser, R.; Mark, A. E.; van Gunsteren, W. F.; Lauterbach, M.; Wipff, G. "The effect of force-field parameters on properties of liquids: Parametrization of a simple three-site model for methanol", *J. Chem. Phys.* **2000,** *112,* 10450–10459.

[88] Bermejo, F. J.; Howells, W.; Jiménez-Ruiz, M.; González, M.; Price, D.; Saboungi, M.; Cabrillo, C. "Origin of the complex dielectric relaxation spectra of molecular glass formers", *Phys. Rev. B* **2004,** *69,* 174201.

[89] Perez-Pellitero, J.; Bourasseau, E.; Demachy, I.; Ridard, J.; Ungerer, P.; Mackie, A. D. "Anisotropic united-atoms (AUA) potential for alcohols", *J. Phys. Chem. B* **2008,** *112,* 9853–9863.

[90] Haughney, M.; Ferrario, M.; McDonald, I. R. "Molecular-dynamics simulation of liquid methanol", *J. Phys. Chem.* **1987,** *91,* 4934–4940.

[91] Kosztolanyi, T.; Bako, I.; Palinkas, G. "Hydrogen bonding in liquid methanol, methylamine, and methanethiol studied by molecular-dynamics simulations", *J. Chem. Phys.* **2003,** *118,* 4546–4555.

[92] Hassion, F. X.; Cole, R. H. "Dielectric properties of liquid ethanol and 2-propanol", *J. Chem. Phys.* **1955,** *23,* 1756–1761.

[93] Sindzingre, P.; Klein, M. L. "A molecular dynamics study of methanol near the liquid-glass transition", *J. Chem. Phys.* **1992,** *96,* 4681–4692.

[94] Guàrdia, E.; Sesé, G.; Padró, J. A. "On the hydrogen bonding effects in liquid methanol: A molecular dynamics simulation study", *J. Mol. Liq.* **1994,** *62,* 1–16.

[95] Iwaki, L.; Dlott, D. "Ultrafast vibrational energy redistribution within C-H and O-H stretching modes of liquid methanol", *Chem. Phys. Lett.* **2000,** *321,* 419–425.

[96] Ferris, T. D.; Zeidler, M. D.; Farrar, T. C. "The concentration dependence of the proton chemical shift and the deuterium quadrupole coupling parameter for binary solutions of ethanol", *Mol. Phys.* **2000,** *98,* 737–744.

[97] Ishiyama, T.; Sokolov, V. V.; Morita, A. "Molecular dynamics simulation of liquid methanol. I. Molecular modeling including C-H vibration and fermi resonance", *J. Chem. Phys.* **2011,** *134,* 024509.

[98] Skarmoutsos, I.; Guàrdia, E. "Local structural effects and related dynamics in supercritical ethanol. 2. Hydrogen-bonding network and Its effect on single reorientational dynamics", *J. Phys. Chem. B* **2009,** *113,* 8898–8910.

[99] Fidler, J.; Rodger, P. "Solvation structure around aqueous alcohols", *J. Phys. Chem. B* **1999,** *103,* 7695–7703.

[100] Levinger, N. E.; Davis, P. H.; Fayer, M. D. "Vibrational relaxation of the free terminal hydroxyl stretch in methanol oligomers: Indirect pathway to hydrogen bond breaking", *J. Chem. Phys.* **2001,** *115,* 9352–9360.

[101] Ishiyama, T.; Sokolov, V. V.; Morita, A. "Molecular dynamics simulation of liquid methanol. II. Unified assignment of infrared, raman, and sum frequency generation vibrational spectra in methyl C-H stretching region", *J. Chem. Phys.* **2011,** *134,* 024510.

[102] Vechi, S.; Skaf, M. "Molecular-dynamics simulations of dimethylsulfoxide-methanol mixtures", *J. Chem. Phys.* **2005,** *123,* 154507.

[103] Wendt, M. A.; Zeidler, M. D.; Farrar, T. C. "The temperature dependence of the deuterium quadrupole coupling constant and the molecular rotational correlation time in liquid methanol", *Mol. Phys.* **1999,** *97,* 753–756.

[104] Zasetsky, A. Y.; Petelina, S. V.; Lyashchenko, A. K.; Lileev, A. S. "Computer simulation study of rotational diffusion in polar liquids of different types", *J. Chem. Phys.* **2010,** *133,* 134502.

[105] Guàrdia, E.; Martí, J.; Pádro, J. A.; Saiz, L.; Komolkin, A. V. "Dynamics in hydrogen bonded liquids: water and alcohols", *J. Mol. Liq.* **2002,** *96-7,* 3–17.

[106] Yamaguchi, T.; Matubayasi, N.; Nakahara, M. "NMR study on the reorientational relaxation in supercritical alcohols", *J. Phys. Chem. A* **2004,** *108,* 1319–1324.

[107] Pálinkás, G.; Hawlicka, E.; Heinzinger, K. "A molecular dynamics of liquid methanol with a flexible three-site model", *J. Phys. Chem.* **1987,** *91,* 4334–4341.

[108] Bai, S.; Yonker, C. R. "Pressure and temperature effects on the hydrogen-bond structures of liquid and supercritical fluid methanol", *J. Phys. Chem. A* **1998,** *102,* 8641–8647.

[109] Saiz, L.; Pádro, J. A.; Guàrdia, E. "Structure and dynamics of liquid ethanol", *J. Phys. Chem. B* **1997,** *101,* 78–86.

[110] Martí, J.; Padró, J. A.; Guàrdia, E. "Hydrogen bonding influence on the intermolecular vibrational spectra of liquid methanol", *J. Mol. Liq.* **1995,** *64,* 1–12.

[111] Asahi, N.; Nakamura, Y. "Nuclear magnetic resonance and molecular dynamics study of methanol up to the supercritical region", *J. Chem. Phys.* **1998,** *109,* 9879–9887.

[112] Ferrario, M.; Haughney, M.; McDonald, I. R.; Klein, M. L. "Molecular-dynamics simulation of aqueous mixtures: Methanol, acetone, and ammonia", *J. Chem. Phys.* **1990,** *93,* 5156–5166.

[113] Behrends, R.; Kaatze, U. "Hydrogen bonding and chain conformational isomerization of alcohols probed by ultrasonic absorption and shear impedance spectrometry", *J. Phys. Chem. A* **2001,** *105,* 5829–5835.

[114] Barlow, S.; Bondarenko, G.; Gorbaty, Y.; Yamaguchi, T.; Poliakoff, M. "An IR study of hydrogen bonding in liquid and supercritical alcohols", *J. Phys. Chem. A* **2002,** *106,* 10452–10460.

[115] Benmore, C. J.; Loh, Y. L. "The structure of liquid ethanol: A neutron diffraction and molecular dynamics study", *J. Chem. Phys.* **2000,** *112,* 5877–5883.

[116] Versmold, H. "Processes of molecular-reorientation in methanol and propanol", 1975.

[117] Wensink, E. J. W.; Hoffmann, A. C.; van Maaren, P. J.; van der Spoel, D. "Dynamic properties of water/alcohol mixtures studied by computer simulation", *J. Chem. Phys.* **2003,** *119,* 7308–7317.

[118] Ferris, T. D.; Farrar, T. C. "The temperature dependence of the hydroxyl deuterium quadrupole coupling parameter and the rotational correlation time of the OD internuclear vector in neat ethanol-d1", *Mol. Phys.* **2002,** *100,* 303–309.

[119] Weitkamp, T.; Neuefeind, J.; Fischer, H. E.; Zeidler, M. D. "Hydrogen bonding in liquid methanol at ambient conditions and at high pressure", *Mol. Phys.* **2000,** *98,* 125–134.

[120] Berendsen, H. J. C.; Grigera, J. R.; Straatsma, T. P. "The missing term in effective pair potentials", *J. Phys. Chem.* **1987,** *91,* 6269–6271.

[121] Jorgensen, W. L. "Optimized intermolecular potential functions for liquid alcohols", *J. Phys. Chem.* **1986,** *90,* 1276–1284.

[122] Jorgensen, W. L.; Madura, J. D.; Swenson, C. J. "Optimized intermolecular potential functions for liquid hydrocarbons", *J. Am. Chem. Soc.* **1984,** *106,* 6638–6646.

[123] The DL_POLY Molecular Simulation Package. http://www.ccp5.ac.uk/DL_POLY.

[124] Nosé, S. "A molecular dynamics method for simulations in the canonical ensemble", *Mol. Phys.* **1984,** *52,* 255–268.

[125] Hoover, W. G. "Canonical dynamics: Equilibrium phase-space distributions", *Phys. Rev. A* **1985,** *31,* 1695–1697.

[126] Shoemaker, D. P.; Garland, C. W.; Nibler, J. W. *Experiments in Physical Chemistry;* McGraw-Hill: New York, 1989.

[127] Kumar, R.; Schmidt, J.; Skinner, J. "Hydrogen bonding definitions and dynamics in liquid water", *J. Chem. Phys.* **2007,** *126,* 204107.

[128] Smith, D. W. G.; Powles, J. G. "Proton spin-lattice relaxation in liquid water and liquid ammonia", *Mol. Phys.* **1966,** *10,* 451–463.

[129] Ludwig, R.; Zeidler, M. D.; Farrar, T. C. "Molecular dynamics in lower alcohols", *Z. Phys. Chem.* **1995,** *189,* 19–27.

[130] Laage, D.; Stirnemann, G.; Hynes, J. T. "Why water reorientation slows without iceberg formation around hydrophobic solutes", *J. Phys. Chem. B* **2009,** *113,* 2428–2435.

[131] Weiner, S. J.; Kollman, P. A.; Case, D. A.; Singh, C. U.; Ghio, C.; Alagona, G.; Profeta, S. J.; Weiner, P. "A new force field for molecular mechanical simulation of nucleic acids and proteins", *J. Am. Chem. Soc.* **1984,** *106,* 765–784.

[132] Schaftenaar, G.; Noordik, J. "Molden: a pre-and post-processing program for molecular and electronic structures", *J. Comput. Aided Mol. Design* **2000,** *14*, 123–134.

[133] Lide, D. R.; et al., *Handboook of Chemistry and Physics, 87th Edition;* The Chemical Rubber Company: Cleveland, OH, 2006.

[134] The LAMMPS Molecular Simulation Package. http://lammps.sandia.gov/index.html.

[135] Steinfeld, J. I.; Francisco, J. S.; Hase, W. L. *Chemical Kinetics and Dynamics, 1st Edition;* Prentice Hall: Englewood Cliffs, NJ, 1989.

[136] Zwanzig, R. "Rate processes with dynamical disorder", *Acc. of Chem. Res.* **1990,** *23*, 148–152.

[137] M. P. Allen, D. J. T. *Computer Simulation of Liquids;* Oxford University Press, Inc.: New York, 1987.

[138] Faeder, J.; Ladanyi, B. "Solvation dynamics in aqueous reverse micelles: A computer simulation study", *J. Phys. Chem. B* **2001,** *105*, 11148–11158.

[139] Kometani, N.; Arzhantsev, S.; Maroncelli, M. "Polar solvation and solvation Dynamics in supercritical CHF3: Results from experiment and simulation", *J. Phys. Chem. A* **2006,** *110*, 3405–3413.

[140] Kumar, P. V.; Maroncelli, M. "Polar solvation dynamics of polyatomic solutes: Simulation studies in acetonitrile and methanol", *J. Chem. Phys.* **1995,** *103*, 3038–3060.

[141] Siler, A.; Walker, R. "Effects of solvent structure on interfacial polarity at strongly associating silica/alcohol interfaces", *J. Phys. Chem. C* .

[142] Reis, H.; Papadopoulos, M. G.; Grzybowski, A. "Computer simulation of the linear and nonlinear optical susceptibilities of p-nitroaniline in cyclohexane, 1,4-dioxane, and tetrahydrofuran in quadrupolar approximation. II. Local field effects and optical susceptibilitities", *J. Phys. Chem. B* **2006,** *110*, 18537–18552.

[143] Jorgensen, W.; Laird, E.; Nguyen, T.; Tiradorives, J. "Monte-Carlo simulations of pure liquid substituted benzenes with OPLS potential functions", *J. Comput. Chem.* **1993,** *14*, 206–215.

[144] Wang, J.; Cieplak, P.; Kollman, P. A. "How well does a restrained electrostatic potential (RESP) model perform in calculating conformational energies of organic and biological molecules?", *J. Comput. Chem.* **2000,** *21*, 1049–1074.

[145] Laage, D.; Thompson, W. "Reorientation dynamics of nanoconfined water: Power-law decay, hydrogen-bond jumps, and test of a two-state model", *J. Chem. Phys.* **2012,** *136*, 044513.

[146] Crupi, V.; Magazu, S.; Maisano, G.; Majolino, D.; Migliardo, P. "Depolarized quasi-elastic light scattering and H-bond cooperative effects in liquid alcohols", *J. Phys.-Condens. Mat.* **1993,** *5*, 6819–6832.

[147] Yonker, C.; Wallen, S.; Palmer, B.; Garrett, B. "Effects of pressure and temperature on the dynamics of liquid tert-butyl alcohol", *J. Phys. Chem. A* **1997,** *101*, 9564–9570.